

**Control of the secondary crossflow instability:
Direct numerical simulation of localized suction
in three-dimensional boundary layers**

A thesis accepted by the Faculty of
Aerospace Engineering and Geodesy of the University of Stuttgart
in partial fulfilment of the requirements for the degree of
Doctor of Engineering Sciences (Dr.-Ing.)

by

Tillmann A. Friederich

born in Stuttgart

main-referee: Prof. Dr.-Ing. U. Rist

co-referee: Prof. Dr.-Ing. H. Fasel

co-referee: Prof. Dr.-Ing. E. Krämer

Date of defence: July 2nd, 2013

Institute for Aerodynamics and Gas Dynamics

University of Stuttgart

2013

“The number of parameters is daunting.”

Philippe R. Spalart, 1993

*Boeing Senior Technical Fellow,
Boeing Commercial Airplanes, Seattle*

(considering the overwhelming parameter space
regarding the setup of direct numerical simulations
in three-dimensional boundary layers with suction)

Vorwort

Diese Arbeit entstand während meiner Tätigkeit als akademischer Mitarbeiter am Institut für Aerodynamik und Gasdynamik der Universität Stuttgart.

Ich möchte mich ganz herzlich bei Prof. Ulrich Rist für die Übernahme des Hauptberichts und das dadurch gezeigte Vertrauen in meine Arbeit bedanken.

Herrn Prof. Fasel gilt mein ganz besonderer Dank dafür, dass ich während meines ISAP-Aufenthalts 2005/06 an der University of Arizona die Strömungsmechanik aus einem anderen Blickwinkel kennen lernen durfte - und auch die praktische Seite in Form von etlichen Flugstunden im Super Ximango nie zu kurz kam. Ebenso gilt mein Dank für die Übernahme des Mitberichtes.

Bei Herrn Prof. Krämer möchte ich mich ebenfalls für die Übernahme des Mitberichtes sowie die gewissenhafte Korrektur meiner Arbeit bedanken.

Bei Herrn Dr. Markus Kloker möchte ich mich für die äußerst produktive Zusammenarbeit bedanken, die mit dem ISAP Programm 2005 begann. In unzähligen Diskussionen konnten auch in auswegslos scheinenden Situationen immer wieder neue Türen aufgestoßen werden. Das wissenschaftliche Arbeiten durfte ich hierbei in Perfektion erlernen.

Den Kollegen am IAG danke ich für fünf tolle und abwechslungsreiche Jahre! Erfrischend unterschiedliche Meinungen und Diskussionen zu allen lebenswichtigen Themen ließen die gemeinsamen Mittagessen und ÖZ-Runden nie langweilig werden. Bei der Fußballtruppe möchte ich mich für fünf Jahre Sport in allen Wetterlagen bedanken und wünsche viele weitere heiße Duelle mit dem ITLR!

Stuttgart, im Juli 2013

Tillmann Friederich

Contents

Abstract	v
Zusammenfassung	vii
Notation	ix
1 Introduction	1
1.1 Crossflow vortices and secondary instability	4
1.2 Discrete suction for laminar flow control	8
1.3 Goals, methods and overview	15
2 Numerical methods	17
2.1 Incompressible numerical method	17
2.1.1 Computation of the steady spanwise-invariant base flow .	19
2.1.2 Computation of the perturbation flow	20
2.1.2.1 Governing equations	21
2.1.2.2 Boundary conditions	22
2.1.2.3 Implementation	24
2.1.2.4 Semi-implicit time integration	25
2.2 Compressible numerical method	26
2.2.1 Computation of the steady spanwise-invariant base flow .	27
2.2.2 Computation of the perturbed flow	28
2.2.2.1 Boundary conditions	29
2.2.2.2 Module for simulated suction	30
2.3 Verification	31
3 Base flows	35
3.1 Incompressible 3-d boundary layer	36
3.2 Compressible 3-d boundary layer at $Ma=0.7$	36
3.3 Compressible Blasius boundary layer at $Ma=0.5$	37
3.4 Properties of the 3-d base flows	38

4	Comparison of modeled and simulated suction	43
4.1	Aspects of modeled and simulated suction setups	44
4.2	Suction in a Blasius boundary layer at $Ma=0.5$	45
4.3	Pinpoint suction in a 3-d boundary layer	48
5	Control of crossflow transition	63
5.1	Reference case and pinpoint suction setup	65
5.2	Disturbance development for suction cases	67
5.3	Skin friction development	72
5.4	Vortical structures	74
5.5	Secondary instability	78
5.5.1	Eigenfunctions in crosscuts	78
5.5.2	Kelvin-Helmholtz shear	81
5.6	Analysis of crossflow-vortex interactions	84
6	Conclusions	91
	Appendix	95
A	Numerical setup and computational performance	95
B	Grid studies for incompressible method	101
B.1	Two-dimensional base flow	103
B.2	Three-dimensional base flow	105
C	Compressible Navier-Stokes equations	107
D	Coordinate systems	109
E	Influence of the hole diameter	111
	References	121

Abstract

Transition control by localized “pinpoint” suction in a three-dimensional boundary-layer flow with crossflow is investigated by means of direct numerical simulation. The control of large-amplitude steady crossflow vortices with active secondary instability constitutes hereby an alternative promising possibility to maintain laminar flow on relevant regions of airliner wings (active laminar flow control) resulting in a significant reduction of drag and thus also of greenhouse gas emissions.

Up to date, laminar flow control applied to tackle crossflow instability aims at a reduction of the primary crossflow instability, i.e. hindering the development of large-amplitude, secondarily unstable crossflow vortices. The classically applied homogeneous suction focuses on reducing the crossflow in the quasi two-dimensional base flow which results in hindered growth of crossflow vortices, later-induced secondary instability and hence delayed laminar-turbulent transition. On the other hand, techniques like the “distributed roughness elements” method or “distributed flow deformation” excite locally stable or weakly unstable crossflow vortex modes, leading to “benign” crossflow vortices that are spaced narrower than the naturally amplified ones while suppressing all other modes, including the most unstable ones.

In the current work, the three-dimensional nonlinear disturbance state with large-amplitude steady crossflow vortices including already active secondary instability is controlled by means of pinpoint hole suction.

The influence of hole-suction modeling on the effects of pinpoint suction is checked in the first part of the work where results from a numerically extensive compressible simulation are discussed that comprises the channel flow below the suction orifice. Although the actual wall-normal velocity distribution in the suction hole deviates from the modeled prescribed distribution, it is shown that at equal mass flux the effects on the crossflow vortex are virtually identical and secondary instability is equally attenuated.

In the second part of the work, localized pinpoint suction through holes is activated below the updraft side of the primary vortices. It is shown that the overall vortical motion is reduced by the imposed negative wall-normal velocity component while simultaneously the growth of unstable high-frequency secondary instability modes is attenuated that are located in a high-shear layer above the suction holes. Thereby, the associated flow field is stabilized and laminar-turbulent transition is significantly delayed or suppressed. A case with homogeneous suction at equal suction rate is shown to be virtually ineffective at this transition stage, while cases with slit suction, where the slits extend in spanwise direction, perform still well; however, the attenuation found in cases with concentrated hole suction is not reached. In all considered setups the suction-induced increased wall shear is by far overcompensated by the much stronger decrease due to the transition delay resulting in an overall effective drag reduction.

Zusammenfassung

Mit Hilfe von direkten numerischen Simulationen wird untersucht, ob der laminar-turbulente Umschlag in einer dreidimensionalen Pfeilflügelgrenzschicht durch konzentrierte Absaugung kontrolliert werden kann. Diese Methode stellt im Forschungsgebiet Laminarhaltung (laminar flow control) eine Möglichkeit dar, Strömungen an Pfeilflügeln von Verkehrsflugzeugen über weite Strecken laminar zu halten, auch wenn sich schon großamplitudige stationäre Querströmungswirbel mit aktiver instationärer Sekundärinstabilität entwickelt haben. Durch das Hinauszögern der Transition wird der Widerstand und damit der Treibstoffverbrauch erheblich reduziert, was gleichzeitig eine Reduktion der ausgestoßenen Treibhausgase bewirkt.

Bis heute wurde Laminarhaltung in Pfeilflügelgrenzschichten dadurch erreicht, dass die Primärinstabilität (Querströmungsinstabilität) reduziert und damit die Entwicklung stationärer großamplitudiger, sekundär instabiler Querströmungswirbel verzögert wurde. Die klassische, homogene Absaugung der Grenzschicht an der Wand reduziert die Querströmung in der Grenzschicht, was eine Abschwächung der Querströmungsinstabilität und damit ein späteres Einsetzen von Sekundärinstabilitäten und der Transition zur Folge hat. Das andere Laminarkonzept, bekannt als “distributed roughness elements” (verteilte Rauigkeitselemente) oder “distributed flow deformation” (verteilte Strömungsverformung), verspricht eine Unterdrückung der instabilsten Querströmungswirbelmoden durch die gezielte Anregung von schwach instabilen Moden, die nicht sekundär instabil sind. Die dadurch entstehenden “gutartigen” Wirbel liegen in Spannweitenrichtung näher zusammen als die natürlich angefachtesten, hindern sich gegenseitig im Wachstum aufgrund gleicher Rotationsrichtung und sättigen deshalb auf (für die Sekundärinstabilität relevantem) unterkritischem Amplitudenniveau. Das Wachstum anderer instabiler Moden wird durch die vorherrschenden Wirbel unterdrückt.

In der vorliegenden Arbeit wird im Gegensatz dazu ein dreidimensionaler, nichtlinearer Strömungszustand, der großamplitudige stationäre Quer-

strömungswirbel mit aktiver Sekundärinstabilität beinhaltet, durch konzentrierte (Loch-) Absaugung kontrolliert.

Im ersten Teil wird der Einfluss der Absauge-Modellierung auf die konzentrierte Absaugung untersucht. Das Modellieren von Lochabsaugung bietet generell den Vorteil, dass die numerischen Simulationen erheblich günstiger sind. Ergebnisse einer aufwändigen Simulation, in der die Kanalströmung unter der Absaugeöffnung mitsimuliert wird, werden hier mit dem zugehörigen, modellierten Fall verglichen. Obwohl sich die wandnormale Geschwindigkeitsverteilung in der Öffnung des simulierten Kanals von der modellierten Verteilung unterscheidet, sind die Auswirkungen auf den Querströmungswirbel bei gleicher abgesaugter Masse praktisch identisch und auch die Sekundärinstabilität wird in gleichem Maße abgeschwächt.

Im zweiten Teil der Arbeit wird gezeigt, dass konzentrierte Absaugung durch Löcher, die unterhalb der aufwärtsdrehenden Seite der Querströmungswirbel angebracht sind, die Wirbelbewegung reduziert, und zwar durch die dadurch überlagerte negative wandnormale Geschwindigkeitskomponente. Gleichzeitig wird das Wachstum instabiler, sekundärer Hochfrequenzinstabilitätsmoden abgeschwächt, die sich in einer Scherschicht über den Absaugelöchern befinden. Das Strömungsfeld wird dadurch stabilisiert und das Einsetzen von laminar-turbulenter Transition erheblich verzögert oder unterdrückt. Eine Simulation mit homogener Absaugung bei gleicher Absaugerate zeigt einen nur schwachen Einfluss in diesem nichtlinearen Stadium der Transition. Schlitzabsaugung mit wenigen spannwitigen Schlitzten liefert gute Ergebnisse; jedoch wird die Abschwächung durch konzentrierte Absaugung nicht erreicht. Das Ansteigen der absaugeinduzierten Wandschubspannung wird durch deren Verringerung als Folge der Transitionsverzögerung bei weitem überkompensiert, was in allen betrachteten Fällen zu einer Widerstandsreduktion führt.

Notation

Latin letters

A	amplitude or area
a	speed of sound
c	chord length
c_f	local skin friction coefficient
c_q	suction coefficient
d	diameter of suction holes
E	total energy
f_v	function for disturbance generation (vortex)
f_w	function for disturbance generation (wave)
h	timewise harmonic, see also subscript h or height coordinate in the cylindrical coordinate system
H_{12}	shape parameter
k	spanwise harmonic or roughness height
K	maximum number of spanwise harmonics
l	streamwise length of suction slits
(l)	time level
l_x	streamwise extension of applied homogeneous suction
L	reference length
\dot{m}	mass flux
Ma	Mach number
N_x, N_y, N_z	number of grid points in streamwise, wall-normal and spanwise direction
p	pressure
P	porosity
q	general flow quantity or velocity component $q = \sqrt{u^2 + w^2}$
r	radius or radial coordinate in the cylindrical coordinate system
Re	Reynolds number
Re_{kk}	roughness Reynolds number based on roughness height k and corresponding local velocity component u_k
s_x, s_z	streamwise and spanwise distance of suction-hole spacing
t	time or orientation of a high-shear layer plane (sec. 5.5.2)

T	temperature
T_0	fundamental period in time
u, v, w	velocity components in streamwise, wall-normal and spanwise direction
u_p	pseudo velocity component for boundary-layer evaluation
x, y, z	streamwise, wall-normal and spanwise coordinates
X, Y, Z	combined non-linear terms
x_0	start of the flow domain computed by the PNS equations
(x_{0r}, z_{0r})	origin of the rotated coordinate system
x_1	first disturbance-strip position
x_2	second disturbance-strip position
x_e	end of the flow domain computed by the PNS equations
x_{e12}, x_{s1}, x_{s2}	start and end coordinates of the first and second DNS domains for the compressible base-flow computation

Greek letters

α_i	amplification rate
α_r	streamwise wave number
β_H	Hartree parameter
δ_1	displacement thickness
δ_2	momentum thickness
δ, δ_{99}	boundary-layer thickness
Δ	Laplace operator or increment
$\tilde{\Delta}$	modified Laplace operator
$\Delta x, \Delta y, \Delta z$	step sizes of the computational grid in streamwise, wall-normal and spanwise direction
Δt	time step
ϕ	circumferential coordinate in the cylindrical coordinate system
ϕ_e	angle of the potential-streamline orientation with the x -axis
ϕ_r	rotation angle of the rotated coordinate system with the x -axis
γ	spanwise wave number
κ	ratio of specific heats (adiabatic index)
λ_z	spanwise wavelength
λ_2	vortex-visualization criterion
μ	dynamic viscosity

ν	kinematic viscosity
ρ	density
Θ	phase
ω	angular frequency
$\omega_x, \omega_y, \omega_z$	vorticity components in streamwise, wall-normal and spanwise direction
ξ, ζ	special rotated coordinate system where the origin coincides with the center of the suction hole

Subscripts

0	fundamental quantity
∞	quantity of the freestream
<i>avg</i>	average quantity
<i>b</i>	base-flow quantity
<i>CHAN</i>	quantity for case CHAN (simulation at Ma=0.7 with suction channel, sec. 4.3)
<i>comp</i>	quantity for a compressible case
<i>crit</i>	critical quantity
<i>e</i>	external quantity (outside the boundary-layer)
<i>exp</i>	experimental quantity
<i>h</i>	index for Fourier coefficient after expansion in time (partially performed for the second time derivative of the variable [9])
<i>incomp</i>	quantity for an incompressible case
<i>H</i>	quantity of a suction hole
<i>k</i>	index for Fourier coefficient after expansion in spanwise direction
<i>max</i>	maximum value
<i>mod</i>	quantity for modeled suction (incompressible simulations, sec. 2.1.2.2 and chap. 5)
<i>MOD</i>	quantity for case MOD (simulation at Ma=0.7 with modeled suction, sec. 4.3)
<i>r</i>	quantity in the rotated coordinate system
<i>s</i>	quantity in the streamline-oriented coordinate system
<i>t</i>	quantity evaluated along the orientation of a high-shear layer
<i>wall</i>	quantity at the wall $y = 0.0$

Superscripts

'	disturbance quantity
^	Fourier coefficient

Symbols

-	dimensional quantity
~	quantity divided by the local streamline-oriented velocity component of the base flow: $\tilde{q} = q/u_{b,s,e}$
*	complex conjugate
⟨ ⟩	mean quantity in time
	absolute value of a quantity

Abbreviations

3-d	three-dimensional
AKSA	Aktive Kontrolle von Störungen in der Aerodynamik (active control of disturbances in aerodynamics), LuFo project
CFV	crossflow vortex
DFD	distributed flow deformation
DLR	Deutsches Zentrum für Luft- und Raumfahrt (German Aerospace Center)
DRE	distributed roughness elements
DNS	direct numerical simulation
ERM	equivalent roughness model
IAG	Institut für Aerodynamik und Gasdynamik (Institute for Aerodynamics and Gas dynamics)
(H)LFC	(hybrid) laminar flow control
LST	linear stability theory
PLST, SLST	primary, secondary linear stability theory
PNS	parabolized Navier-Stokes (equations)
PSE	parabolized stability equations
T-S	Tollmien-Schlichting
UFD	upstream flow deformation
VER ² SUS	Verifikation eines vereinfachten Absaugesystems (verification of a simplified suction system), LuFo project

1 Introduction

One of the fundamental research fields in fluid dynamics is the investigation of laminar-turbulent transition in various flow scenarios. The transition process was first observed in 1883 by Osborne Reynolds in his famous pipe-flow experiment, where “coloured filaments” were added to the flow through a pipe showing first a well-ordered, laminar flow regime comprising straight color-particle lines that eventually became turbulent and resulted in strong mixing and finally even-colored fluid motion. Ever since the research of this phenomena was of enormous interest.

Around the turn of the century, Ludwig Prandtl proposed his concept of boundary-layer theory dividing a wall-bounded flow into a physically most relevant thin layer evolving near the body’s wall with dominating viscous effects and the remaining flow where viscosity can be neglected. Theoretical investigations by Osborne Reynolds, Lord Rayleigh and William Orr & Arnold Sommerfeld led to primary linear stability theory (PLST) that predicted wave-like perturbations in plane boundary layers to be damped or amplified depending on the detailed velocity profile and their frequency. The first satisfactory numerical results were published by Walter Tollmien and Hermann Schlichting in 1930.

An experimental milestone was set in 1947 by the work of Schubauer & Skramstad [75] who detected the predicted unstable two-dimensional Tollmien-Schlichting (T-S) waves for the first time in the boundary-layer flow on a flat plate with controlled disturbance input. Further experiments by Klebanoff et al. [36] in 1962 revealed three-dimensional ordered Λ -structures right before breakdown to turbulence, whereas Kachanov et al. [34] additionally found staggered ones in 1984. Today, the formation of these distinct three-dimensional structures is known as a consequence of secondary instability mechanisms (secondary linear stability theory, SLST, published in 1988 by Herbert [29]).

The two processes of transition to turbulence were named fundamental K-breakdown (K for Klebanoff) and subharmonic N- or H-breakdown (for Novosibirsk or Herbert). Including the oblique-type breakdown (first observed in numerical simulations by Fasel et al. [18]), the most important scenarios leading to turbulent flow in flat-plate boundary layers with low disturbance background were basically understood [85, 72].

In 1952, Gray observed that the transition process on a swept wing started much earlier than in the corresponding scenario on a straight wing [26]. By flow visualization he found closely-spaced stationary streaks very close to the leading edge - footprints of (later known as) stationary crossflow vortices (CFVs). Further work by P. Owen and D. Randall as well as H. Squire has been summarized in 1955 by Gregory et al. [28] who proposed the complete three-dimensional disturbance equations. Primary stability mechanisms have been elucidated by Mack in 1984 [46]. The secondary instability of (steady or traveling) CFVs, i.e. the physical mechanisms of transition to full turbulence in three-dimensional or swept-wing boundary layers, has only been completely clarified in the last decades and is described in section 1.1.

Besides theory and experiments, numerical simulations are nowadays a well-established field of research for the investigation of fluid-dynamic phenomena and can provide insight and explanation of successively more complex physical mechanisms considering the increasing computational resources. The first numerical solutions of the incompressible Navier-Stokes equations were reported in 1974 by Fasel [17]. In the 1990s, “correct *spatial*” direct numerical simulations (DNS) of the K-breakdown were conducted by Rist [66], and Kloker provided results for a strongly decelerated flow [37]. As of today, DNS codes can handle incompressible and compressible, fully three-dimensional flows on more complex integration domains, see, e.g. [6, 5], providing a powerful tool to not only validate experiments and offer highly-resolved flow physics but to investigate and predict completely new flow scenarios including, e.g., localized suction for boundary-layer control as in the current work.

Since laminar and turbulent boundary-layer flows are found in many technical applications the control of the boundary-layer state is of enormous interest. Triggering turbulence effectively enables, e.g., to improve combustion in an engine by strongly enhanced fuel-oxidant mixing. Also, since a laminar boundary

layer detaches more easily, turbulent boundary layers can ensure attached flow over a wind turbine blade, for example, providing higher efficiency, or over airplane control surfaces to warrant a reliable steering operation. On the other hand, a laminar boundary layer typically causes less drag or thermal load than a turbulent one. Maintaining laminar flow as long as possible and thus effectively reducing drag presents the main goal of the rapidly growing research field of laminar flow control (LFC). Aircraft manufacturers are forced to put a lot of effort in producing more efficient airplanes that allow airlines to decrease their direct operation costs regarding the increasingly expensive fuel. An Airbus advertisement for the new A350-1000 aircraft reads “while burning 25 percent less fuel than its nearest competitor” [1], while Boeing promotes the 787 laminar flow nacelle claiming “Laminar flow: The 787 nacelle was designed to maintain laminar flow over a longer portion of the nacelle than ever before” [2]. Furthermore, not only the economic but also the environmental aspect has gained growing interest and limiting greenhouse gas emission by regulators is at hand.

Until today, actually applied optimizations for new airplanes are limited to enhanced shaping, higher surface quality, and engine improvement, but little potential is thought to be left in these research fields using the proven aircraft shape. New concepts have therefore to be envisaged. According to Schrauf in 2005, LFC provides a total drag-reduction potential of up to 16% by, e.g., realizing 40% laminar flow on wings and tail planes of a current airliner [74].

Many investigations on LFC technologies including active T-S wave cancellation, boundary-layer suction, plasma actuators, to name a few, have shown the relevance and practical applicability of LFC for plane boundary layers. For three-dimensional (3-d) boundary layers, however, only little work on flow control by means of discrete suction is available and the gained knowledge from two-dimensional (2-d) flow scenarios cannot be simply transferred to 3-d boundary-layer flows since the physical effects are completely different.

1.1 Crossflow vortices and their secondary instability

The transition process for a boundary-layer flow depends mainly on the turbulence level of the oncoming flow, see e.g. [70]. For very high turbulence, a mechanism called *bypass transition* sets in and leads directly to turbulent flow. Bypass transition can also be caused by large roughness elements. For medium and low freestream turbulence different stages within the transition process can be distinguished. The first stage is called *receptivity*, where disturbances are generated inside the boundary layer resulting from sound waves, vibrations, vorticity fluctuations, or small roughness elements at the wall, just to name a few. A medium turbulence level can then provoke *transient growth* of the generated disturbances, where the interaction of two non-orthogonal modes leads to limited, but possibly large algebraic disturbance growth that can trigger transition to turbulence. For low turbulence levels, typically observed in free-flight conditions, the two following stages are usually observed: The generated small disturbances grow exponentially within the boundary layer according to *primary* LST. Next, *secondary* mechanisms are triggered that typically generate growing secondary disturbances and cause the final breakdown to turbulence. In the case of a two-dimensional boundary-layer flow the primary instability mechanism results in unsteady, two-dimensional T-S waves and, depending on their finite amplitude level and the disturbance background, secondary instability with subsequent either fundamental or subharmonic breakdown sets in. Another way to turbulence is caused by a non-linearly acting pair of oblique modes that are amplified strongest in plane boundary layers at high subsonic up to supersonic flow speeds. Breakdown occurs hereby in the absence of a large-amplitude primary T-S wave and the mechanism is called oblique breakdown.

For swept-wing boundary layers the underlying flow as well as the instability mechanisms are different. Due to wing sweep and chordwise pressure gradient an instability called *crossflow instability* sets in which is the dominant transition mechanism on airliner wings for sweep angles larger than 20-25°. The most important region where crossflow instability is active is located in the

favorable-pressure region on the wing which ranges approximately from the leading edge to the chord position with maximum thickness. (Further relevant instability mechanisms in a flow over a swept wing are the attachment line instability, the Görtler instability on the lower side of a wing with concave curvature, and the T-S instability in regions with pressure-gradient changeover, but are out of the scope of the current work.)

The crossflow instability is a result of curved potential streamlines that arise from a non-zero spanwise freestream-velocity component and a pressure-gradient component pointing to the curvature center of the streamlines that originates, e.g. on the front part of a swept-wing, from the chordwise acceleration of the flow. Considering the fluid motion outside the boundary layer, centrifugal forces and pressure forces are in equilibrium. Inside the boundary layer, as the velocity reduces close to the wall due to the no-slip condition, pressure forces overcome and a compensating flow (*crossflow*) component evolves, as sketched in figure 1.1, in a local potential-streamline-oriented coordinate system. The characteristic crossflow-velocity profile w_s appears orthogonal to the streamline orientation and has a distinct maximum at approximately 25% of the boundary-layer thickness. According to the inflection-point criterion (Rayleigh, Tollmien, and Fjørtoft), the occurring inflection point causes an inviscid instability. In contrast to Blasius boundary-layer flows, PLST predicts steady and unsteady unstable modes within spanwise wave number bands that are amplified with wave vectors nearly orthogonal to the direction of the local

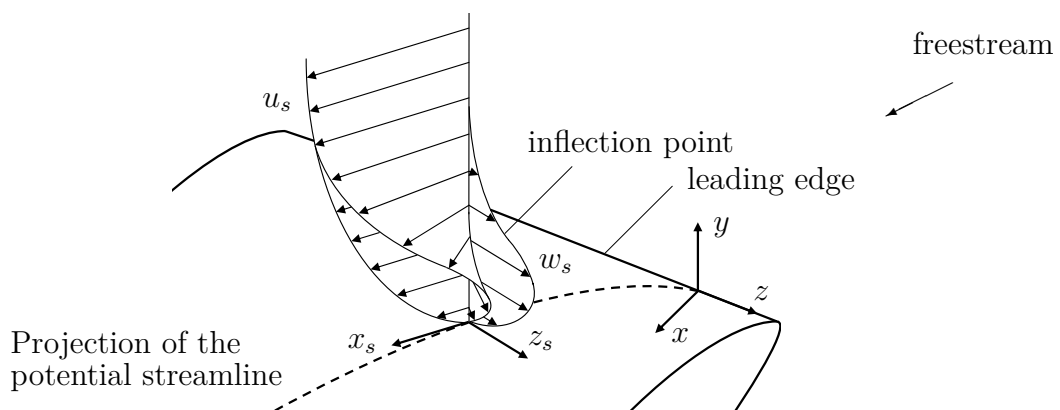


Figure 1.1: Typical velocity profile in a swept-wing boundary layer. Wing fixed, with oncoming flow.

streamwise velocity component. Steady or unsteady, longitudinal co-rotating CFVs develop as a consequence of the *primary instability* where the vortical motion close to the wall follows the crossflow direction. Typically, they are staggered in spanwise direction according to the naturally most amplified mode, and in smooth flight conditions steady CFVs are observed due to the higher receptivity of the flow to steady CFV modes.

The resulting flow field shows water-wave shaped streamwise velocity isocontours in flow crosscuts. Low-momentum fluid is transported away from the wall on the updraft side of each vortex while high-momentum fluid from outside the boundary layer is pushed towards the wall on the other side. The vortex-deformed flow reveals strong gradients of the streamwise velocity component and can be strongly unstable with respect to *secondary instabilities* depending on the CFV amplitude and state. In this case, small, finger-like secondary vortices develop in a typical scenario with unstable CFVs, winding up the updraft side of the main vortex. Fed by underlying exponential growth they rapidly grow, and tertiary structures in between the finger vortices trigger finally transition to turbulence.

Partially based on the reviews on stability of three-dimensional boundary layers by Reed and Saric [63, 71], the most important publications on secondary instability of CFVs are briefly summarized below.

Experimental work has been carried out by research groups at the DLR Göttingen, Germany [8], at the Arizona State University in Phoenix, AZ, USA [69, 84, 83], at the Tohoku University in Sendai, Japan [42, 35], and at Chalmers University of Technology in Göteborg, Sweden [15].

At the DLR, the so-called “Prinzipexperiment Querströmungsinstabilität” (a basic experiment on crossflow instability) was set-up by Bippes and co-workers [8] who studied steady and unsteady CFV modes including non-linear interaction. They found that in low-turbulence environments steady CFVs dominate whereas crossflow waves prevail in a higher-turbulence environment. Explosive growth of secondary instability modes leads to transition in the CFV scenario whereas transition in the unsteady case sets in comparably slowly. White & Saric and co-workers at the ASU [69, 84, 83] focused on low-turbulence cases with the controlled excitation of steady CFVs and pro-

vided well-resolved investigations on secondary-instability growth. Kawakami, Kohama and co-workers [42, 35] found secondary instability of CFVs for both the steady and unsteady fundamental scenarios on a flat plate at Tohoku University. Chernoray and co-workers investigated the steady case at Chalmers University [15] providing growth rates for secondary amplification and studied the interaction of large-amplitude CFVs.

Theoretical work, namely the development of a SLST model, has been mostly carried out using the parabolized stability equations (PSE) to calculate nonlinear solutions for unstable CFV modes, see publications by Balachandar, Malik, Koch, and Reed [7, 51, 52, 41, 40, 62]. Three different classes of secondary instability modes were identified, namely the high-frequency mode I or z -mode related to the minimum of the spanwise gradient of the streamwise velocity component, the high-frequency mode II or y -mode, related to the maximum of the wall-normal gradient, and a low-frequency type III mode related to the maximum spanwise gradient.

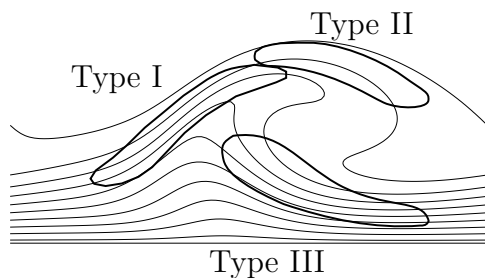


Figure 1.2: Location of different types of secondary instability modes.

that secondary growth rates are very sensitive to the primary state (i.e. the underlying vortex-deformed base flow) and particularly to moderate artificially induced wall-normal and crossflow velocity components. They concluded that the reported differences originated most likely from ambiguities and possibly also inaccuracies in the base-flow extraction technique for the SLST calculations. Furthermore they suggested that this sensitivity might open a door for transition control which lead to the initial idea of pinpoint suction proposed in the current work.

Results from DNS have been mainly reported by three groups: Based on the temporal model (with timewise growth and fixed streamwise periodicity

The location of the respective modes is sketched in figure 1.2. Discrepancies between SLST and experiments regarding growth rates of secondary instability modes as e.g. reported by White & Saric [83] were investigated later thoroughly by Bonfigli & Kloker [12]. Based on their results from SLST and DNS they found

of the flow) the Kleiser group at ETH Zürich, Switzerland, investigated the nonlinear development of stationary and traveling crossflow modes but details on the secondary instability of steady CFVs were not given [87, 88, 86]. Investigations employing spatial DNS were first reported by the Swedish work group at KTH, Stockholm, Sweden by Högberg & Henningson in 1998, who found the highest amplification rates for the high-frequency z -mode [30]. The DNS group in Stuttgart provided first results in 1995 where some aspects of interaction between steady and unsteady modes were clarified [59]. Succeeding publications by Bonfigli & Kloker [11, 10] showed very good agreement with results from the DLR “Prinzipexperiment”. As of 2002, Wassermann & Kloker used a wing-generic base flow for their investigations of steady and unsteady fundamental cases [80, 81, 82] and provided fully detailed insights into the secondary-instability and breakdown mechanisms. They also provided conclusive and detailed visualizations of the actual flow fields in very good agreement with available data from theory [52] and experiments [83].

A concept of swept-wing boundary-layer control without the help of suction has been introduced by Saric and co-workers at Arizona State University, and by Wassermann & Kloker at Stuttgart University. Saric proposed the distributed-roughness-elements (DRE) technique [68, 69], for a recent overview see [67]. A one-time excitation of steady CFVs that are spaced narrower in the spanwise direction than the naturally most amplified ones enforces a flow scenario with, at first, secondarily stable CFVs and thus delays transition to turbulence by suppressing other, further downstream more unstable CFV modes. The upstream-flow-deformation concept (UFD), proposed in Stuttgart [80], pursues a similar goal, however, not necessarily based on roughness. Currently, investigations are started in the LuFo project AKSA where the base flow of the DLR “Prinzipexperiment” is to be controlled by the DRE/UFD technique both numerically and experimentally using pneumatic and plasma actuators.

1.2 Discrete suction for laminar flow control

Mainly driven by rising fuel prices intense research on LFC with the help of boundary-layer suction has been carried out within the last decades. For plane

boundary-layer flows without crossflow, (homogeneous) suction at the wall has been shown to significantly delay transition to turbulence by pulling high-momentum fluid towards the wall, thus enforcing fuller streamwise-velocity profiles which lead to attenuated growth of Tollmien-Schlichting (T-S) instability waves, see e.g. [65].

As for swept-wing boundary layers, suction has until now been employed for a reduction of the basic crossflow and thus to weaken primary instability resulting in attenuated (primary) vortex growth and postponed transition.

Starting in the early 1960s, several **flight campaigns** were conducted in the USA and Europe. Based on the overviews by Joslin [33, 32] and Braslow [13] the most important ones are mentioned here briefly (see also [56]):

Spanwise suction slits employed in the Northrop X-21 flight tests in the 1960s showed successful transition delay on 30° -swept wings at a global Reynolds number of 20 millions, but never entered regular operation since it was too difficult to keep the slits clean [61]. For the NASA Jetstar campaign in the 1980s laminar flow on a wing glove with perforated suction panels (suction hole diameters of $65\mu\text{m}$) was reported [50]. Flight tests on a Boeing 757 employed a complete suction system for the wing and 65% laminar flow could be maintained at $\text{Ma}=0.82$ and a global Reynolds number of 30 millions [49]. In France, 30% laminar flow was achieved at 30° wing sweep on a Falcon 50 in the late 1980s at small suction rates [14]. An Airbus A320 fin test was conducted in 1998 at $\text{Ma}=0.8$ and laminar flow up to 50% was reported but detailed information on the suction system parameters was not provided [77].

To date, suction systems are still far from mass production but both Airbus and Boeing are currently setting up new flight campaigns: The Boeing ZA003 test aircraft which is a 787-9 airplane employs a hybrid laminar flow control (HLFC) surface including suction in a limited area on the leading edge of the vertical stabilizer, one-quarter to one-half the way up the fin, and started operation in November 2011. No publications are available yet. Airbus focuses on a “simplified” suction system and a 1:1 wind-tunnel model of a vertical stabilizer that is currently developed and built at the DLR Göttingen comprising suction panels with suction hole diameters of $50\text{-}100\mu\text{m}$ within the LuFo Project VER²SUS (Verifikation eines vereinfachten Absaugesystems, verification of a

simplified suction system). Experiments and flight tests are planned in the near future.

The perfect homogeneous suction panel that does not induce any disturbances is mostly approximated by suction-hole or suction-slit arrays which inherently comprise the excitation of disturbances with finite stream- or spanwise wavenumbers. Thus, various experiments as well as numerical investigations have been carried out in the last decades to gain a deeper understanding of mechanisms occurring in a boundary layer with discrete suction. Furthermore, the focus was on a mechanism often referred to as “oversuction” where suction-induced early transition to turbulence is triggered due to too large suction rates.

As for **discrete suction in two-dimensional boundary layers**, the first publications date back to 1957 where Goldsmith [25] investigated the influence of suction-hole mass-flux variations on a pipe flow with closely-spaced suction holes. At low suction rates, a pronounced counter-rotating stationary vortex pair was visible behind each hole turning such that high-momentum fluid was transported towards the wall in between the vortices (see figure 1.3a) but no premature transition could be observed. At high suction rates, additionally, horseshoe vortices connecting adjacent holes occurred that detached periodically in time and caused early transition. Meitz & Fasel provided DNS results for the pipe-flow experiments and found seemingly good agreement for the threshold of critical suction rates that triggered early transition [54, 53]. (However, recent extensive numerical resolution studies within the current work, see appendix B, have shown that these results are not converged and that a much finer grid in the wall-normal direction is necessary to correctly resolve the occurring suction phenomena with the vorticity–velocity code used.)

Gregory [27] investigated the variation of the suction-hole diameters and the spanwise spacing of the holes experimentally and found increasing critical suction rates (i.e. higher rates are needed for triggering turbulence) with decreased diameters or increased hole spacing.

Reneaux & Blanchard tried to design perforation patterns allowing for high suction rates without inducing transition and therefore investigated systematically the influence of two hole patterns. Their “triangular” pattern performed

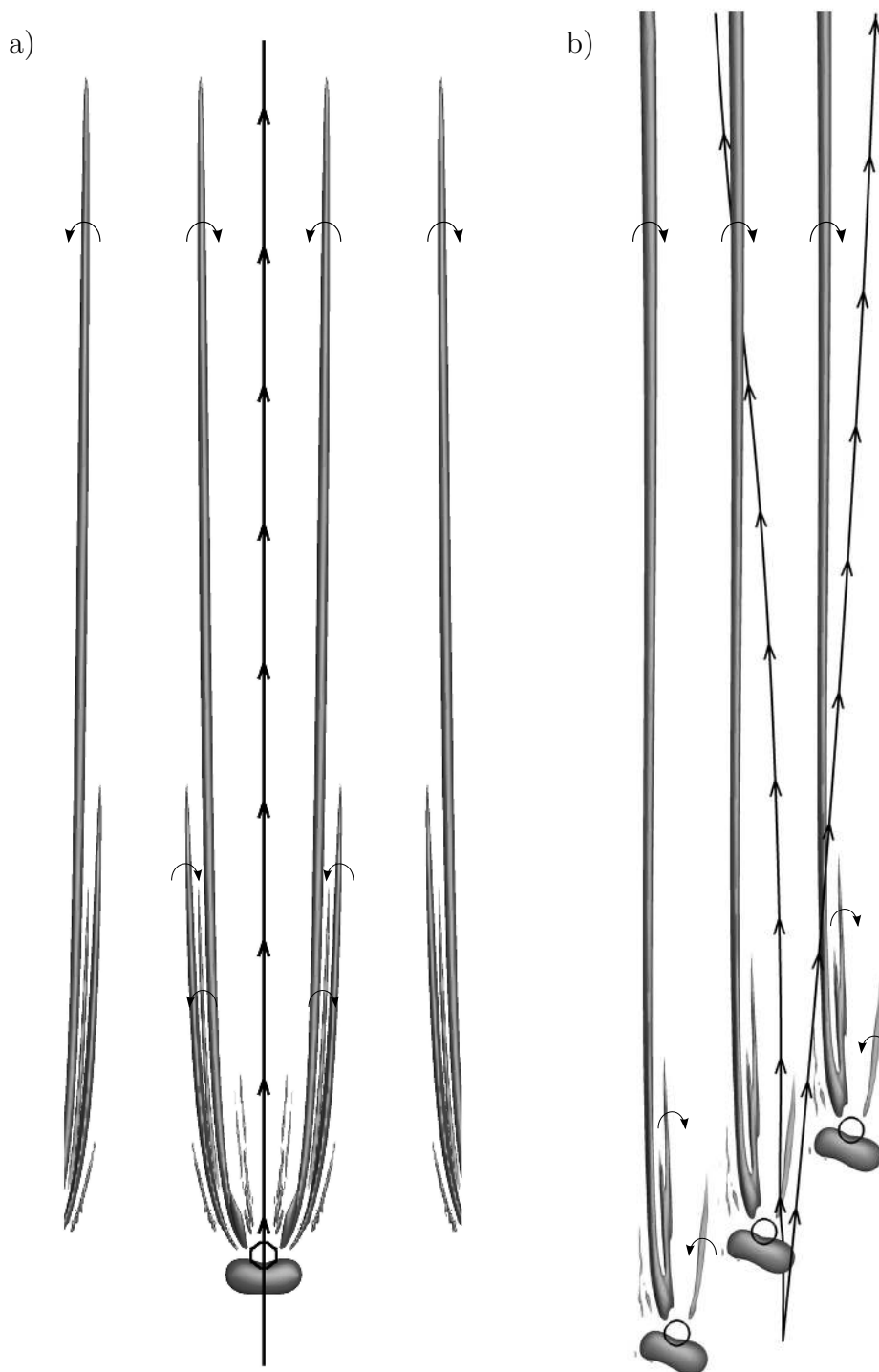


Figure 1.3: Vortical structures caused by suction through a spanwise row of holes in a Blasius boundary layer (a) and an accelerated boundary layer with crossflow (b). The flow direction is indicated by streamlines. In (b), the potential and wall-near flow is visualized by streamlines above and below the CFVs; crossflow is from right to left. For simulation details see appendix A.

better than their “square” pattern which was explained by an “increased distance between holes for a given streamline” [64]. Today it is known that staggered hole patterns in two-dimensional boundary layers provide an effective method to reduce pattern-induced disturbances since succeeding staggered suction holes create modes in anti-phase that can cancel each other.

MacManus & Eaton [48] provide experimental and numerical results for HLFC suction surfaces. They confirm the complex nature of flow phenomena evolving behind single suction orifices and suction panels at varying suction rates and provide a critical suction design based on measured and predicted streamtube characteristics. They query a critical suction parameter suggested by Reneaux & Blanchard based on a rectangular shape of the streamtube and state that Goldsmith’s parameter G_k performs better since his assumed round shape was more realistic. Based on their experiments they correlate G_k with Re_{kk} , the Reynolds number based on the streamtube height, and find a linear relationship allowing for the derivation of a critical suction Reynolds number $Re_{kk} = 890$.

Müller, Friederich & Kloker summarized and examined investigations on roughness analogies for strong discrete suction by means of spatial DNS [58]. Comparisons with results reported by MacManus & Eaton showed unacceptable deviations. As it turned out, the Reynolds-number variation of MacManus’ experiments was too weak and thus the roughness analogy and the derived critical suction parameter is valid for a small Re_{δ_1} -range only. This conclusion was confirmed evaluating experimental results by Reneaux & Blanchard who covered a broader Re_{δ_1} -range. The proposed critical suction value of $Re_{kk} = 890$ by MacManus was refuted. Several cases with strong modeled hole suction in a Blasius boundary layer revealed oversuction to set in only above Re_{kk} -values of 1400 to 1700, where suction-induced unsteadiness of the resulting counter-rotating vortex pair was observed. Horseshoe-type secondary vortices, located almost symmetrically above each vortex caused by a y -mode were found to be responsible for triggering breakdown to turbulence. The results were confirmed with a simulation comprising the channel flow below the suction hole showing that the flow field with channel is slightly more stable than in the case with modeled suction. However, a simulation revealing oversuction including the channel flow has not been accomplished.

The presence of crossflow constitutes a fundamental change of physical effects as for **discrete suction in three-dimensional boundary layers**. Messing & Kloker [56] point out that “any direct transfer of findings gained from two-dimensional boundary layers to three-dimensional boundary layers is almost always misleading or even impossible”. They provide an example, where MacManus & Eaton [47] addressed the problem of possible interaction between suction-induced vortices and CFVs. Assuming that two counter-rotating vortices evolve behind a suction hole in a 3-d boundary layer MacManus identified wrong length scales relevant for nocent interaction and disturbance amplification. Indeed, two counter-rotating vortices can be discovered right behind the suction hole, but the one turning against the crossflow near the wall is damped instantly, cf. figure 1.3b. Recall also that steady modes excited by suction holes are not exponentially and continuously amplified in the Blasius flow but, depending on their spanwise spacing, can be exponentially amplified in a 3-d boundary layer.

Experiments on discrete suction in three-dimensional boundary layers turn out to be very complex and have been carried out only at ONERA, France and at DLR Göttingen, Germany.

In 2000, Arnal and co-workers managed to successfully delay transition on a 50° swept wing with cylindrical nose using $45\mu\text{m}$ suction holes at $1200\mu\text{m}$ spanwise spacing. Increased initial amplitudes caused by the suction holes were overcompensated by a reduction of CFV growth [4].

Abegg and co-workers modified the DLR “Prinzipexperiment” by introducing two suction chambers at 16% and 35% chord. Metal sheets containing chordwise slits or suction holes could be mounted. After measuring and comparing the different initial amplitudes introduced by the suction orifices they concluded that an appropriate design of suction panels should allow for minimizing the excitation of steady three-dimensional disturbances [3]. As already noted by Messing & Kloker [56] one fundamental flaw of these experiments however was that the perforated metal sheets were designed for free-flight experiments. Similarity parameters like d/δ_1 , s_z/δ_1 , s_x/δ_1 (d : suction hole diameter, δ_1 : displacement thickness, s_z , s_x : spanwise, chordwise spacing of the suction holes) were therefore not kept constant since the freestream velocity was about one order of magnitude smaller in the wind tunnel. Moreover, the

unstable wavelengths are then one order of magnitude larger which means that the hole spacings were unrealistically subcritical.

Besides the publications by scientists from Stuttgart University results of **DNS on discrete suction in 3-d boundary layers** have only been provided by Spalart in 1993 [76]. His goal was to simulate by-pass transition by strong suction but he ended up obtaining steady saturated CFVs only. His explanations at the chosen parameters (likely to cause premature transition) are the smooth shape of the modeled hole-suction distribution, the perfect spanwise periodicity, or the omission of time-dependent forcing. Furthermore, he states that “the number of parameters is daunting” regarding the wide parameter space for the expensive simulations of oversuction. Simulations with succeeding rows of suction holes showed damped amplitude development right after the first hole rows, but at some streamwise distance crossflow modes started to grow right behind the holes, induced by the suction panel.

In Stuttgart, results with discrete, modeled suction in 3-d boundary layers were published by Messing & Kloker [55, 56]. They showed the survival of only one vortex behind a single suction hole since the one rotating against the crossflow near the wall is damped. They also analyzed suction panels consisting of slits and holes that included small manufacturing imperfections and showed that subcritically designed suction panels, i.e. inducing in the optimal case only smaller spanwise wavelengths than the amplified ones, can excite unstable vortex eigenmodes. In one case (“overcritical suction”) they proved that secondary instability can set in on an active suction panel. Furthermore, they proposed a combination of UFD and suction leading to the concept of distributed flow deformation (DFD) and in particular “formative suction”. A panel was designed such that narrow-spaced useful vortices were continuously excited and maintained, suppressing other unstable modes and thus enhancing the positive effect of bare suction. It was also shown that succeeding panels can be adapted to the altering stability characteristics of the base flow when proceeding downstream and hence continuously excite the locally optimal DFD mode.

Müller, Friederich & Kloker investigated oversuction in the three-dimensional DLR “Prinzipexperiment” base flow [58] employing compressible DNS. They found a suction-induced vortex pair behind the suction holes where the one

turning against the crossflow was damped instantly, and for large suction rates self-induced unsteadiness lead to transition to turbulence which was considered oversuction. The resulting secondary structures resembled the ones found in their overcritical two-dimensional case. A comparison of relevant unstable secondary modes of an undercritical and an overcritical case revealed the changeover from a typical, naturally evolving high-frequency z -type mode to a suction-induced y -type mode. The corresponding Re_{kk} -values were 627 (undercritical) and 876 (overcritical). A comparison with values found in the Blasius case shows strong deviations and trying to constitute a universally valid critical Reynolds number (for two- and three-dimensional flows) is questionable considering the fundamentally different underlying base flows.

1.3 Goals, methods and overview

Up to date, the challenging task of LFC in swept-wing boundary layers applied for drag reduction has been tackled by influencing primary crossflow instability only. Approaches with bare suction aim at a reduction of the basic crossflow to reduce primary instability. Thereby, the growth of CFV modes and the development of large-amplitude CFVs is weakened which results in later-induced secondary instability and delayed laminar-turbulent transition. A similar goal is pursued by the DRE and UFD methods, however the primary-growth reduction is here achieved by, at first, stable CFVs that are spaced closer than the naturally most amplified ones. These nonlinearly large CFVs cause a mean flow alteration similar to suction. The DFD method combines this effect and suction and furthermore provides a possibility to adapt the panel to changing stability characteristics of the base flow by locally exciting and maintaining the correct, benign DFD vortices.

The concept of LFC proposed in the current work aims at a direct control of the secondary crossflow instability by means of localized “pinpoint” suction. The investigated base flow contains nonlinearly large and secondarily unstable steady CFVs that would naturally develop in the flow near the leading edge on a swept wing at cruise flight and cause early transition to turbulence. The flow setup corresponds to the DLR Göttingen “Prinzipexperiment”

[8, 12] where a swept flat plate with a displacement body above was employed. It is a model flow for the boundary layer developing on the upper side of a swept-back airplane wing within the region of accelerated flow. Located below the updraft side of each CFV, “pinpoint” suction holes are activated at the wall such that the vortical motion is weakened by the imposed negative wall-normal velocity component which simultaneously attenuates the growth of unstable high-frequency secondary instability modes, see also [12] and first tentative studies [21, 39]. The accompanying transition delay leads to a possibly large overall drag reduction at considerably lower suction rates compared to standard (homogeneous) suction.

The incompressible high-order DNS code developed at the institute is employed for the investigation of various suction scenarios realized by modeled velocity distributions within the wall boundary condition. It is chosen due to its excellent numerical performance.

To check the influence of the suction-hole modeling a numerically extensive compressible simulation is carried out where the channel flow below the suction orifice is included in the simulation and the result is compared to a modeled-suction case. The DNS are performed for a freestream Mach number $Ma_\infty = 0.7$ to (i) exploit the improved performance of the compressible code compared to $Ma_\infty = 0.05$ for the “Prinzipexperiment”, and (ii) to check the influence of a Mach number relevant to airliner flight.

The structure of the dissertation is as follows: The numerical methods are described in chapter 2. The underlying base flows and characteristics are introduced in chapter 3, followed by the comparison of simulations with modeled and simulated hole suction in chapter 4. The main results of secondary instability control by (modeled) pinpoint suction for incompressible flow are provided in chapter 5.

2 Numerical methods

The origin of solving the incompressible Navier-Stokes equations numerically for stability investigations dates back to the work by Fasel in 1974 [17]. Rist [66], Konzelmann [43] and later Kloker [37] developed the basic numerical scheme for the actual code. Including the improvements by Wassermann [79] and Bonfigli [9] the applied numerical method is capable of solving the full three-dimensional unsteady incompressible Navier-Stokes equations for spanwise periodic, asymmetric three-dimensional flows using high-order spatial and timewise discretization schemes. A detailed overview of the historical development can be found in [79, 55, 9].

The compressible numerical method is based on the work by Thumm [78] and improvements by Kloker [38], Eissler [16], Fezer & Kloker [19], and Pagella [60]. Due to rising scientific and computational demands a new compressible code was developed by Babucke et al. [6]. It solves the full three-dimensional unsteady compressible Navier-Stokes equations using high-order spatial and timewise discretization schemes. The current code, further adapted especially for spanwise asymmetric flows within the pinpoint suction investigations allows for simulating the disturbance development in 3-d boundary layers, similarly to the incompressible method, but comprises also a module to include the flow in an attached cylindrical domain (e.g. a cylindrical blowing or suction channel).

The incompressible and compressible numerical methods are described in sections 2.1 and 2.2 followed by a verification of the numerical methods in section 2.3.

2.1 Incompressible numerical method

The full three-dimensional unsteady incompressible Navier-Stokes equations are solved in vorticity-velocity formulation. A rectangular integration domain

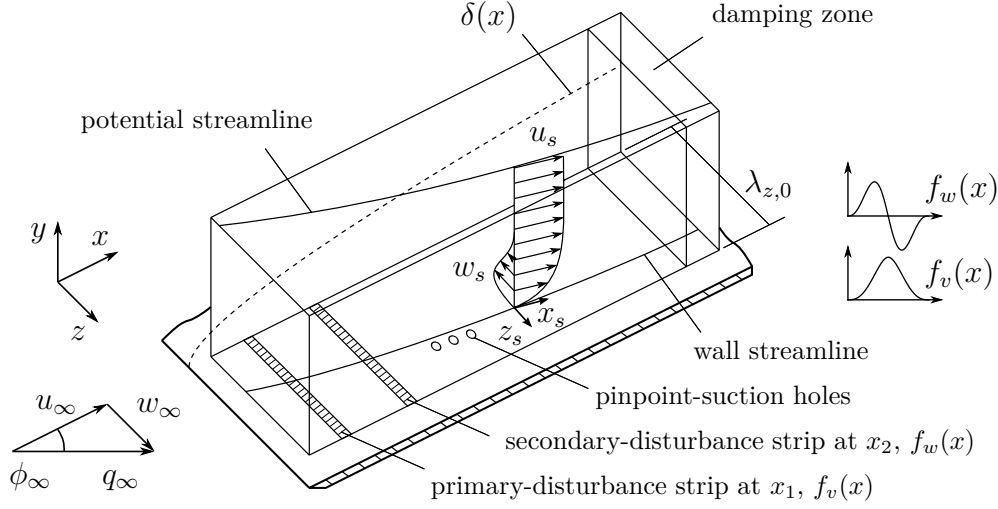


Figure 2.1: Integration domain. For details on coordinate systems see appendix D.

on a flat plate is considered as shown in figure 2.1. The computational Cartesian reference system (x, y, z) denotes chordwise, wall-normal and spanwise direction. The corresponding velocity vector is $(u, v, w)^T$, and the following definition of the vorticity components is considered:

$$\omega_x = \frac{\partial v}{\partial z} - \frac{\partial w}{\partial y}, \quad \omega_y = \frac{\partial w}{\partial x} - \frac{\partial u}{\partial z}, \quad \omega_z = \frac{\partial u}{\partial y} - \frac{\partial v}{\partial x}. \quad (2.1)$$

All flow quantities are non-dimensionalized using the reference length $\bar{L} = 0.1m$ and the reference velocity $\bar{u}_\infty = 14.0m/s$ (the overbar indicates dimensional values) unless otherwise stated. The Reynolds number is $Re = \bar{u}_\infty \bar{L} / \bar{\nu} = 92000$. The non-dimensional variables are

$$\begin{aligned} x &= \frac{\bar{x}}{\bar{L}}, & y &= \frac{\bar{y}}{\bar{L}}, & z &= \frac{\bar{z}}{\bar{L}}, \\ u &= \frac{\bar{u}}{\bar{u}_\infty}, & v &= \frac{\bar{v}}{\bar{u}_\infty}, & w &= \frac{\bar{w}}{\bar{u}_\infty}, \\ \omega_x &= \frac{\bar{\omega}_x \cdot \bar{L}}{\bar{u}_\infty}, & \omega_y &= \frac{\bar{\omega}_y \cdot \bar{L}}{\bar{u}_\infty}, & \omega_z &= \frac{\bar{\omega}_z \cdot \bar{L}}{\bar{u}_\infty}, \\ t &= \bar{t} \cdot \frac{\bar{u}_\infty}{\bar{L}}. \end{aligned} \quad (2.2)$$

The three vorticity transport equations and three Poisson equations for the velocity components represent a non-linear coupled system of partial differential

equations, where Δ is the Laplace operator:

$$\frac{\partial \omega_x}{\partial t} + \frac{\partial}{\partial y}(v\omega_x - u\omega_y) - \frac{\partial}{\partial z}(u\omega_z - w\omega_x) = \frac{1}{Re}\Delta\omega_x, \quad (2.3a)$$

$$\frac{\partial \omega_y}{\partial t} - \frac{\partial}{\partial x}(v\omega_x - u\omega_y) + \frac{\partial}{\partial z}(w\omega_y - v\omega_z) = \frac{1}{Re}\Delta\omega_y, \quad (2.3b)$$

$$\frac{\partial \omega_z}{\partial t} + \frac{\partial}{\partial x}(u\omega_z - w\omega_x) - \frac{\partial}{\partial y}(w\omega_y - v\omega_z) = \frac{1}{Re}\Delta\omega_z, \quad (2.3c)$$

$$\frac{\partial^2 u}{\partial x^2} + \frac{\partial^2 u}{\partial z^2} = -\frac{\partial \omega_y}{\partial z} - \frac{\partial^2 v}{\partial x \partial y}, \quad (2.3d)$$

$$\Delta v = \frac{\partial \omega_x}{\partial z} - \frac{\partial \omega_z}{\partial x}, \quad (2.3e)$$

$$\frac{\partial^2 w}{\partial x^2} + \frac{\partial^2 w}{\partial z^2} = \frac{\partial \omega_y}{\partial x} - \frac{\partial^2 v}{\partial y \partial z}. \quad (2.3f)$$

Each flow quantity q is split into its steady base-flow component $q_b(x, y)$ and perturbation component $q'(t, x, y, z)$ which are computed consecutively. This procedure allows for setting optimal boundary conditions in each case. Note that the time mean $\langle q' \rangle$ is non-zero for large q' in the perturbation simulation, and that no simplifications of the equations are introduced with this ansatz.

2.1.1 Computation of the steady spanwise-invariant base flow

The three-dimensional base flow (subscript b) is assumed to be independent of the spanwise direction (infinite wing assumption). Nevertheless, w_b , $\omega_{x,b}$, and $\omega_{y,b}$ are non-zero which results in curved potential streamlines for $u_{b,e} = f(x)$. If all derivatives with respect to z are neglected the base-flow equations can be derived from the equation system (2.3). In contrast to standard codes that tackle the complete system at once the procedure developed by Bonfigli (for details on the numerical implementation and validation of the code see [9]) solves the two-dimensional problem for u_b , v_b , $\omega_{z,b}$ in a first step before the remaining three flow quantities for the three-dimensional problem w_b , $\omega_{x,b}$, $\omega_{y,b}$ are computed hereafter. This is a consequence of the independence principle holding for spanwise invariant flows.

As for the inflow boundary condition the quantities v_b , w_b and $\omega_{z,b}$ are prescribed as a function of the wall-normal coordinate y employing Falkner-Skan

profiles with a Hartree parameter $\beta_h = 2/3$. Small adaptations were necessary to match the experimental flow, see also section 3.2. At the outflow all second derivatives with respect to x are neglected and the remaining equations are solved. The freestream consists of a prescribed $u_b(x)$ -velocity field which is derived from the experimental pressure distribution. Furthermore, the constant spanwise velocity component w_b and vanishing vorticity $\omega_{x,b} = \omega_{y,b} = \omega_{z,b} = 0$ are prescribed. The no-slip and no-penetration condition $u_b = v_b = w_b = 0$ forms the boundary condition at the wall. A fictive time development is applied to obtain a steady-state solution.

2.1.2 Computation of the perturbation flow

Once the steady base flow is computed, the extensive unsteady perturbation simulation can be set up. The boundary conditions at the wall allow for the input of controlled steady and unsteady disturbances that are periodic in spanwise direction. Furthermore, suction slits and holes can be turned on and the spatial downstream development of all perturbations is simulated. In order to (i) keep the integration domain short and (ii) easily check for secondary instability of grown CFVs, unsteady, pulse-like disturbances are continuously forced in a disturbance strip.

The basic numerical method has been described in detail by Wassermann & Kloker [80] and Bonfigli & Kloker [12]. Modifications were made by Messing [55] who implemented a wall boundary condition that allows for modeled suction through slits, slots, and holes. He furthermore added a direct solver for the v -Poisson equation achieving a speed-up of the code. The advancement by Meyer [57] included the porting to Fortran 90, improved parallelization, and stretched-grid handling in wall-normal direction. This was realized by calculating biased compact finite differences adapted to the base-flow grid and resulted in savings of up to 50% of the grid points at similar spatial resolution near the wall.

The code is based on sixth-order compact finite differences alternatingly forward/backward biased in x - and central in y -direction, whereas the z -direction is discretized by a fully complex Fourier expansion. The general perturbation

flow quantity q' is decomposed into

$$q'(t, x, y, z) = \sum_{k=-\infty}^{\infty} \hat{q}'_{(k)}(t, x, y) \cdot e^{ik\gamma_0 z}, \quad \gamma_0 = \frac{2\pi}{\lambda_{z,0}}, \quad i^2 = -1, \quad (2.4)$$

where γ_0 is the fundamental wave number in spanwise direction. The coefficients $\hat{q}'_{(k)}$ with $k < 0$ need not be computed since $q'_{(k)} = q'_{(-k)}^* \quad \forall k$, where the asterisk indicates complex conjugates. However, both imaginary and real parts of the equations have to be solved.

For time integration a four-step explicit fourth-order Runge-Kutta scheme is originally implemented.

The code was tested and verified for weak suction by Messing & Kloker [56]. In the current work it was found that for higher suction rates an extremely well-resolved grid in wall-normal direction is needed near the wall; see grid studies in appendix B and also the discussion of figure 4.11. Since the numerical time-step limit then is of viscous type $\Delta t_{max} \sim \Delta y_{wall}^2$, simulations with the explicit Runge-Kutta O4 time integrator turned out to be no longer feasible. Thus, a semi-implicit time integration scheme was developed and implemented which is described in section 2.1.2.4.

2.1.2.1 Governing equations

After applying the decomposition (2.4) to the equation system (2.3), all flow quantities are split into their base-flow and perturbation parts and the zero-sum base flow is subtracted. The following perturbation equations have to be solved for the Fourier coefficients:

$$\frac{\partial \hat{\omega}_{x,(k)}}{\partial t} = \frac{1}{Re} \tilde{\Delta}_k \hat{\omega}_{x,(k)} + \hat{X}_{(k)} \quad \forall k, \quad (2.5a)$$

$$\frac{\partial \hat{\omega}_{y,(k)}}{\partial t} = \frac{1}{Re} \tilde{\Delta}_k \hat{\omega}_{y,(k)} + \hat{Y}_{(k)} \quad \forall k, \quad (2.5b)$$

$$\frac{\partial \hat{\omega}_{z,(k)}}{\partial t} = \frac{1}{Re} \tilde{\Delta}_k \hat{\omega}_{z,(k)} + \hat{Z}_{(k)} \quad \forall k, \quad (2.5c)$$

$$\frac{\partial^2 \hat{u}_{(k)}}{\partial x^2} - (k\gamma)^2 \hat{u}_{(k)} = -ik\gamma \hat{\omega}_{y,(k)} - \frac{\partial^2 \hat{v}_{(k)}}{\partial x \partial y} \quad k \neq 0, \quad (2.5d)$$

$$\frac{\partial \hat{u}_{(k)}}{\partial x} = -\frac{\partial \hat{v}_{(k)}}{\partial y} \quad k = 0, \quad (2.5e)$$

$$\tilde{\Delta}_k \hat{v}_{(k)} = ik\gamma \hat{\omega}_{x,(k)} - \frac{\partial \hat{\omega}_{z,(k)}}{\partial x} \quad \forall k, \quad (2.5f)$$

$$\frac{\partial^2 \hat{w}_{(k)}}{\partial x^2} - (k\gamma)^2 \hat{w}_{(k)} = \frac{\partial \hat{\omega}_{y,(k)}}{\partial x} - ik\gamma \frac{\partial \hat{v}_{(k)}}{\partial y} \quad k \neq 0, \quad (2.5g)$$

$$\frac{\partial \hat{w}_{(k)}}{\partial x} = \hat{\omega}_{y,(k)} \quad k = 0. \quad (2.5h)$$

The Laplace operator with a spectral z -derivative now reads:

$$\tilde{\Delta}_k = \frac{\partial^2}{\partial x^2} + \frac{\partial^2}{\partial y^2} - (k\gamma)^2. \quad (2.6)$$

The nonlinear convective terms of the momentum equations are called $\hat{X}_{(k)}$, $\hat{Y}_{(k)}$ and $\hat{Z}_{(k)}$ and include base-flow as well as perturbation quantities. These terms are generally dependent on all Fourier harmonics and therefore form the coupling between the spanwise modes. If a truncated Fourier sum for the decomposition (2.4) is introduced by choosing $-K \leq k \leq +K$, the equation system (2.5) represents $K + 1$ complex differential equations.

2.1.2.2 Boundary conditions

Inflow: All perturbations are set to zero. (The disturbances are introduced far enough downstream of the beginning of the integration domain.)

Outflow: All second derivatives with respect to x are locally neglected. Most importantly, a preceding damping zone reduces all perturbations of the vorticity vector and the wall-normal velocity component v as well as very low values of u and w to zero [37, 11].

Freestream: Vanishing vorticity and an exponential decay of the wall-normal velocity according to linear stability theory are prescribed:

$$\frac{\partial v'}{\partial y} = -\alpha^* v'. \quad (2.7)$$

The constant is defined as $\alpha^* = \sqrt{\alpha_r^2 + (k\gamma_0)^2}$ for all k . According to Messing [55], cases that include wall suction require $\alpha^* = 0$ for $k = 0$, since the two-dimensional part of v' does not decay outside the boundary layer. The remaining α^* -values for $k > 0$ stay unaffected for cases with suction.

Perturbation strips at the wall: Perturbation strips are activated by prescribing the wall-normal velocity component $v'(x, z, t)$ at the wall:

$$\begin{aligned} v'(x, 0, z) = & f_v(x) \cdot \sum_{k=1}^{\infty} 2 \cdot A_{(0,k)} \cdot \cos(k\gamma_0 z + \Theta_{(0,k)}) \\ & + f_w(x) \cdot \sum_{h=1}^{\infty} \sum_{k=-\infty}^{\infty} 2 \cdot A_{(h,k)} \cdot \cos(k\gamma_0 z - h\omega_0 t + \Theta_{(h,k)}), \end{aligned} \quad (2.8)$$

with frequencies $h\omega_0$, spanwise wavenumbers $k\gamma_0$, amplitudes $A_{(h,k)}$, and phases $\Theta_{(h,k)}$. (The common double-spectral notation is used where (h, k) denotes timewise and spanwise harmonics of the respective fundamental wavenumbers.) The fundamental frequency ω_0 determines a fundamental period in time denoted by $T_0 = 2\pi/\omega_0$. The functions $f_v(x)$ and $f_w(x)$, indicating vortex and wave excitation, respectively, are functions of the downstream direction and sketched in figure 2.1. As the initial condition of the perturbation simulation consists of the bare base flow only the perturbation strips are gradually ramped on during time.

Wall: The no-slip/no-penetration condition $u' = v' = w' = 0$ is imposed except within regions of perturbation strips or suction orifices. The following equations hold for the wall-vorticity vector:

$$\frac{\partial^2 \hat{\omega}'_{x,(k)}}{\partial x^2} + \frac{\partial^2 \hat{\omega}'_{x,(k)}}{\partial z^2} = \frac{\partial^2 \hat{\omega}'_{y,(k)}}{\partial x \partial y} + \frac{\partial}{\partial z} \Delta \hat{v}'_{(k)} \quad k \neq 0, \quad (2.9a)$$

$$\frac{\partial \hat{\omega}'_{x,(k)}}{\partial x} = -\frac{\partial \hat{\omega}'_{y,(k)}}{\partial y} \quad k = 0, \quad (2.9b)$$

$$\omega'_y = 0, \quad (2.9c)$$

$$\frac{\partial \omega'_z}{\partial x} = \frac{\partial \omega'_x}{\partial z} - \Delta v'. \quad (2.9d)$$

Modeled suction: Two types of modeled suction are considered in the current work, namely spanwise-slit suction and hole suction. The following wall-normal velocity components are prescribed at the wall:

$$v'(x, 0, z) = -v_{max} \cos^3\left(\frac{\pi(x - x_S)}{l_{mod}}\right), \quad (2.10)$$

$$v'(x, 0, z) = -v_{max} \cos^3\left(\frac{\pi r}{d_{mod}}\right), \quad (2.11)$$

where v_{max} is the maximum suction velocity in the slit or hole center.

As for the spanwise slit suction, x_S defines the slit center position and l_{mod} the chordwise extension of the slit. Note that the modeled suction is two-dimensional with respect to the computational coordinate system (x, y, z) .

For the hole suction, r and d_{mod} are the radius and diameter, respectively, of the suction hole with $r = \{(x - x_H)^2 + (z - z_H)^2\}^{1/2}$ and $(x_H, 0, z_H)$ defining the hole center.

Note that a modeled hole-suction velocity distribution needs three parameters to be defined: The maximum suction velocity v_{max} , the hole diameter d_{mod} , and the distribution $v(r)$. For the chosen $v(r)$, see equation (2.11), a diameter d_{mod} larger than d of an assumed Hagen-Poiseuille (suction-channel) profile is required ($d_{mod}/d = 1.51$, see section 4.1) to yield identical mass flow at the same maximum suction velocity.

Similar to the holes, a plane Poiseuille-flow profile is assumed for the slit flow and hence $l_{mod}/l = 1.57$ has to be considered to obtain identical mass flow at equal maximum suction velocity, where $l_{mod} \approx d_{mod}$ has been chosen, cf. also sections 4.1 and 5.2.

Homogeneous suction can be defined at the wall by prescribing a constant wall-normal velocity component at the wall within a certain chordwise domain l_x covering the complete spanwise domain. At the beginning and at the end of this area the velocity distribution is ramped from zero to one and vice versa using a \cos^3 -distribution.

2.1.2.3 Implementation

To obtain the solution at a new time-level, the following procedure is carried out [12]: The explicit fourth-order Runge-Kutta O4 integration scheme is used to advance the vorticity field, equations (2.5a-2.5c) in time. Hereby, the non-linear terms are computed pseudo-spectrally based on an aliasing-free fast Fourier transformation. Once the vorticity field is known, the Poisson equation (2.5f) is solved for the v -component using an implemented direct solver, followed by the solution of the vorticity vector at the wall using the wall boundary conditions (2.9). Last, the remaining two Poisson equations (2.5d) and (2.5g) for u and w are solved.

2.1.2.4 Semi-implicit time integration

The three momentum equations (2.5a-c) can be written as

$$\frac{\partial \boldsymbol{\omega}}{\partial t} = -\mathbf{N} + \frac{1}{Re} \Delta \boldsymbol{\omega} = -\mathbf{N} + \mathbf{V}_{xx} + \mathbf{V}_{yy} + \mathbf{V}_{zz}, \quad (2.12)$$

where \mathbf{N} and \mathbf{V} combine the non-linear and viscous terms, respectively.

For cases with suction above, say, $v_{max} = 10 - 15\%$, highly-resolved wall-normal grids are necessary, and the resulting numerical time-step limit is dominated by the term \mathbf{V}_{yy} comprising the second wall-normal derivative of each vorticity component. An implicit time-integration scheme for this term is implemented according to the trapezoidal rule. Since this yields $O(2)$ -accuracy, a modified Heun method being second-order accurate as well is used for the remaining explicit time integration for full consistency. A second corrector step is added to secure A-stability. The scheme reads (see also Friederich & Kloker [20]):

$$\boldsymbol{\omega}^{(l+1)*} = \boldsymbol{\omega}^{(l)} + \Delta t \left\{ \mathbf{R}^{(l)} + \frac{1}{2} \mathbf{V}_{yy}^{(l)} + \frac{1}{2} \mathbf{V}_{yy}^{(l+1)*} \right\}, \quad (2.13a)$$

$$\boldsymbol{\omega}^{(l+1)**} = \boldsymbol{\omega}^{(l)} + \frac{\Delta t}{2} \left\{ \mathbf{R}^{(l)} + \mathbf{R}^{(l+1)*} + \mathbf{V}_{yy}^{(l)} + \mathbf{V}_{yy}^{(l+1)**} \right\}, \quad (2.13b)$$

$$\boldsymbol{\omega}^{(l+1)} = \boldsymbol{\omega}^{(l)} + \frac{\Delta t}{2} \left\{ \mathbf{R}^{(l)} + \mathbf{R}^{(l+1)**} + \mathbf{V}_{yy}^{(l)} + \mathbf{V}_{yy}^{(l+1)} \right\}, \quad (2.13c)$$

where (l) is the current time level and $\mathbf{R} = -\mathbf{N} + \mathbf{V}_{xx} + \mathbf{V}_{zz}$. Each of these equations has the form

$$\left(1 - \frac{\Delta t}{2Re} \frac{\partial^2}{\partial y^2} \right) \boldsymbol{\omega}^{(l+1)} = \tilde{\mathbf{R}}, \quad (2.14)$$

where $\tilde{\mathbf{R}}$ includes all remaining explicit parts of the right hand sides of (2.13).

At the wall, the equation system (2.9) is applied for obtaining the new wall-vorticity values. Equation (2.9a) depends on the v -velocity component of the flow field at the new time level which in turn depends on the new wall-vorticity values. Thus, an iteration procedure has to be carried out for each substep (2.13a) - (2.13c), monitoring wall vorticity and starting with the wall-vorticity values of the old time level:

$$\left(1 - \frac{\Delta t}{2Re} \frac{\partial^2}{\partial y^2} \right) \boldsymbol{\omega}^{(l+1)^{(i+1)}} = \tilde{\mathbf{R}}, \quad (2.15)$$

with (i) being the iteration level. For equation (2.13a) for example, within each iteration step the vorticity components for $y > 0$ are computed, then the v -poisson equation and finally the wall-vorticity equations are solved. The updated wall values serve as new boundary condition for the next iteration step. Note that the right hand side $\tilde{\mathbf{R}}$ remains constant during the iteration. (5,4,3) iteration cycles have shown to be sufficient for equations (2.13a, 2.13b, 2.13c).

The convective terms in y -direction still impose a small time step translating into an insufficient damping of high-wavenumber modes devised by the alternating forward-/backward-biased differencing of the convective terms in chordwise direction [38]. Therefore a compact spatial filter [9] is activated in chordwise direction x for all simulations with suction and the fine wall-normal grid.

2.2 Compressible numerical method

The procedure of solving the unsteady compressible Navier-Stokes equations is also split into two consecutive parts: A steady, spanwise invariant base flow is computed first and used as an initial solution for the second step, the unsteady simulation employing the full variables and including controlled perturbations. The IAG code PROFKOM, that has until now been typically used for creating compressible base flows, solves the compressible boundary-layer equations and is thus capable of computing two-dimensional flows only, i.e. no spanwise velocity component is considered. For the current work a computation scheme for obtaining a spanwise invariant three-dimensional base flow, similar to the incompressible one, is necessary and described in section 2.2.1. Furthermore, the numerical method for solving the unsteady problem has until now been applied for symmetrical two-dimensional base flows and without streamwise pressure gradients only. Modified freestream boundary conditions allow now for simulating 3-d boundary layers and are presented in section 2.2.2.1, where the compressible Navier-Stokes solver is introduced.

2.2.1 Computation of the steady spanwise-invariant base flow

The compressible base flow is obtained in two steps: First, a solution of the three-dimensional compressible parabolized Navier-Stokes (PNS) equations with constant spanwise freestream velocity and prescribed streamwise pressure gradient is computed using an extension of the PNS code originally developed by Schmidt [73]. This PNS solution serves as an initial and as boundary condition for the second step, the steady full Navier-Stokes computation, cf. figure 2.2. The goal is to create a base flow matching as closely as possible the incompressible one.

This procedure is necessary for three reasons: Appropriate boundary conditions of the final DNS domain at the inflow and the upper boundary are required, preventing significant streamwise transients within the domain. Also, the integration domain of the (numerically cheap) PNS solution is huge in order to prevent influences of the ad-hoc chosen inflow boundary onto the final DNS domain. Last, matching the flow to the incompressible case required many iterations suggesting a fast numerical procedure.

As for the PNS, the dimensionless freestream-velocity distribution $u_e(x)$ is chosen as design variable and matched to the incompressible case. Alternatively, the pressure distribution could be matched, but matching $u_e(x)$ eases comparison with our incompressible vorticity-based code. The beginning of the PNS integration domain is close to the leading edge, far upstream of the

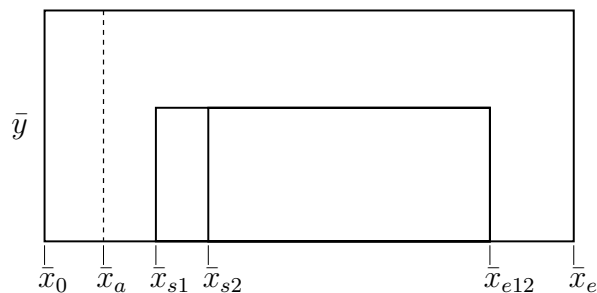


Figure 2.2: Sketch of the integration-domain extensions for compressible base-flow computations. Not to scale. PNS domain from \bar{x}_0 to \bar{x}_e . DNS domains from \bar{x}_{s1} , \bar{x}_{s2} to \bar{x}_{e12} . For details on \bar{x}_a see section 3.2.

DNS domain start in order to keep influences from the inflow at a minimum where Blasius profiles are prescribed as an inflow boundary condition. At the upper boundary the streamwise pressure gradient has to be specified. The compressible Bernoulli equation along a streamline (subscript s) is considered:

$$\int \frac{d\bar{p}}{\bar{\rho}} + \frac{\bar{q}^2}{2} = \text{const.} \quad (2.16)$$

When substituting $\bar{\rho}$ by \bar{p} using the isentropic relations, equation (2.16) can be written as $\partial\bar{p}/\partial\bar{s} = f(\bar{u}, \partial\bar{u}/\partial\bar{s})$ which is known from the incompressible base flow. Dirichlet boundary conditions can then be prescribed for $\bar{T}_e(\bar{x})$ and $\bar{\rho}_e(\bar{x})$ using the isentropic relations. The non-dimensional $u_e(x)$ -distribution can be matched perfectly to the incompressible one by this procedure.

The second step, the steady Navier-Stokes solution, is carried out in two parts to obtain the final base flow: First, a preliminary DNS domain is used employing PNS velocity profiles at the inflow (\bar{x}_{s1}), see figure 2.2. Then the final DNS domain 2 is considered where profiles from the first DNS solution are used for the inflow boundary condition at \bar{x}_{s2} . Both domains end at \bar{x}_{e12} . For both DNS domains PNS values are prescribed at the freestream boundary. At the outflow the space operator from the last but one grid point is applied.

2.2.2 Computation of the perturbed flow

The three-dimensional unsteady compressible Navier-Stokes equations are solved together with the continuity and energy equation in conservative formulation, where $\mathbf{Q} = (\rho, \rho u, \rho v, \rho w, E)^T$ represents the solution vector consisting of density, mass fluxes and total energy per volume. The equations may be found in appendix C. In contrast to the incompressible code the computation happens here mainly in physical space; the Fourier space is exploited for calculating spanwise derivatives only. Also unlike the incompressible case, the unsteady compressible equations are solved in total variables. The numerical method is extensively described in [5, 45, 6].

The integration domain, the computational coordinate system and the non-dimensionalization are chosen and defined similarly to the incompressible case as described in section 2.1. The reference density $\bar{\rho}_\infty$, the reference temperature \bar{T}_∞ , and the speed of sound $\bar{a}_\infty = \sqrt{\kappa R \bar{T}_\infty}$ are additionally used for

normalization (see sections 3.2 and 3.3 for the actual reference values):

$$\begin{aligned} \rho &= \frac{\bar{\rho}}{\bar{\rho}_\infty}, & T &= \frac{\bar{T}}{\bar{T}_\infty}, & p &= \frac{\bar{p}}{\bar{\rho}_\infty \bar{u}_\infty^2}, \\ Ma_\infty &= \frac{\bar{u}_\infty}{\bar{a}_\infty}, & Pr &= \frac{\bar{c}_p \bar{\mu}_\infty}{\theta_\infty}, & Re &= \frac{\bar{\rho}_\infty \bar{u}_\infty \bar{L}}{\bar{\mu}_\infty}. \end{aligned} \quad (2.17)$$

The specific heats c_p and c_v as well as the Prandtl number are assumed to be constant whereas the temperature-viscosity dependence is modeled by Sutherland's law.

Sixth-order compact finite differences on an orthogonal grid (stretched in wall-normal direction) are used to discretize the streamwise and wall-normal direction, respectively. Stretched grids are handled by grid transformation. For the spanwise direction a Fourier-spectral ansatz is implemented to compute the spanwise derivatives following the Fourier decomposition (2.4). The explicit four-step fourth-order Runge-Kutta scheme serves as time integrator.

2.2.2.1 Boundary conditions

At the subsonic inflow all base-flow variables are prescribed and upstream-traveling acoustic waves are allowed to leave the integration domain using a disturbance transformation to characteristic variables. The no-slip isothermal wall with wall-pressure condition $\partial p / \partial y|_{wall} = 0$ includes several disturbance strips where the wall-normal mass flux ρv -component is prescribed to excite steady and unsteady disturbances. At the outflow, a buffer domain is employed that ramps all conservative variables to their respective base-flow values. At the freestream, the base-flow values are kept for w , T , and ρ , suppressing all disturbances. In addition, $\partial u / \partial y|_e = 0$ allows u_e to adequately adapt, and $\partial v / \partial y|_e = -(\partial(\rho_e u_e) / \partial x) / \rho_e$ is exploited to obtain v_e , assuming $\partial \rho / \partial y|_e = 0$.

For cases with modeled suction, equation (2.11) from the incompressible code is considered. The wall-normal mass flux ρv is prescribed here instead of v :

$$\rho v'(x, 0, z) = -\rho v_{max} \cos^3\left(\frac{\pi r}{d_{mod}}\right), \quad (2.18)$$

where ρv_{max} is the maximum suction mass flux in the hole center.

2.2.2.2 Module for simulated suction

A code extension developed by Kunze [44] allows for the attachment of a cylindrical channel-flow domain to the rectangular flat-plate domain. It was applied to study the influence of cold-gas blowing through holes on film cooling in super- and hypersonic boundary layers.

In the current work the code was adapted to simulate suction through the channel domain in order to compare the effects of modeled hole suction and the attached simulated suction channel. Figure 2.3 shows the integration domains and the definition of the cylindrical coordinate system. The original channel domain employed an equidistant grid for r and h . The circumferential direction was resolved by an equidistant grid as well, featuring spectral derivatives similar to the spanwise direction of the rectangular integration domain. The implementation of grid stretching for the h -coordinate resulted in a considerable speed-up during the current investigations. The center line of

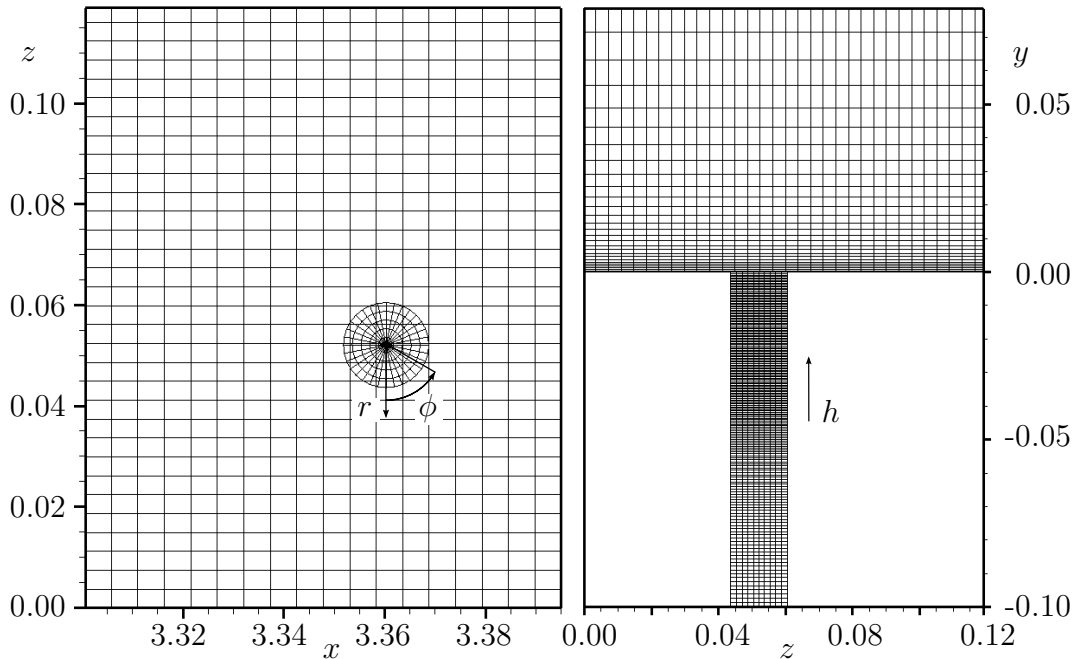


Figure 2.3: Sketch of computational grids in the vicinity of the coupling between main integration domain and suction-channel domain. Every 4th grid line of case CHAN (cf. section 4.3) is shown. The origin of the cylindrical coordinate system (h, r, ϕ) is at the lower end of the suction channel.

the channel forms a singularity at $r = 0$. By choosing an appropriate numerical grid the center line is not simulated but the neighboring grid points are located at $\pm\Delta r/2$. Thus, the stencil of finite differences can be easily set up across the channel center. An implemented mode reduction for the circumferential coordinate at small r handles prohibitive grid steps monitoring $r\Delta\phi$. The boundary conditions include an isothermal wall with no-slip condition and periodic boundary conditions in circumferential direction. The inflow (when the channel is used for suction) represents the coupling between the Cartesian and cylindrical domains where interpolation routines are implemented featuring overlapping finite differences. The outflow is defined prescribing pressure, temperature, and boundary values for all three velocity components extrapolated from the channel flow above. By adapting the pressure at the outflow, the suction mass flux can be controlled. The flow is initialized with a constant pressure gradient Hagen-Poiseuille velocity profile according to pipe-flow theory. Spatial filtering is inevitable to obtain stable simulations with eventually smooth flow. The filter is applied for $y \geq 0.0$ and for $y < 0.0$, $0.0 \leq r < d$.

2.3 Verification

Publications of detailed data of non-weak, localized suction in three-dimensional boundary layers are not known. The incompressible numerical method has been well tested and validated for crossflow transition scenarios [79, 9] as well as for moderate suction in two- and three-dimensional boundary layers [56]. As verification for strong suction and the semi-implicit time-integration scheme, one of the current cases is simulated also with the compressible code that is not based on vorticity.

The chordwise Mach number for the “Prinzipexperiment” is approximately 0.05. Since the numerical time-step limit of the compressible method is very prohibitive at small freestream Mach numbers, a similar boundary-layer flow at $Ma_\infty = 0.20$ is chosen for the verification simulation. For details of the numerical setup see appendix A and also Friederich & Kloker [20].

The wall-normal resolution can be coarser for the compressible case: the step size $\Delta y_{wall} = 2.3 \cdot 10^{-4}$ is 35 times larger, and thus only 95 grid points

are needed compared to 225 for the incompressible case. The wall-normal grid stretching yields $\Delta y_e/\Delta y_{wall} = 12$, versus 120 for the incompressible case. The resolutions in downstream and spanwise direction ($\Delta x = 1.309 \cdot 10^{-3}$, $K = 10$) are identical. The resolution of the relevant shear layers at the edge of the boundary layer is still appropriate, cf. table A.1 in appendix A.

(Still, to obtain a solution at a given physical time after disturbance activation, the incompressible code runs more than 14 times faster when a Mach number of 0.2 is chosen for the compressible case, the latter having an about seven times smaller time step, cf. also appendix A.)

A visualization of vortical structures [31] and velocity crosscuts for the case with modeled suction is given in figure 2.4 comparing the incompressible and compressible results. The rotated reference system (cf. appendix D) is used for visualization with $x_0 = 3.20$, $z_0 = -0.03$, $\phi_r = 45.0^\circ$. The inset shows a top view where the suction holes are marked by black circles. Again, almost identical results can be observed proofing the correctness of the results. A preceding study of the verification can be found in [24].

Figure 2.5 shows the downstream modal development of the streamline-oriented disturbance velocity component $\tilde{u}'_s = u'_s/u_{b,s,e}$ for a reference case without suction and a case with modeled hole suction. These are the cases REF and 1-H with $K = 10$, see tables A.1 and 5.1 discussed in more detail later. In all cases, the steady CFV mode with $\gamma = \gamma_0 = 52.4$ has been excited at $x = 2.2$ as primary disturbance and a packet of controlled unsteady disturbances at $x = 3.0$ has been introduced to easily check for secondary instability. The modeled hole-suction distributions as well as the disturbance-strip setups are virtually identical in all cases since prescribing ρv in the compressible case results in negligible v -deviations at the chosen Mach number. The match of the results of the two codes proofs the correctness of the results at the prescribed boundary conditions and used discretization. Moreover, careful grid studies using higher resolutions, especially $K = 15$ and 21, clearly show that the results in figure 2.5 are converged, see also appendix B.

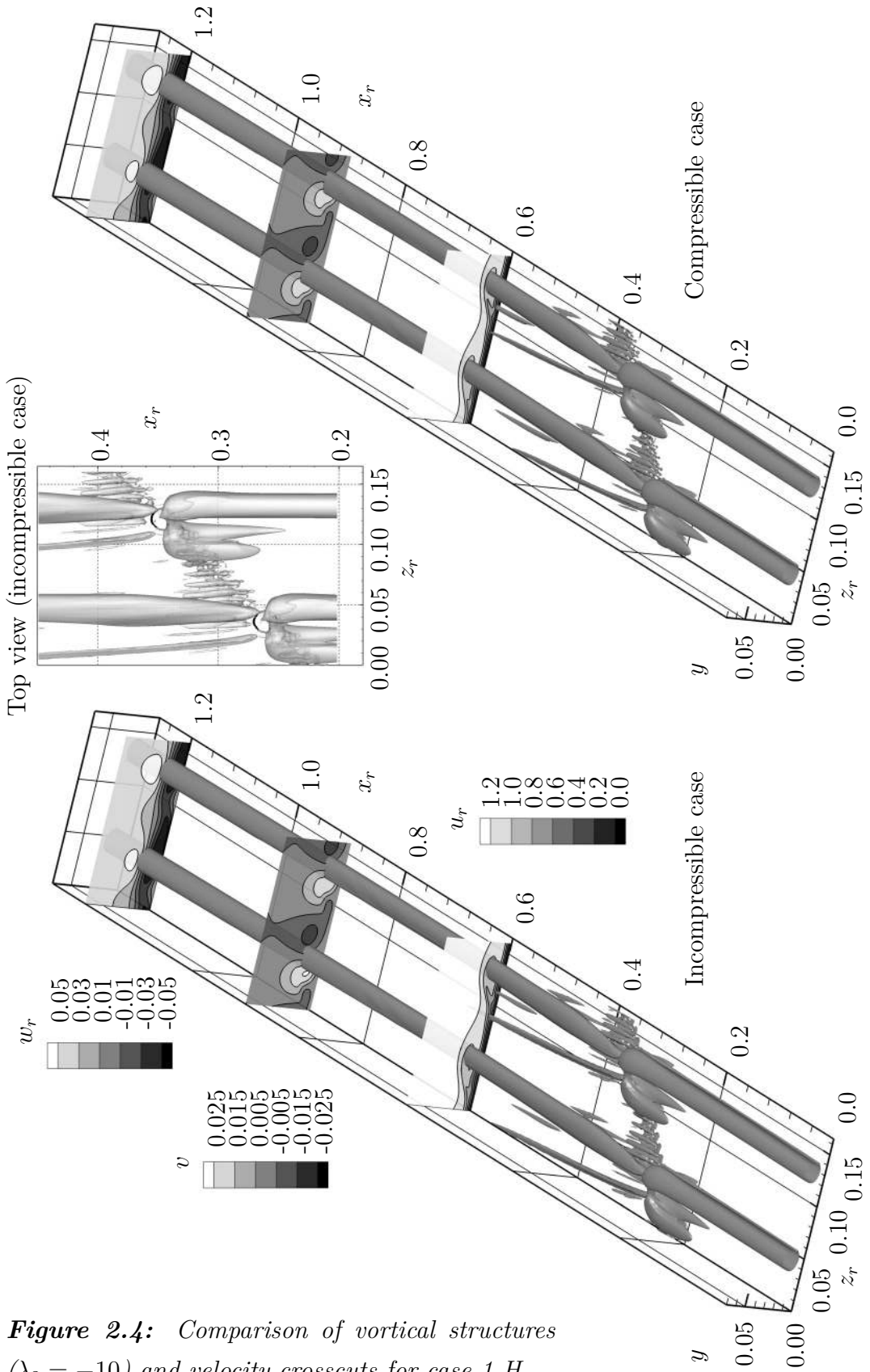


Figure 2.4: Comparison of vortical structures ($\lambda_2 = -10$) and velocity crosscuts for case 1-H.

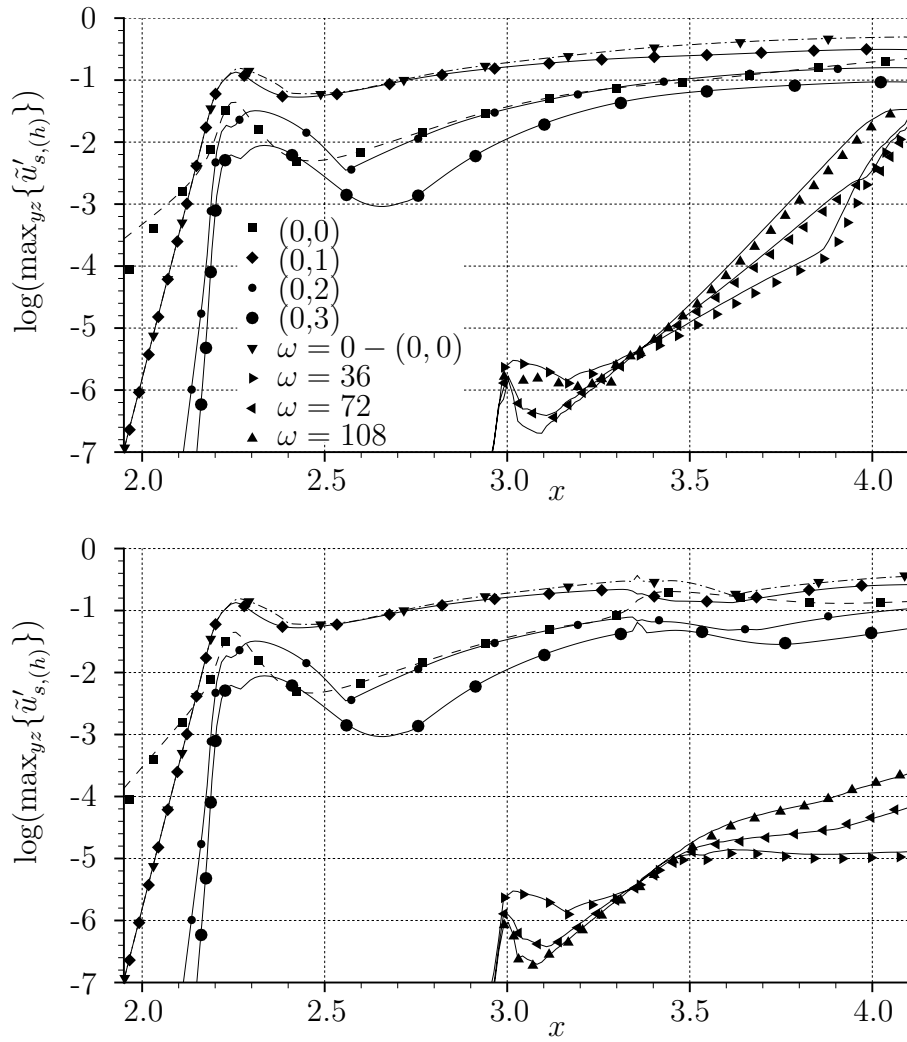


Figure 2.5: Downstream development of selected modal \tilde{u}'_s -amplitudes obtained from the incompressible code (lines) and compressible code (symbols). Shown are a reference case without suction (top) and a case with a single suction hole (bottom).

3 Base flows

The 3-d boundary-layer flow that has been experimentally investigated by Bippes and co-workers in the “Prinzipexperiment” (DLR Göttingen, see, e.g., the review article by Bippes [8]), is subject of investigation in the present work. The experimental setup consists of a flat plate with a displacement body above to generate a favorable streamwise pressure gradient. Streamline-shaped lateral plates are used to approximate an infinite wing-span. The chord length of the flat plate is $\bar{c} = 0.5m$. A nearly constant favorable pressure gradient imposed corresponds to a Falkner-Skan-Cooke (FSC) flow with a Hartree parameter $\beta_h = 2/3$, but the flow resulting is only nearly a FSC flow [9, 12].

Three base flows are employed in the current work: First (3.1), the proven incompressible 3-d base flow computed by Bonfigli [9] is chosen for various (modeled-) suction scenarios presented in chapter 5.

Second (3.2), an akin flow at $Ma(x_0) = 0.7$ is computed for comparing results between modeled and simulated pinpoint suction discussed in section 4.3. Here, the incompressible streamwise freestream-velocity distribution is chosen as design variable and matched. The DNS are performed for a Mach number $Ma=0.7$ to (i) exploit the improved performance of the compressible code compared to $Ma=0.05$ for the “Prinzipexperiment”, and (ii) to check the influence of a Mach number relevant to airliner flight.

Third (3.3), a compressible Blasius flow at $Ma_\infty = 0.5$ is set up for a fundamental comparison of modeled and simulated suction unaffected by crossflow and pressure gradient; the results are discussed in section 4.2.

The most relevant characteristics of the incompressible and compressible 3-d base flows are discussed in section 3.4.

Note that the 3-d base flow used for verification in section 2.3 at $Ma_\infty = 0.2$ is not further discussed here.

3.1 Incompressible 3-d boundary layer

The incompressible base flow was computed by Bonfigli [9] who also developed the numerical procedure described in section 2.1.1. The goal was to match the experimental flow of the DLR ‘‘Prinzipexperiment’’ as closely as possible. An effective experimental sweep angle of $\phi_{exp} = 42.5^\circ$ and a freestream velocity of $\bar{Q}_\infty = 19.0m/s$ ($\bar{U}_\infty = 14.0m/s$) as well as the experimental, nearly constant negative streamwise pressure gradient define the most important parameters for the computation. The streamwise velocity distribution is used as reference for the compressible base flow. Velocity profiles as well as boundary-layer parameters are included in the respective figures in section 3.4 and compared to results from the compressible 3-d case at $Ma=0.7$.

3.2 Compressible 3-d boundary layer at $Ma=0.7$

The time-step limit and therefore the computational performance of the compressible code depends directly on the freestream Mach number for low Mach numbers.

As for the verification simulation a fairly low Mach number of $Ma_\infty = 0.2$ had been chosen (cf. section 2.3) to meet both computational feasibility and ‘‘incompressible’’ flow behavior which was indispensable for a quantitative comparison of the incompressible and compressible numerical method.

The investigation purpose here, however, is different. A comparison of modeled suction and suction comprising the suction channel is desired. The integration domain covers the incompressible-case Re_{δ_1} range to ensure a related flow field where the dimensionless freestream velocity components u_e and w_e are chosen as design variables and matched to the incompressible distribution.

Following the computational procedure described in section 2.2.1, the variables for the upstream boundary of the PNS domain at $\bar{x}_0 = 0.0010m$ depend on the initial choice of the Mach number based on the oncoming flow $\bar{q}_e(\bar{x}_0) = \{\bar{w}_e(\bar{x}_0)^2 + \bar{u}_e(\bar{x}_0)^2\}^{1/2}$, set to $Ma_q(\bar{x}_0) = \bar{q}_e(\bar{x}_0)/\bar{a}(\bar{x}_0) = 0.70$. The

density is chosen to be $\bar{\rho}(\bar{x}_0) = 1.225 \text{ kg/m}^3$. To match the kinematic viscosity of the incompressible case ($\bar{\nu} = 1.52 \cdot 10^{-5} \text{ m}^2/\text{s}$) the temperature is set to $\bar{T}_e(\bar{x}_0) = \bar{T}_{wall} = 303.4 \text{ K}$. Therewith, $\bar{q}_e(\bar{x}_0) = 244.43 \text{ m/s}$ is found, and by varying the angle of the oncoming flow such that the incompressible streamwise velocity distribution $u_e(x)$ is met, yielding $\phi(\bar{x}_0) = 72.58^\circ$, the spanwise and streamwise velocity components are $\bar{w}_e(\bar{x}_0) = \bar{w}_e = 233.22 \text{ m/s}$ and $\bar{u}_e(\bar{x}_0) = 73.18 \text{ m/s}$, respectively.

Prescribing $\bar{w}_e = \text{const.}$, $\bar{T}_e(\bar{x})$, $\bar{\rho}_e(\bar{x})$, and $\partial\bar{p}/\partial\bar{x}(\bar{x})$, the desired non-dimensional $u_e(x)$ distribution is matched. For simplicity, Blasius inflow profiles are given. By this procedure, however, the resulting crossflow component $w_s(y)$ did not match the distribution obtained from the DLR experiment and the incompressible base flow. Hence, during chordwise integration, the solution is adapted once at $\bar{x}_a = 0.0047 \text{ m}$ (cf. figure 2.2). Enlarging $w_s(x_a, y)$ gives modified u - and w - profiles that match the incompressible crossflow that in turn had also been matched [9] to the well-documented experimental development.

The domain extensions introduced in figure 2.2 are $\bar{x}_{s1} = 0.0055 \text{ m}$, $\bar{x}_{s2} = 0.0062 \text{ m}$, $\bar{x}_{e12} = 0.0304 \text{ m}$. Note that the DNS domain of the final simulation with disturbances starts only at $\bar{x} = 0.0104 \text{ m}$.

Similarly to the incompressible case the reference velocity is chosen at the chordwise position with a local flow angle of $\phi_e = \phi_\infty = 42.5^\circ$ and yields $\bar{U}_\infty = \bar{w}_{e,0} / \tan \phi_\infty = 254.51 \text{ ms}^{-1}$. Defining $Re = 92000$ and using $\bar{\nu} = 1.52 \cdot 10^{-5} \text{ m}^2/\text{s}$ from the incompressible case the reference length yields $\bar{L} = 5.49 \cdot 10^{-3} \text{ m}$. Additionally, $\bar{T}_\infty = \bar{T}(\bar{x}_0)$ and $\bar{\rho}_\infty = \bar{\rho}(\bar{x}_0)$ are used for normalization as already mentioned in section 2.2.2. Properties of the compressible 3-d base flow are provided in section 3.4.

3.3 Compressible Blasius boundary layer at $Ma=0.5$

The compressible boundary-layer equations are solved to obtain a Blasius similarity solution at $Ma_\infty = \bar{U}_\infty / \bar{a}_\infty = 0.5$. The Reynolds number is 100,000 and the reference values include the freestream velocity $\bar{U}_\infty = 173.63 \text{ m/s}$,

the reference length $\bar{L} = 9.1575 \cdot 10^{-3}m$, the temperature $\bar{T}_\infty = 300K$, and the density $\rho_\infty = 1.161kg/m^2$. The considered streamwise domain covers the Reynolds number range $1880 < Re_{\delta_1} < 2000$ resulting in the dimensionless streamwise coordinate $11.7 < x < 13.1$.

3.4 Properties of the 3-d base flows

Velocity profiles from the Ma=0.7 steady compressible 3-d Navier-Stokes base flow are compared with the corresponding incompressible ones in figure 3.1 for two downstream positions. The slightly fuller u - and w -profiles of the incompressible flow show that, owing to the decreasing density during acceleration, the boundary layer becomes thicker for the compressible case. This finding is in accordance with less negative v -profiles. Figure 3.2 compares velocity profiles in the streamline-oriented coordinate system (for a definition of the corresponding coordinate system see appendix D) and provides temperature and density profiles for the Ma=0.7 case. The u_s -profile behavior is similar to u before. The typically shaped crossflow profiles with maxima at approximately $\delta/4$ are found for w_s , with the compressible maxima being slightly larger than the incompressible ones. This can be explained by the equilibrium of forces normal to a curved, steady streamline: $\partial p/\partial n = \rho v^2/r$. Since for the Ma=0.7 case the density decreases in the boundary layer and the pressure gradient is approximately constant, the (crossflow) velocity component must increase.

A comparison of the boundary-layer parameters is provided in figures 3.3 and 3.4. Values with subscript s are evaluated using the streamline-oriented velocity component u_s . For the calculation of the displacement and momentum thickness a pseudo-velocity distribution $u_p = \int_0^{y_e} \omega_z dy$ is used for both cases to suppress influences from slightly non-constant u -velocity profiles outside the boundary layer. Thus, the wall-normal density variation is neglected to compare velocity profiles only.

The flow is accelerated in chordwise direction throughout the complete integration domain, and due to the sweep angle the wall-normal maximum of the crossflow velocity component w_s increases as well as already observed before. The shape factor H_{12} is computed from the displacement thickness δ_1 and the

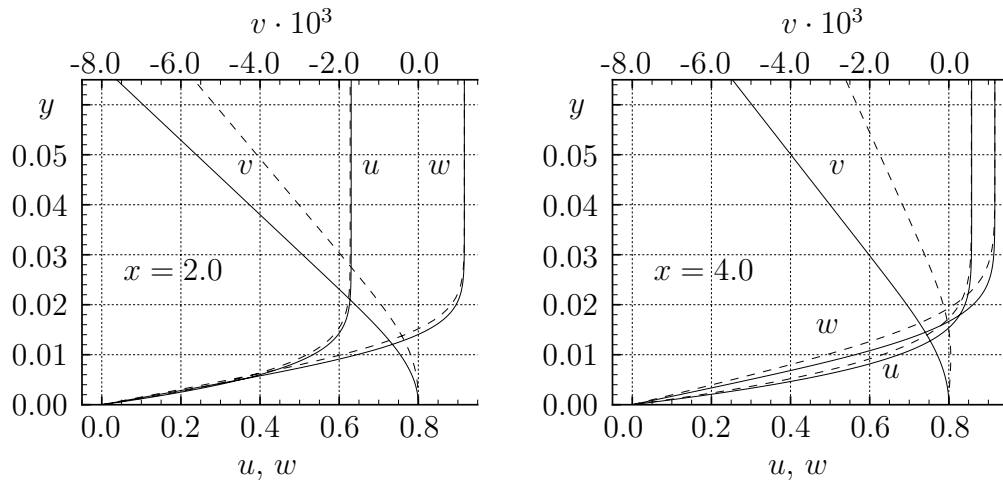


Figure 3.1: Velocity profiles of the incompressible (solid lines) and compressible (dashed lines) base flow at two streamwise locations.

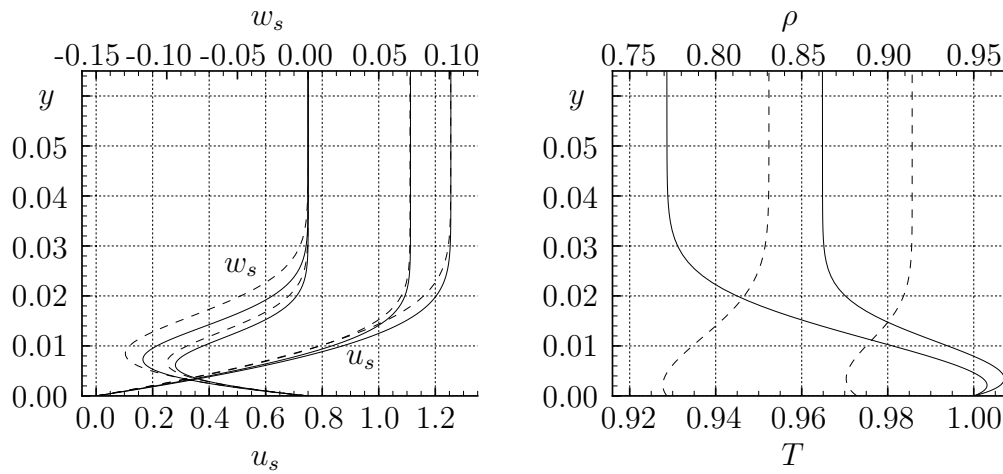


Figure 3.2: Left: Streamline-oriented velocity profiles u_s and crossflow-velocity profiles w_s of the incompressible (solid lines) and compressible (dashed lines) base flow at $x = 2.0$ and $x = 4.0$ (the profile maxima increase with increasing x). Right: Profiles for temperature T (solid lines) and density ρ (dashed lines) of the compressible base flow at $x = 2.0$ and $x = 4.0$ (freestream values decrease with increasing x).

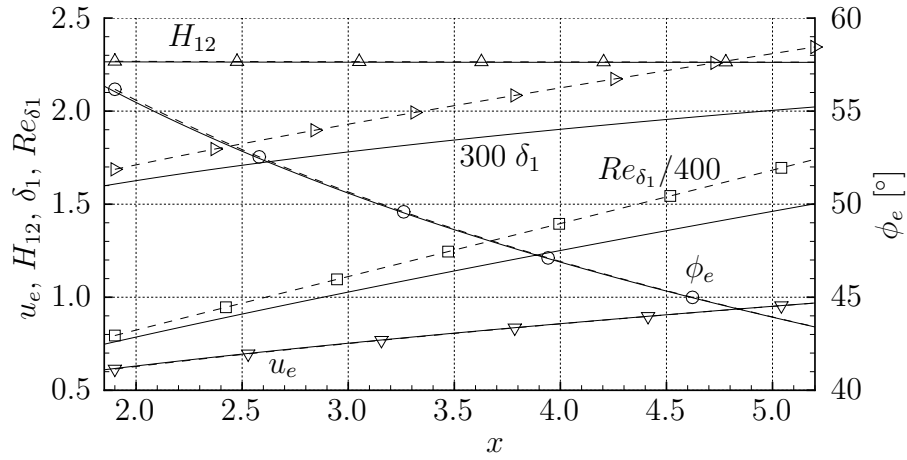


Figure 3.3: Boundary-layer parameters for incompressible base flow (solid lines) and $Ma=0.7$ base flow (dashed lines with symbols) versus chordwise coordinate x : chordwise edge velocity u_e , shape parameter H_{12} , displacement thickness δ_1 , local Reynolds number Re_{δ_1} , and local sweep angle ϕ_e .

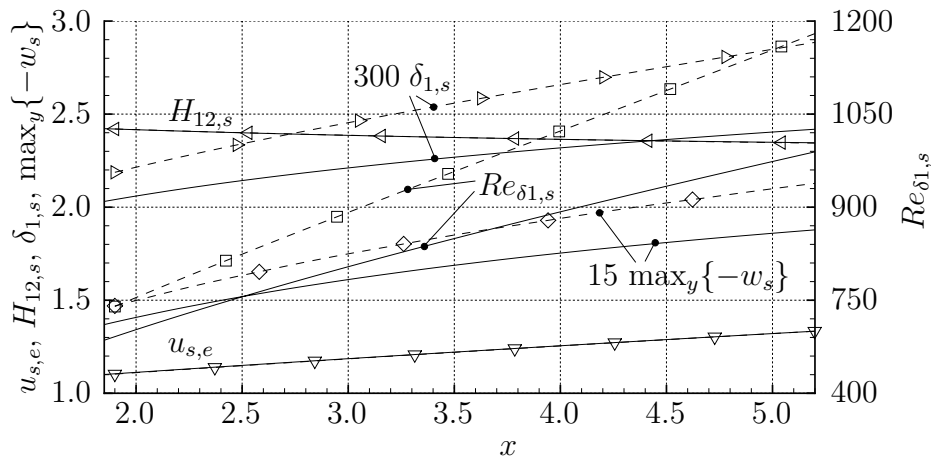


Figure 3.4: As figure 3.3: streamline-oriented edge velocity $u_{s,e}$, shape parameter $H_{12,s}$, displacement thickness $\delta_{1,s}$, local Reynolds number $Re_{\delta_{1,s}}$ and maximal crossflow velocity $\max_y\{-w_s\}$.

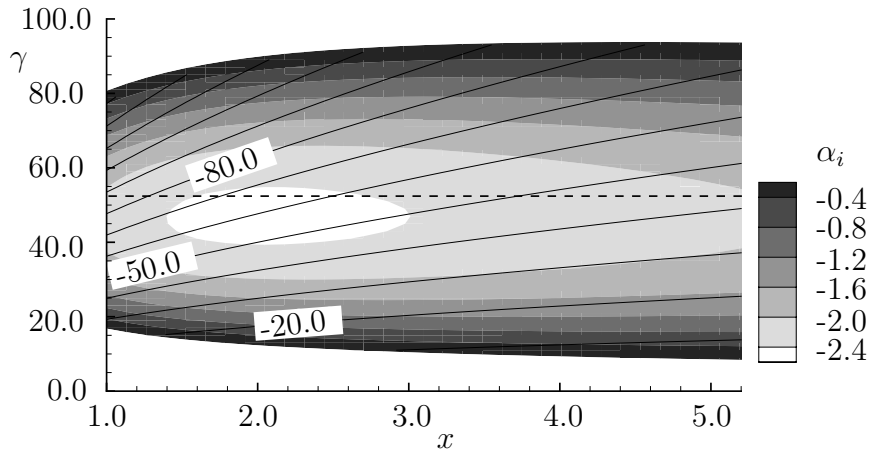


Figure 3.5: Amplification rates α_i (shaded) and streamwise wave numbers α_r (lines) of unstable steady crossflow modes as functions of streamwise coordinate x and spanwise wavenumber γ obtained from spatial incompressible LST. The dashed line marks the investigated fundamental mode $\gamma_0 = 52.4$.

momentum thickness δ_2 and yields approximately 2.26, slightly decreasing.

The difference between compressible and incompressible computations becomes obvious in the boundary-layer-thickness evaluations and the maximal crossflow. However, the shape parameters H_{12} and $H_{12,s}$ are identical indicating similar profiles. The already observed thicker boundary layer and larger maximal crossflow component for the $\text{Ma}=0.7$ case can also be found in the respective downstream development.

Results from an analysis of the incompressible base flow according to incompressible linear stability theory (LST)¹ are provided in figure 3.5 for the steady mode $\omega = 0.0$. A band of unstable spanwise modes is found indicating crossflow instability. Although higher amplification rates can be found for unsteady, traveling crossflow modes (not shown) investigations have shown that under free-flight conditions typically the steady ones prevail due to their higher receptivity [51]. Thus, only steady crossflow modes are investigated in the current work.

Owing to previous numerical studies the unstable crossflow mode with $\gamma = 52.4$ is subject of investigation for all simulations. It represents one of the most amplified steady modes that are expected to develop in a natural scenario.

¹The numerical method was programmed by M. Zengl, IAG, Universität Stuttgart

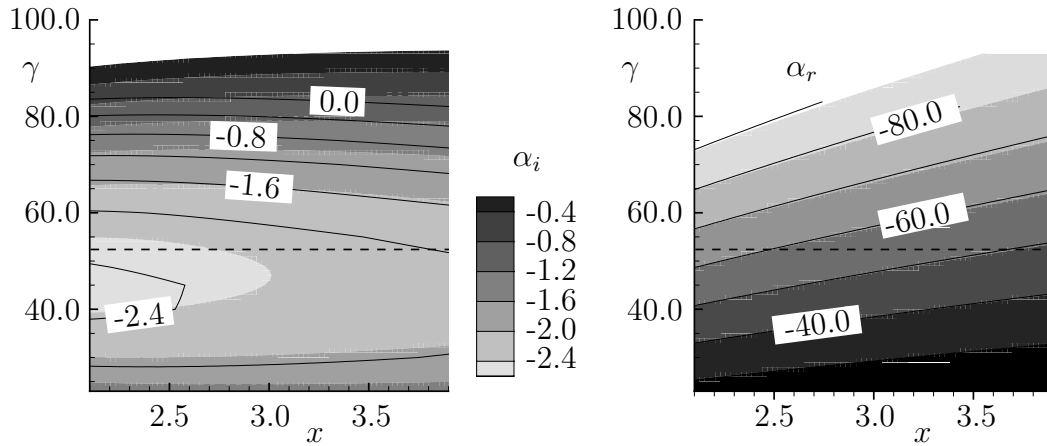


Figure 3.6: Comparison of amplification rates α_i (left) and streamwise wave numbers α_r (right, α_r -values for $\alpha_i > 0$ cut off) as functions of streamwise coordinate x and spanwise wavenumber γ for the incompressible base flow (shaded, spatial incompressible LST) and the $Ma=0.7$ base flow (lines, spatial compressible LST). The dashed line marks the investigated fundamental mode $\gamma_0 = 52.4$.

Figure 3.6 provides a comparison of results from a compressible LST evaluation² of the $Ma=0.7$ base flow (solid lines) with the incompressible LST results (shaded) of the incompressible base flow. The corresponding streamwise wavenumbers α_r of the unstable steady crossflow modes are almost identical, the amplification rates α_i however show some deviations. For the $Ma=0.7$ case the maximum is shifted towards lower spanwise wave numbers and also the absolute value decays slightly (at $x = 2.2$ and $\gamma = 52.4$: $\alpha_{i,incomp} = -2.44$, $\alpha_{i,comp} = -2.31$). For $\gamma \leq 20$ the solution did not converge, however this is outside the region of interest.

²Code included in the PNS solver by O. Schmidt [73]

4 Comparison of modeled and simulated suction

The effects of hole suction on two- and three-dimensional boundary layers are investigated in this chapter with special focus on the comparison of modeled and simulated suction. For modeled suction, the suction-velocity distribution is prescribed at the wall whereas for simulated suction the flow below the suction orifice in the suction channel is simulated.

In the three-dimensional boundary layer, the development of a controlled excited crossflow vortex (CFV) eventually inducing secondary instability is controlled by a single suction hole. The focus of this chapter is on the comparison of the effects on the flow through modeled and simulated suction rather than on the physical effects of transition control by means of pinpoint suction. This is elaborated in chapter 5.

The channel-flow module is integrated in the compressible DNS code introduced in section 2.2. Originally developed for cold-gas blowing through holes [45] the module has been adapted to simulate a suction channel (cf. section 2.2.2.2); see also the tentative study [22]. Due to the extensive computational demands of the simulation with channel, the increasing performance of the compressible code with increasing Mach number is exploited, and hence the comparisons are carried out at the subsonic Mach numbers $Ma=0.5$ and $Ma=0.7$.

First, an overview of modeled and simulation suction setups is given in section 4.1. Then, results from modeled and simulated hole suction in a Blasius boundary-layer flow at $Ma_\infty = 0.5$ are compared in section 4.2 to explicate the influences of bare hole suction in the absence of pressure gradient and crossflow.

The comparison for a three-dimensional boundary layer provided in section 4.3 is carried out in the $Ma=0.7$ 3-d base flow where results for transition delay by modeled and simulated pinpoint suction are discussed.

4.1 Aspects of modeled and simulated suction setups

For a useful comparison it has turned out that the sucked mass fluxes in the modeled case (MOD) and simulated case with suction channel (CHAN) should be identical; see appendix E for a study where the hole diameter and maximum suction velocity are varied. The derivation of the corresponding parameters yielding equal mass fluxes is described in the following.

The modeled suction-velocity distribution (see equation 2.18) is defined according to a \cos^3 -profile. As for the theoretical channel flow, a Hagen-Poiseuille profile is considered. (Of course, the channel-velocity distribution differs from a Hagen-Poiseuille profile in the vicinity of the wall orifice, however, the overall mass flux is not affected due to mass continuity.)

The sucked mass flux of the channel simulation can be obtained by integrating the actual wall-normal mass flux $\dot{m} = \int (\rho v) r dr d\phi$ in the channel. Considering the theoretical mass fluxes for both cases

$$\dot{m}_{CHAN} = |(\rho v)|_{max} \frac{\pi}{8} d_{CHAN}^2, \quad |\rho v|_{mean} = 0.5 |\rho v|_{max} \quad (4.1)$$

$$\dot{m}_{MOD} = |(\rho v)|_{max} \frac{2(3\pi - 7)}{9\pi} d_{MOD}^2, \quad |\rho v|_{mean} \approx 0.2184 |\rho v|_{max} \quad (4.2)$$

at equal $|(\rho v)|_{max}$ and assuming constant density across the channel diameter, the diameter ratio results in

$$d_{MOD}/d_{CHAN} = 1.51313. \quad (4.3)$$

The hole-diameter of the modeled suction is larger due to the smoother shape of the \cos^3 -profile compared to the second order polynomial. Applying equation (4.3), the modeled case can be set up with equal sucked mass flux by choosing d_{MOD} and $|(\rho v)|_{max}$, once the values from the channel simulation are known.

For the sake of completeness, the procedure for slit suction (not part of this chapter, but applied in chapter 5) shall be mentioned here briefly: For the modeled case the two-dimensional \cos^3 -velocity distribution (see equation (2.10) for the incompressible case) is considered and compared to a plane Poiseuille-flow profile. The mass fluxes are

$$\dot{m}_{CHAN,2D} = |(\rho v)|_{max} \frac{4}{3\pi} l_{CHAN} \quad (4.4)$$

$$\dot{m}_{MOD,2D} = |(\rho v)|_{max} \frac{2}{3} l_{MOD}^2. \quad (4.5)$$

resulting in

$$l_{MOD}/l_{CHAN} = 1.57080 \quad (4.6)$$

at equal maximum mass flux.

4.2 Suction in a Blasius boundary layer at $Ma=0.5$

The effects of modeled and simulated hole suction are compared in a Blasius boundary layer at $Ma_\infty = 0.5$ (see section 3.3 for relevant base-flow parameters and appendix A for the numerical setup). The center of the suction orifice is located at $Re_{\delta_1} = 1925$ for both cases. This was originally chosen for comparison with experiments [58].

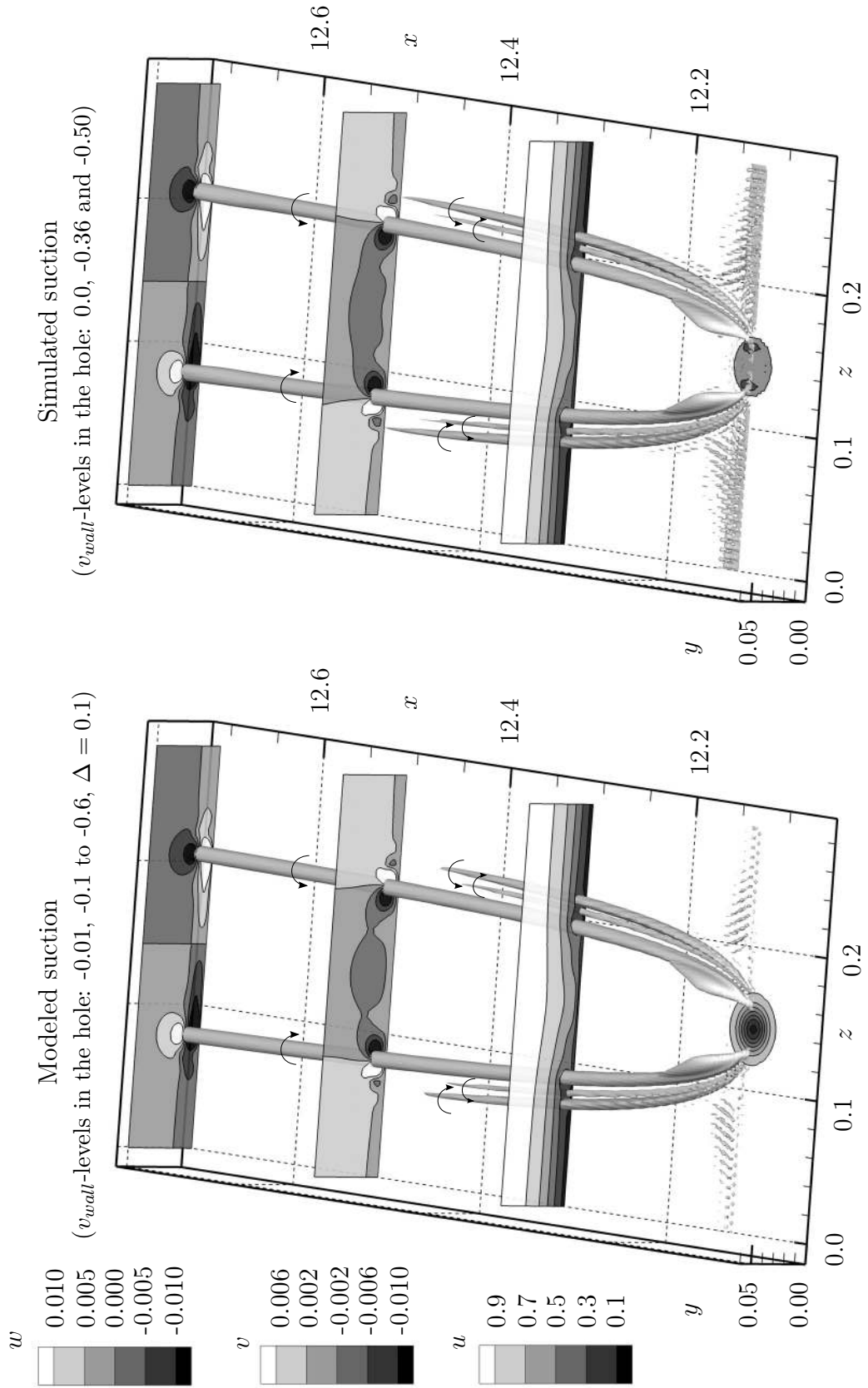
As for the channel simulation, a suction-channel diameter of $2.0 \delta_{1,s}$ is employed at a spanwise spacing of $\lambda_z/\delta_{1,s} = 14.8$; $\delta_{1,s} = 1.925 \cdot 10^{-2}$, $\bar{\delta}_{1,s} = 1.7628 \cdot 10^{-4}m$ is the displacement thickness of the undisturbed base flow at the chordwise location $x = 12.12$ ($\bar{x} = 0.111m$) of the suction hole center. At the pressure level prescribed at the channel outflow, the resulting mass flux corresponds to a Hagen-Poiseuille profile with $(\rho v)_{max} = |-0.597|$. (Note that this corresponds to an area-averaged mass flux of 0.3 which is relatively large compared to standard suction with about 0.1.) This value is consequently used for the simulation with modeled suction where the suction-hole diameter is chosen according to equation (4.3) to yield identical mass fluxes.

Figure 4.1 shows a comparison of vortical structures and velocity crosscuts caused by the modeled and the simulated suction hole. The most obvious difference can be observed for the wall-normal velocity-distributions in the wall orifices. The clean, analytically prescribed modeled distribution consists of concentric isocontours. For the simulated case, almost evenly distributed suction can be observed with two distinct maxima. (A more detailed discussion including all velocity components at various channel crosscuts is provided in the next section for the 3-d boundary-layer flow.) When the resulting vortices are compared, almost identical structures can be found even very close to the suction hole. The only noticeable difference is the streamwise extension of the smaller, secondary structures lying outside of the main vortex pair where the generation is slightly underpredicted in the modeled case. As for the velocity crosscuts only weak deviations can be observed for the sensitive v -component. The overall agreement is excellent. For the given suction rate it is concluded that - assuming equal mass flux - the actual suction-velocity distribution has virtually no influence on the generation of vortical structures. Note that the streamwise extension of the integration domain is too short to capture the region where the main vortex pair decays and eventually disappears.

A comparison of the downstream modal amplitude development of the u' -velocity component is provided in figure 4.2 for the first four steady spanwise modes and the mean-flow deformation $(0,0)$. A simulation with significantly improved wall-normal resolution for the modeled case (not shown) confirms the converged result. Once more, the agreement is excellent justifying the applicability of the employed modeled suction in two-dimensional boundary layers.

A case with differently modeled suction (not shown) employs a top-hat profile for the suction distribution at equal mass flux. Thus, the resulting modeled diameter is smaller than the channel diameter. The amplitude development is almost identical but the spanwise spacing of the counter-rotating structures is somewhat closer, probably due to the more closely spaced edges of the suction hole where the structures emerge. It is concluded that the \cos^3 -distribution is an appropriate choice for modeling suction through a cylindrical channel up to the considered suction rate.

Figure 4.1: Comparison of vortical structures ($\lambda_2 = -5$) and velocity crosscuts for $Ma=0.5$ Blasius flow. Note: λ_2 -structures for $x < 12.12$ are cut off.



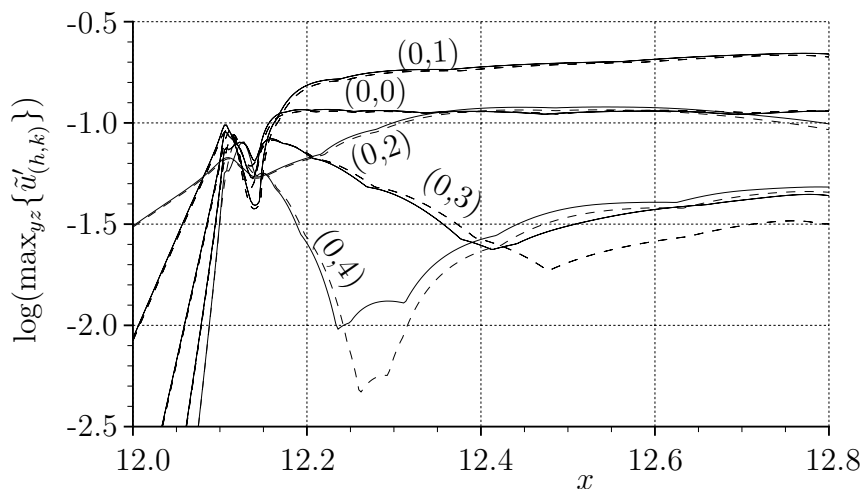


Figure 4.2: Downstream development of selected steady modal $\tilde{u}'_{(0,k)}$ -amplitudes in a $Ma=0.5$ Blasius flow for the modeled-suction case (dashed) and the case with suction channel (solid lines) after Fourier analysis in time. The amplitude level of all unsteady modes is too small for the chosen ordinate values.

4.3 Pinpoint suction in a 3-d boundary layer at $Ma=0.7$

The 3-d boundary-layer flow at $Ma(x_0) = 0.7$ introduced in section 3.2 is employed for the comparison of modeled and simulated “pinpoint” suction in a three-dimensional boundary layer applied for LFC of large-amplitude CFVs with active secondary instability. Since the flow scenario contains now oncoming CFVs, the term pinpoint suction is used to explicate the importance of the hole location relative to the vortex. (Physical aspects of hole suction in the three-dimensional boundary layer without oncoming CFVs are discussed in the next chapter.)

Three cases are considered: The reference case without suction is called REF-07, the case with modeled hole suction (MOD) and the simulation comprising the channel flow (CHAN) employ a single pinpoint suction hole with identical coordinates and mass fluxes; see appendix A for the numerical setup.

For all cases two succeeding disturbance strips at the wall excite steady and unsteady perturbations, respectively, with momentum input but without net

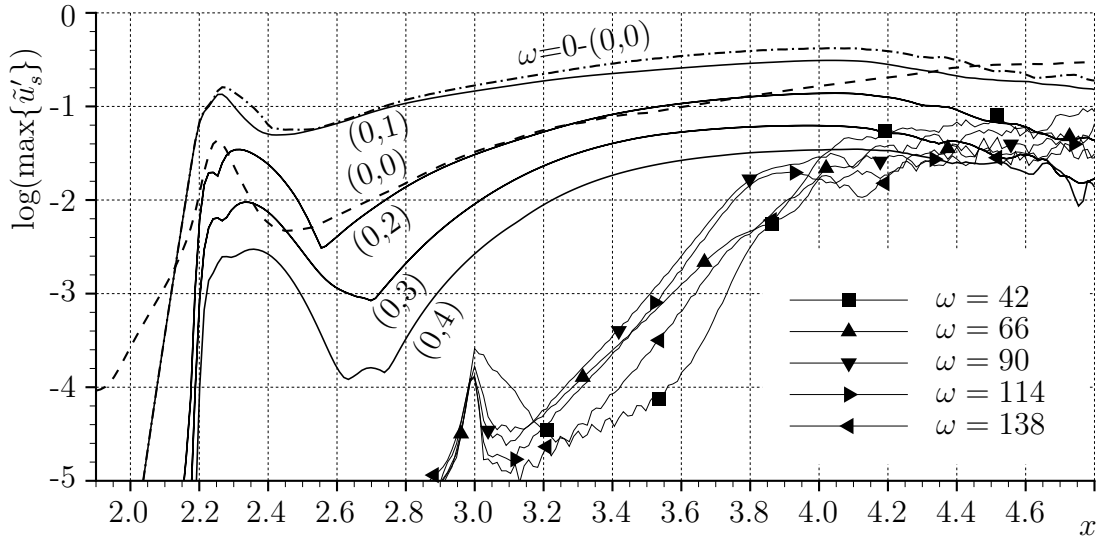


Figure 4.3: Downstream development of modal $\tilde{u}'_{s,(h)}$ - and $\tilde{u}'_{s,(h,k)}$ -amplitudes from Fourier analysis in time (maximum over y or y and z , $\omega = 0$ and $42 \leq \omega \leq 138$, $\Delta\omega = 24$ for case REF-07).

mass flow. Equation (2.8) describes the incompressible disturbance generation; here, the wall-normal mass-flux ρv is prescribed accordingly instead of the wall-normal velocity component v . At $x = 2.20$ the steady vortex mode $(0,1)$ is triggered with an amplitude of $A = 9.3 \cdot 10^{-3}$ whereas at $x = 3.00$ an unsteady, pulse-like disturbance is generated that includes modes $(h, \pm 1)$, $h = 1 - 50$ with amplitudes of $A = 6.25 \cdot 10^{-4}$ and phases $\Theta = 0.0$ (see the inset of figure 5.1 for the resulting time signal). The fundamental spanwise wave number $\gamma_0 = 52.4$ and the fundamental frequency $\omega_0 = 6.0$ are chosen for the simulation representing one of the most amplified primary modes according to LST. Exciting spanwise modes with $\gamma = \pm\gamma_0$ only does not form a limitation since, together with the (large) vortex modes $(0,1)$, $(0,2)$ etc. of the prevailing CFV, the full disturbance spectrum is generated non-linearly at once.

The downstream modal development of the streamline-oriented disturbance velocity component $\tilde{u}'_s = u'_s/u_{b,s,e}$ for the reference case REF-07 without suction is shown in figure 4.3. At $x = 3.00$ the steady and purely three-dimensional part of the mean flow $\omega = 0-(0,0)$, i.e. the steady part of the flow field without the spanwise mean $(0,0)$, reaches 17%. Secondary instability sets in immediately, shown by the growth of high-frequency disturbances, e.g., mode $\omega = 90$

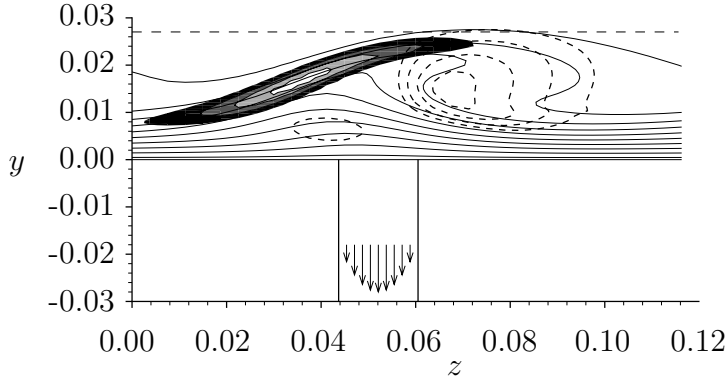


Figure 4.4: Pinpoint-suction setup for the $Ma=0.7$ boundary layer: Crosscut at $x = 3.36$ for case *REF-07* ($t/T_0 = 0.0$) without suction. Solid lines show \tilde{u}_s -isocontours (0.05 to 0.95 , $\Delta = 0.1$), dashed lines show λ_2 -isocontours (-20 to -5 , $\Delta = 5$), modal \tilde{u}'_s -amplitude distribution for high-frequency secondary-instability mode $\omega = 90$ visualized by gray scale (0.3 to 0.9 , $\Delta = 0.2$). Location of the suction channel to be applied marked by two vertical lines (case *CHAN*, crosscut through center of suction channel). The horizontal dashed line denotes the undisturbed boundary-layer thickness $\delta_{99,s}$.

($h = 15$). Starting at $x = 3.60$, non-linear growth of the low-frequency mode $\omega = 42$ ($h = 7$) followed by transition to turbulence can be observed.

When examining y - z -crosscuts of the \tilde{u}'_s -amplitude distributions, low-frequency type-III modes are found in the range $6 \leq \omega \leq 48$, whereas the high-frequency modes ($\omega > 60$) reveal the typical type-I or z -mode amplitude distributions. Mode $\omega = 90$ gains the largest amplitude level at $x = 3.36$. Figure 4.4 shows its location with respect to the clockwise-turning CFV visualized by \tilde{u}_s - and λ_2 -isocontours.

The pinpoint-suction setup is visualized by two vertical lines and arrows that mark the suction channel walls and the sucked flow as applied in case *CHAN*. The center of the suction channel is located at $x = 3.360$ and $z = 0.052$ and a diameter of $d_{CHAN} = 0.01687$ is chosen which corresponds to $d/\delta_{1,s} = 2.00$. The channel outlet is located at $y = -0.250$ which corresponds to approximately $15d$. Details on the choice of the specific location and the underlying physical mechanisms are explained in detail in chapter 5.

After transient effects from the start of the simulation have died out the flow in the suction channel adjusts to the prescribed pressure difference and a steady

flow field can be observed. According to equation (4.1) the integrated mass flux yields a theoretical Hagen-Poiseuille profile with $(\rho v)_{max} = |-0.64239|$. Consequently, case MOD with modeled suction-distribution is set-up with identical hole-center coordinates employing the same maximum mass flux and, according to equation (4.3), a modeled diameter of $d_{MOD} = 0.02542$.

The channel Reynolds number based on the maximum wall-normal mass flux and the channel diameter d is $Re = |\bar{\rho}\bar{v}|_{max}\bar{d}/\bar{\mu} = 970$ and well below the critical Reynolds number $Re_{crit} = 2300$ for pipe flow with sharp-edged inlet based on the average channel velocity. Furthermore, to check for possible oversuction, a critical Reynolds number Re_{kk} is evaluated according to the “equivalent roughness model” (ERM) [48, 58]. If the height of the sucked streamtube is h_k (measured sufficiently far upstream of the suction hole) and the corresponding actual local streamwise velocity component is $u_{k,s}$, the equivalent roughness Reynolds number is defined as $Re_{kk,ERM} = \bar{h}_k\bar{u}_{k,s}/\bar{\nu}$. The values yield $Re_{kk} \approx 350$ for cases MOD and CHAN, being well below the observed, critical values found, $700 < Re_{kk} < 800$, in the same boundary-layer flow [58]. Note that the critical *roughness* Reynolds number, defined as $Re_{kk,crit} = \bar{k}\bar{u}_k/\bar{\nu}$, based on the roughness height k and the corresponding streamwise velocity component of the reference base flow u_k , is typically much smaller. Authors give values of 350 for hemispherical roughness elements and 600 or higher for cylindrical shapes, however, evaluated in two-dimensional base flows, cf. the overview in [58]. The corresponding oversuction cases in a Blasius boundary layer suggest critical values above $Re_{kk} = 1400$. Therefore, the critical equivalent roughness Reynolds numbers for suction cases seem to be higher by a factor of 2, and, as already concluded in [58], the ERM seems questionable.

The effect of pinpoint suction becomes obvious in figure 4.5 where the modal downstream development of disturbances for cases MOD and CHAN is compared. The attenuation of the CFV is identical in both cases and a reduction from 26% amplitude level at $x = 3.45$ to less than 14% at $x = 3.64$ can be found for $\omega = 0 - (0, 0)$. The accompanying weakening of secondary amplification is somewhat stronger in case CHAN considering the amplitude level, suggesting that case MOD slightly underpredicts the attenuating effect of pinpoint suction rendering the modeling intrinsically rather conservative. The growth rates coincide well for corresponding modes.

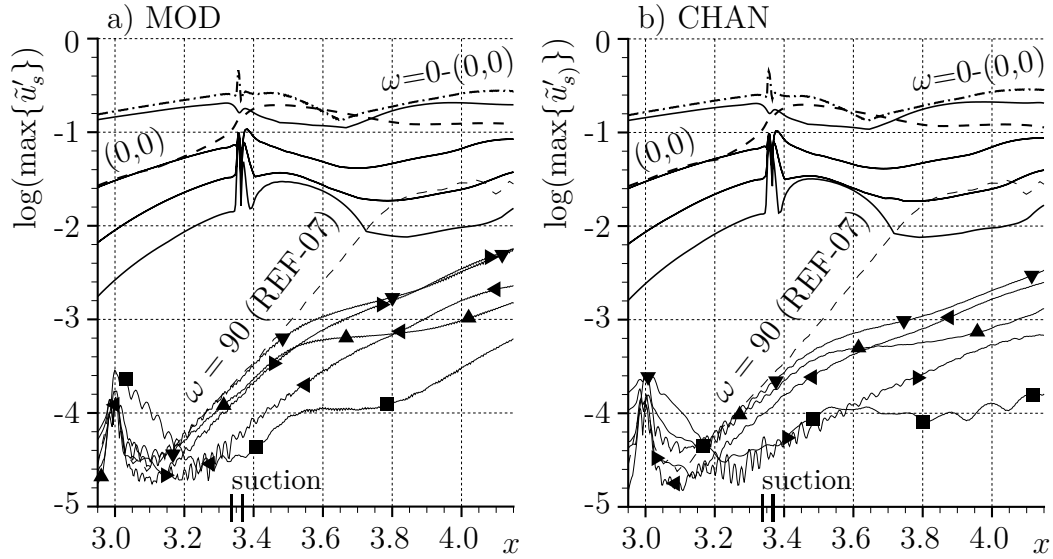


Figure 4.5: As figure 4.3 but for cases MOD and CHAN. Mode $\omega = 90$ from case REF-07 has been added as reference (dotted line).

Crosscuts through the CFVs at $x = 3.72$ are shown in figure 4.6 for all three cases. Isocontours of the streamwise \tilde{u}_s -velocity component as well as eigenfunctions for mode $\omega = 90$ highlight the relevant shear-layer regions. The effect of pinpoint suction can be found in the reduction of the CFV strength indicated by the less-deformed \tilde{u}_s -velocity isocontours for cases MOD and CHAN and also by the reduced size of the vortex shown by the λ_2 -isocontours. Moreover, the shape of the eigenfunction reveals less localized-acting secondary instability. The agreement for cases MOD and CHAN is excellent.

Note the small, newly appearing structure at $z = 0.096$, $y = 0.008$, for cases MOD and CHAN which is a relict from a suction-hole-induced vortex. A further discussion is again postponed to chapter 5.

Figure 4.7 provides a top view of vortical structures for all cases in a rotated reference system (for details on the used coordinate systems see appendix D) that is chosen to approximately show straight CFVs. The snapshot for case REF-07 reveals undisturbed flow up to $x_r = 0.9$. The small structures at $x_r = 1.0$ show the disturbance pulse in an early stage. The turbulent region between $x_r = 1.6$ and $x_r = 2.5$ is caused by the previous pulse and full turbulence starts at $x_r = 3.0$. Postponed transition can be found for

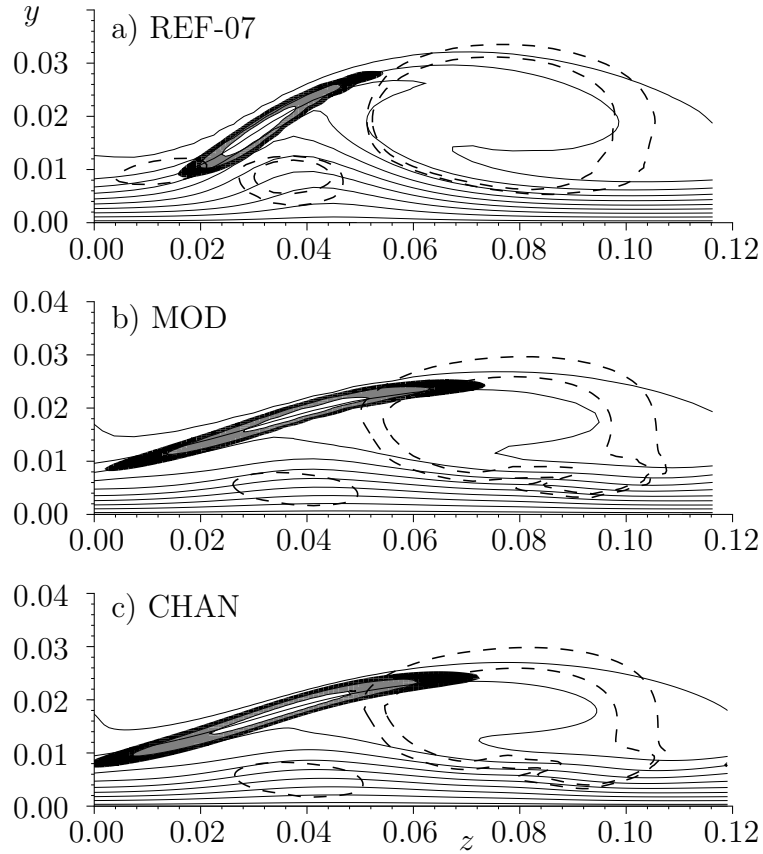


Figure 4.6: Crosscuts at $x = 3.72$ showing \tilde{u}_s -isocontours (solid lines, 0.05 to 0.95, $\Delta = 0.1$), λ_2 -isocontours (dashed lines, levels -1 and -5) and the normalized u_s -amplitude distribution for mode $\omega = 90$ (shaded, levels 0.5, 0.7, and 0.9) at time level $t/T_0 = 0.2$.

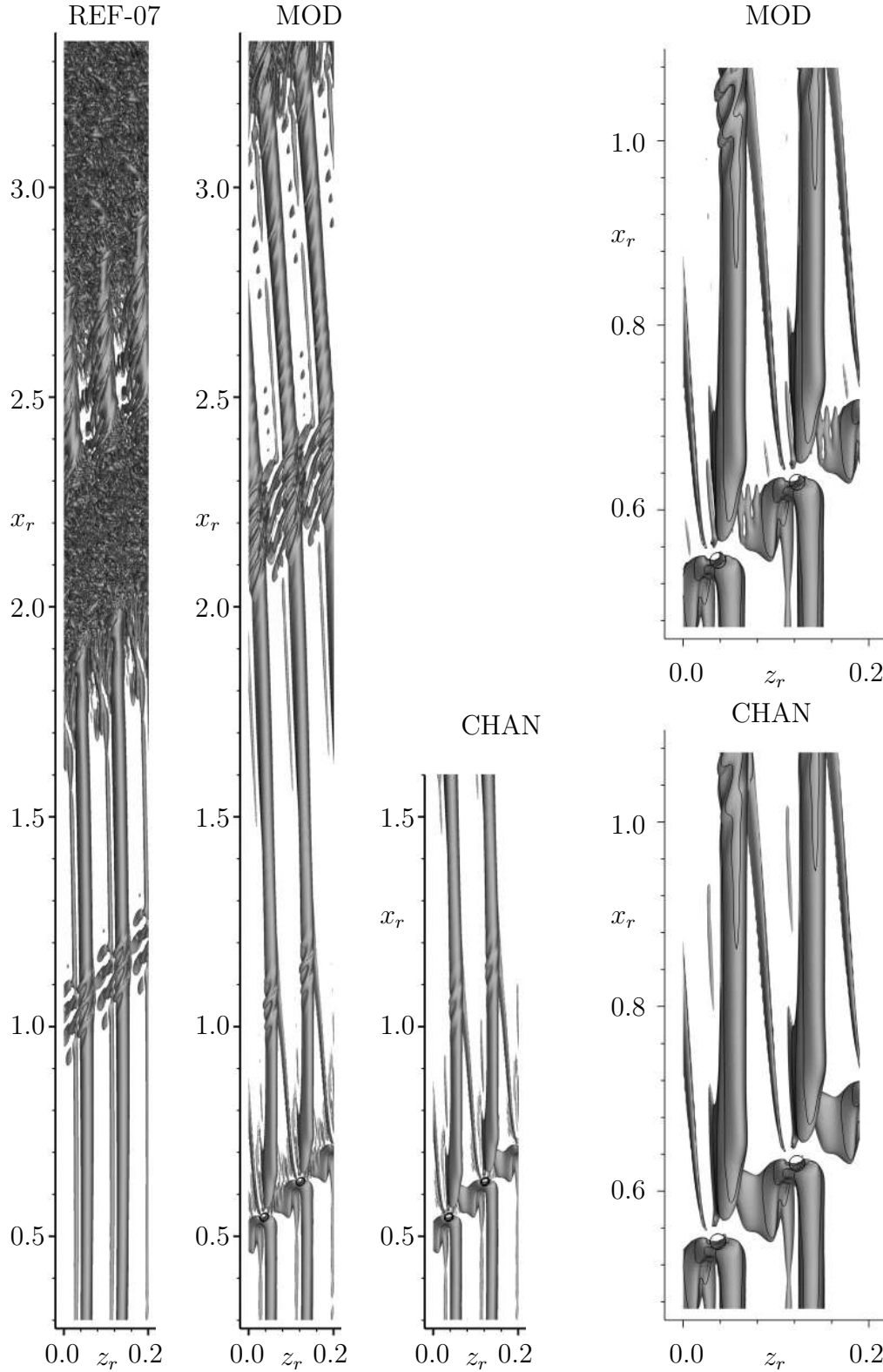


Figure 4.7: Vortex visualization ($\lambda_2 = -5$), top view, snapshot in time ($t/T_0 = 0.0$), to scale, for cases *REF-07*, *MOD*, and *CHAN*. Right plots show a zoom of the structures in the vicinity of the suction hole; lines show wall-normal isocontours. The suction holes are marked by black circles. A rotated reference system is used with $x_{r0} = 3.0$, $z_{r0} = 0.0$, $\Phi_r = 45.0^\circ$.

case MOD where the equivalent secondary structures described for case REF-07 are on a much lower level and hence transition occurs only later in the considered domain. Due to the large numerical demands of the computation with suction channel a shorter integration domain is chosen for case CHAN. The comparison is therefore available only up to $x_r = 1.6$ but provides very good agreement. The close-ups show almost identical structures evolving from the suction orifices with slightly more pronounced secondary structures in case MOD which is in agreement with the earlier-observed larger amplitude level of secondary modes. The near-wall, spanwise periodic structures in case MOD result from the coarser spanwise grid which is however sufficient considering the alike downstream evolution of vortical structures.

The flow fields of cases MOD and CHAN are compared in more detail in figures 4.8-4.12 where a distinct rotated coordinate system (ξ, y, ζ) is chosen such that its origin coincides with the suction hole center (cf. appendix D). Note that in a boundary layer with crossflow the streamline direction varies with the distance from the wall and thus the chosen angle $\phi_r = 45.0^\circ$ does not coincide with the potential streamline direction outside the boundary layer, $\phi_e(x = 3.36) = 49.2^\circ$, but rather follows the local flow direction in the boundary layer which coincides well with the orientation of the CFV cores. The crosscuts at $\zeta = 0.0$ and $\xi = 0.0$ in figure 4.8 reveal the flow fields in this very local streamwise and spanwise flow direction through the suction-hole center. The agreement of the flow fields for $y > 0.0$ is perfect. Wall-normal mass flux ρv and projected streamlines are shown in the left column. Differences can be observed only for a very small region directly above the suction hole, but the far-field distributions are identical and also the streamlines coincide. The suction channel shows a large region of positive ρv at the left side indicating steady separation ($-0.026 < y < 0.000$). The maximum suction lies downstream of the center of the channel. The right column shows the local streamwise velocity component u_r and pressure levels in a spanwise crosscut. The water-wave shapes are identical for both cases and also the pressure level 1.07 coincides fairly well. Close to the wall the pressure distributions show minor deviations due to the suction modeling. The channel flow reveals a symmetrical and for a decreasing y -coordinate decaying u_r -component.

Figure 4.9 gives a comparison of the wall-pressure distributions. Differences

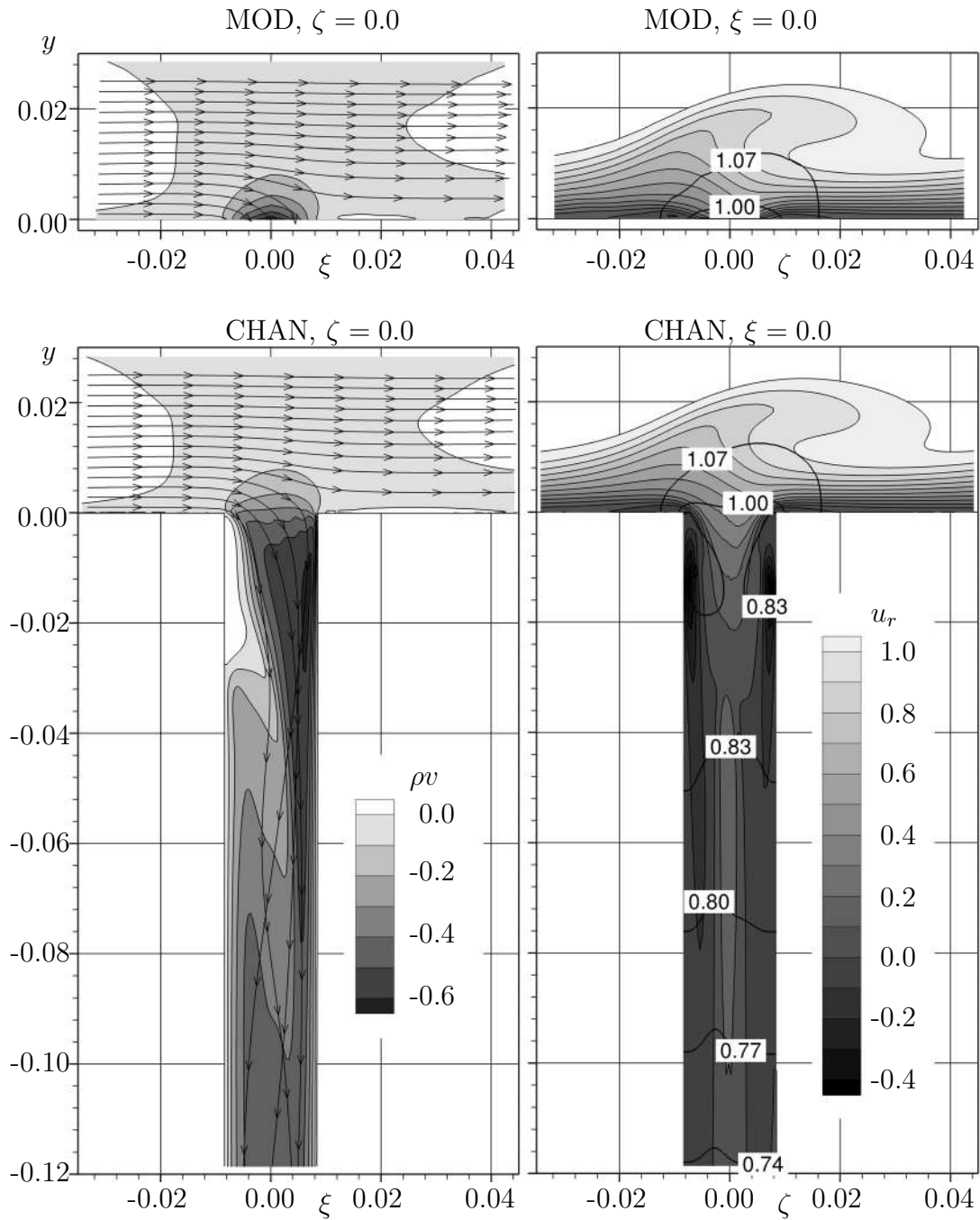


Figure 4.8: Crosscuts for cases MOD and CHAN. Left column shows ρv -distributions (shaded) and projected $[u,v,w]$ -streamlines. Right columns shows u_r -isocontours (shaded) and pressure levels p (thick lines). A distinct rotated coordinate system (ξ, y, ζ) is used with $\phi_r = 45^\circ$ and x_{r0} and z_{r0} being the hole-center coordinates. Note that the channel extends up to $y = -0.25$.

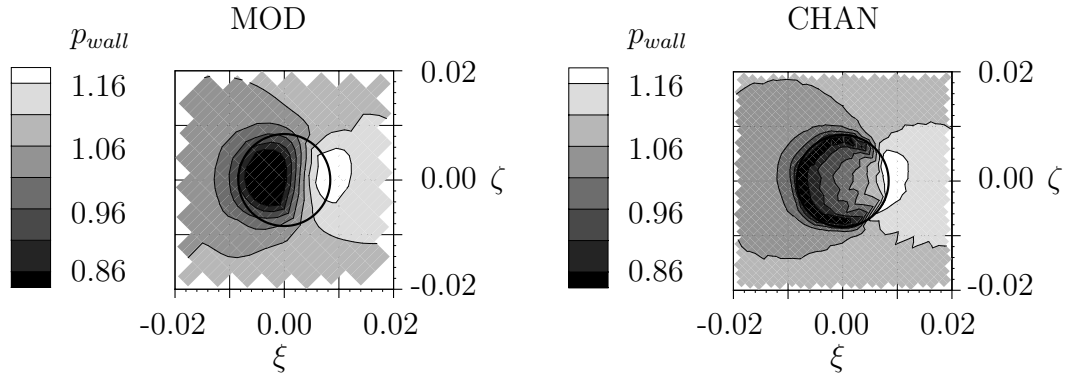


Figure 4.9: Wall-pressure distributions for cases MOD and CHAN. The wall of the suction channel is marked in both figures by a black circle. The coordinate system from figure 4.8 is used.

occur only above the suction orifice due to the differing velocity distributions but the wall-pressure distributions outside the holes coincide well.

Wall-normal crosscuts of velocity and mass-flux distributions are provided in figure 4.10. At $y = +d$ the wall-normal mass fluxes are compared right above the suction centers and very good agreement is found. At the wall, ρv and v show qualitatively similar distributions for the channel case and are scaled only by the density value. The crosscuts for u_r and w_r show the actual streamwise and spanwise velocity components at $y = 0.0$ (that are zero in the modeled case) and values up to 50% or 20% can be observed, respectively. The channel-flow evolution is shown by two more crosscuts at $y = -d$ and $y = -5d$ revealing u_r - and w_r -components below 10% while the wall-normal mass flux approaches the theoretical Hagen-Poiseuille distribution.

Wall-normal profiles along the suction-hole center can be found in figure 4.11 for the six flow variables. The u_r -profile is deformed above the suction hole and approaches a value of 0.4 close to the wall, surprisingly also in the modeled case. The imposed no-slip suction distribution forces here the value to be zero at the wall which creates a large wall-normal gradient. This is most likely the explanation for the demanding wall-normal resolution of the incompressible, vorticity-based code considering that the variable ω_z is mainly determined by $\partial u / \partial y$ and the equation system includes second derivatives of all

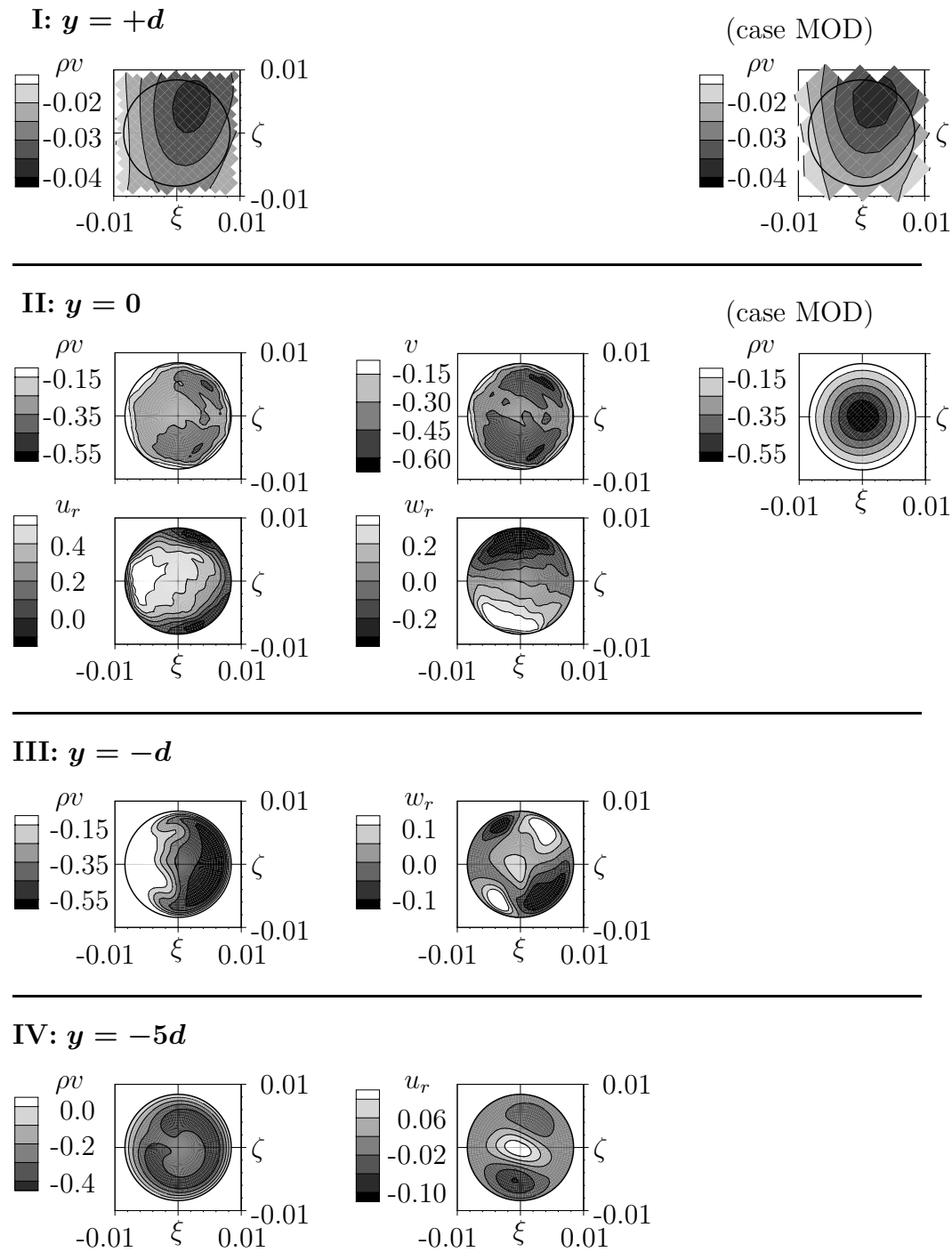


Figure 4.10: Wall-normal crosscuts providing various velocity/mass-flux distributions at four locations for case CHAN (left two columns). For case MOD, two ρv -distributions are shown at $y = +d$ and $y = 0$ (right column). The respective crosscut locations are marked in figure 4.11. The coordinate system from figure 4.8 is used.

$$\xi = 0.0, \zeta = 0.0$$

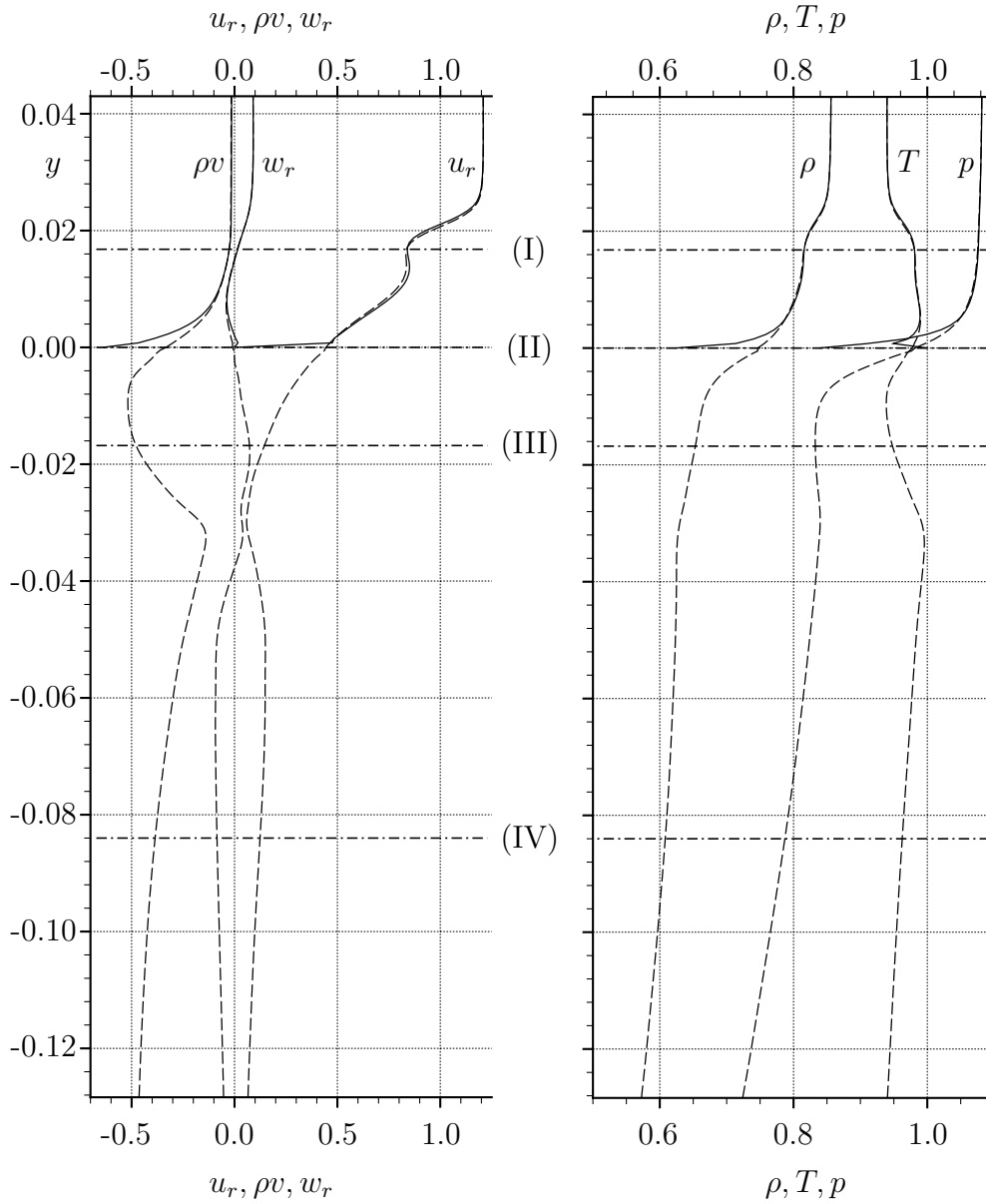


Figure 4.11: Wall-normal profiles of selected flow variables for cases CHAN (dashed lines) and MOD (solid lines) at the suction hole center. Note that the shape of the v -profile is only marginally influenced by the density variation and therefore not additionally shown. The coordinate system from figure 4.8 is used. Horizontal lines (I) through (IV) mark crosscut locations shown in figure 4.10.

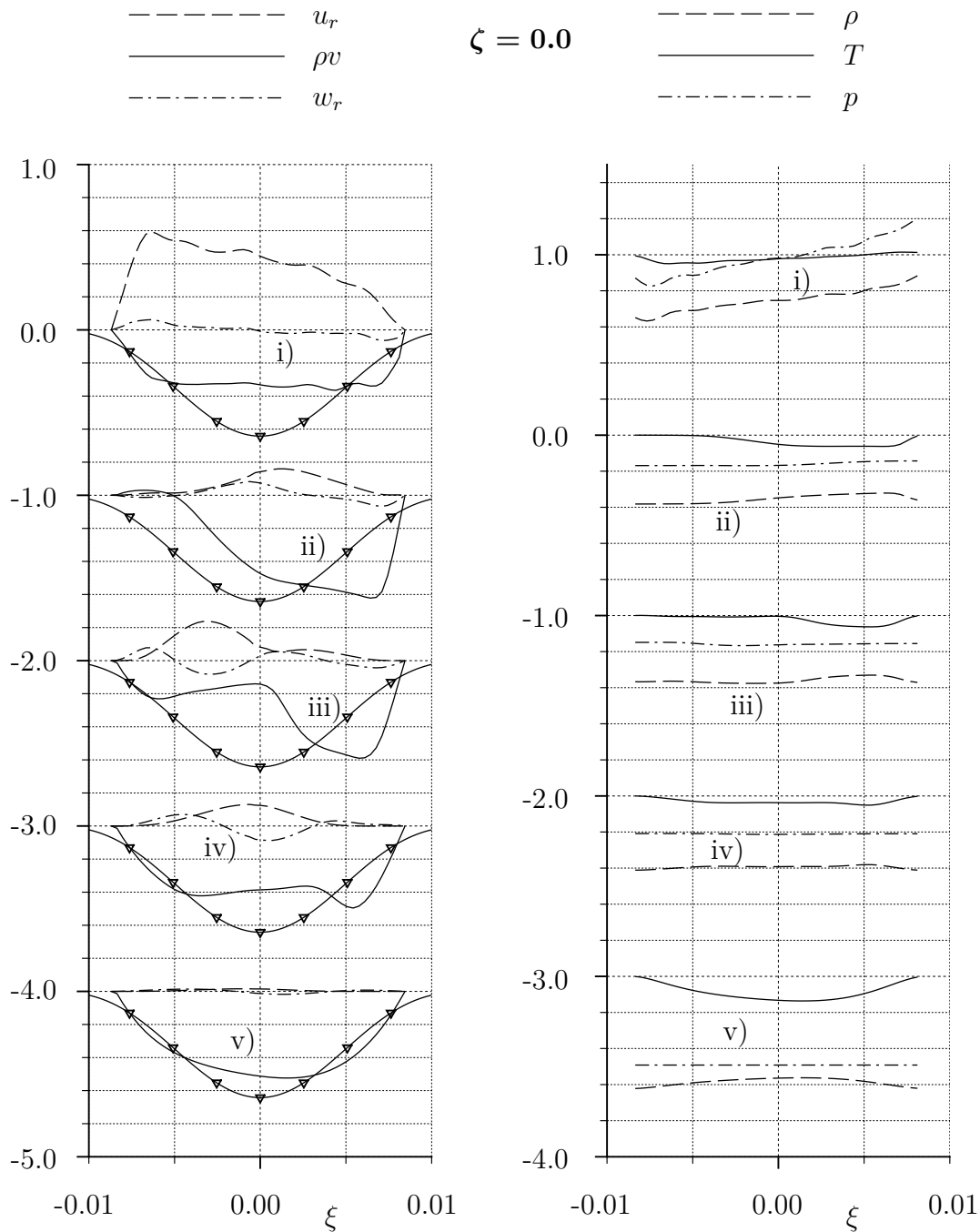


Figure 4.12: Profiles of selected flow variables vs. local streamline direction ξ in the plane $\zeta = 0.0$ for case CHAN at five channel locations: i) $y = 0.0$, ii) $y = -d$, iii) $y = -2d$, iv) $y = -5d$, v) $y = -15d$. The ordinates are defined in subfigures i) and successively shifted by -1.0. for ii)-v). The modeled ρv -distribution from case MOD at the wall is added for comparison (solid line with symbols) in the left figure. The coordinate system from figure 4.8 is used.

vorticity components. In the channel case the u_r -component approaches zero for increasing channel-flow direction $-y$, as does w_r . The crossflow profile w_r does not vanish outside the boundary layer since the chosen coordinate system does not coincide with the (potential) streamline-oriented one as explained above. The wall-normal mass flux ρv is almost zero outside the boundary layer with increasing negative values when approaching the wall. The modeled wall-value of -0.64 is never reached in the channel case where a maximum of -0.50 can be found for large $|-y|$ suggesting that the theoretical Hagen-Poiseuille distribution has not yet been reached. Density, temperature and pressure profiles show the resulting distributions of the prescribed low pressure region at the channel outlet.

The according profiles for varying ξ -coordinate at $\zeta = 0.0$ are provided in figure 4.12 for five channel positions and show the distributions in local flow direction. For comparison, the prescribed modeled suction distribution is added in the left figure at every position. In subfigure ii) the maximum suction mass flux can be found at $\xi = 0.007$ whereas the positive values at $\xi = -0.007$ reveal the separated flow region. Note that the total sucked mass flux is determined by the area integral of ρv and the line integrals of ρv do not yield equal values at equal mass flux. The distributions of ρ , T , and p result from the pressure gradient and the chosen isothermal-wall boundary condition.

A visualization of vortical structures for the channel flow is provided in figure 4.13. The left subfigure shows the main domain of case CHAN and the channel domain in a three-dimensional view. The channel domain can be found separately in the right subfigure at a higher λ_2 -level including various crosscuts that show isocontours of the wall-normal velocity component. Recall that the local flow direction corresponds approximately to the coordinate x_r . The emerging structures are symmetrical to some extent with respect to the oncoming flow direction. The corresponding structures wind around the channel center and decay with increasing $|-y|$ coordinate. The separated flow region is visualized by positive v -values in the two wall-near crosscuts.

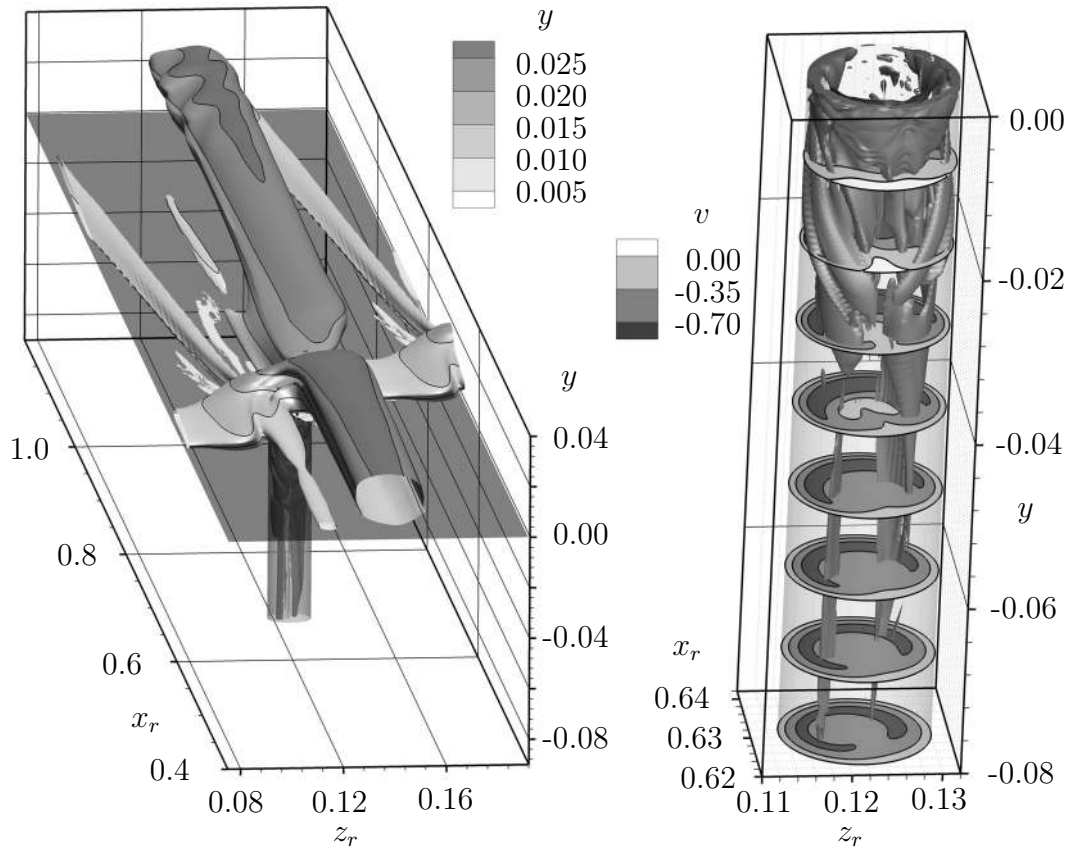


Figure 4.13: Results of the simulation with suction channel. Left: Visualization of vortical structures, $\lambda_2 = -5$ including isocontours of the wall-normal coordinate y . Right: $\lambda_2 = -80$, and crosscuts with isocontours of the wall-normal velocity-component v . The coordinate system of figure 4.7 is used. To scale.

5 Control of crossflow transition

All results in this chapter are obtained from the incompressible, vorticity-based numerical method introduced in section 2.1. Subject of investigation is the incompressible base flow that represents the 3-d boundary-layer flow of the DLR Göttingen “Prinzipexperiment”. The goal of all applied suction setups - using modeled suction throughout this chapter - is the drag reduction by maintaining laminar flow as long as possible. In the most considered scenarios this is achieved by the pinpoint-suction concept where one or several suction holes are placed underneath the updraft-turning side of a grown crossflow vortex (CFV) which can substantially postpone the location of laminar-turbulent transition.

The following simulation cases are considered (for a tentative study see [24] and for a subset see also [20]): The reference case REF is used as the basis for the transition process without suction and for comparison. It includes the generation of a large-amplitude CFV with triggered, active secondary instability leading to transition to turbulence. All remaining cases employ the same disturbance generation - unless stated otherwise - but additionally some kind of suction: Case HOM shows the effect of homogeneous suction in a chordwise finite area of the integration domain. Cases 1-H, 3-H, 3-H*, and 9-H are set up with one, three, or nine successive, identical suction holes at the wall, positioned along one CFV. Spanwise suction slits are considered in cases 3-S, 1-S, and 3-S* employing different suction rates. The numerical parameters for the various cases are given in table A.1 of appendix A and table 5.1 summarizes parameters for the suction generation.

Note that the values d and l are the hole diameters and slit extensions from Hagen-Poiseuille and plane Poiseuille profiles, respectively, that correspond to the actually computed cases with the numerical parameters d_{mod} and l_{mod} at identical sucked mass flux. Thereby, d and l would directly represent the dimensions of a respective channel setup.

5. CONTROL OF CROSSFLOW TRANSITION

Case	suction setup	c_q	v_{max}	v_{avg}	$d \times 10^2$	$P \times 10^2$	$v_{avg,mod}$	$d_{mod} \times 10^2$	$P_{mod} \times 10^2$	suction centers at x_H
REF	-	-	-	-	-	-	-	-	-	-
HOM	homogeneous	$c_{q,0}$	0.0016	0.0016	-	100.0	-	-	-	3.15 – 4.05, $l_x = 0.90$
1-H	1 hole	$c_{q,0}/3$	0.5000	0.2500	1.73	0.218	0.1092	2.62	0.499	3.36
3-H/3-H*	3 holes	$c_{q,0}$	0.5000	0.2500	1.73	0.653	0.1092	2.62	1.498	3.36, 3.38, 3.40
3-S	3 slits	$c_{q,0}$	0.0463	0.0308	$l=1.59$	5.300	0.0217	$l_{mod} = 2.50$	8.320	3.36, 3.38, 3.40
1-S	1 slit	$\approx c_{q,0}$	0.5000	0.3333	$l=0.50$	0.560	0.2122	$l_{mod} = 0.79$	0.756	3.36
3-S*	3 slits	$3 c_{q,0}$	0.0463	0.0308	$l=1.59$	5.300	0.0651	$l_{mod} = 2.50$	8.320	3.36, 3.38, 3.40
9-H	9 holes	$3 c_{q,0}$	0.5000	0.2500	1.73	1.960	0.1092	2.62	4.491	3.36, 3.38, ..., 3.52

Reference suction coefficient $c_{q,0} = 1.63 \cdot 10^{-3}$

$v_{max} = \bar{v}_{max}/\bar{U}_\infty$

Spanwise location of suction-hole centers for cases 1-H, 3-H, and 9-H: $z_H = 0.5 \cdot \lambda_{z,0} = 0.06$, for case 3-H*: $z_H = 0.0$

Reference area for porosity: $A_{hom} = \lambda_{z,0} \cdot l_x = 0.108$

Table 5.1: Simulation setups.

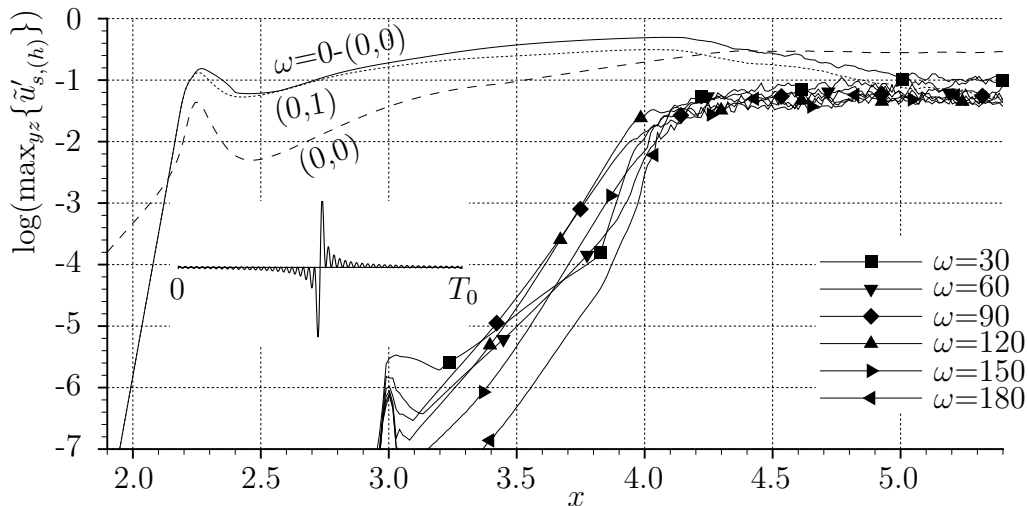


Figure 5.1: Downstream development of modal $\tilde{u}'_{s,(h)}$ -amplitudes for case REF from Fourier analysis in time (maximum over y and z , $0 \leq \omega \leq 180$, $\Delta\omega = 6$). The inset shows the physical time signal of the pulsing.

5.1 Reference case and pinpoint suction setup

For all cases two succeeding disturbance strips excite steady and unsteady modes similarly to the procedure described in section 4.3 for the compressible setup but here the wall-normal velocity component at the wall is prescribed as defined in equation (2.8). At $x = 2.20$ the fundamental steady vortex mode $(0,1)$ is triggered with an amplitude of $A = 9.30 \cdot 10^{-3}$ whereas at $x = 3.00$ the unsteady, pulse-like disturbance is generated that includes modes $(h, \pm 1)$, $h = 1 - 50$, here excited on a lower amplitude level of $A = 6.25 \cdot 10^{-7}$ and $\Theta = 0.0$. The same fundamental spanwise and timewise wavenumbers $\gamma_0 = 52.4$ and $\omega_0 = 6.0$ are chosen.

The downstream modal development of the streamline-oriented disturbance velocity component $\tilde{u}'_s = u'_s/u_{b,s,e}$ for the reference case REF without suction is shown in figure 5.1. A high initial amplitude of mode $(0,1)$ is chosen as before to skip the linear development of the crossflow vortex mode. The linear stage has been extensively discussed in [12] and left out here to save computational resources. (A comparison of the induced CFV shows no notable differences to cases where the fundamental mode was triggered on a lower amplitude level.) At $x = 3.00$, the steady three-dimensional part of the mean flow $\omega = 0 - (0, 0)$

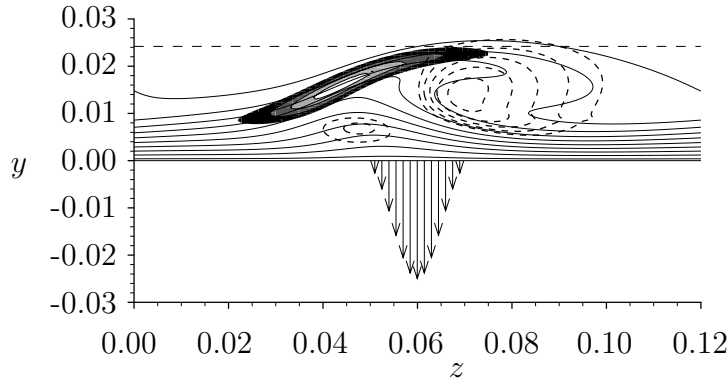


Figure 5.2: *Pinpoint suction setup: Crosscut at $x = 3.36$ for case REF without suction. Solid lines show \tilde{u}_s -isocontours (0.05 to 0.95, $\Delta = 0.1$), dashed lines show λ_2 -isocontours (-25 to -5 , $\Delta = 5$), modal \tilde{u}'_s -amplitude distribution for high-frequency secondary-instability mode $\omega = 90$ visualized by gray scale (0.3 to 0.9, $\Delta = 0.2$). Arrows show pinpoint-suction distribution at the wall to be applied (case 1-H, crosscut through center of suction hole). The horizontal dashed line denotes the undisturbed boundary-layer thickness $\delta_{99,s}$.*

reaches 19% and secondary instability of high-frequency modes sets in. Non-linear growth of the low-frequency modes followed by transition to turbulence can be observed starting at $x = 3.75$.

Note that without unsteady forcing the simulated flow breaks down to turbulence for $x > 5.5$ only. In this case the strong convective secondary instability caused by the large-amplitude CFVs amplifies the small numerical background noise ($O(\tilde{u}'_s) = 10^{-12} - 10^{-15}$) and it takes until $x = 5.5$ to reach the turbulent state. The forcing of unsteady pulse disturbances has been applied to keep the integration domain short for the various cases considered.

The \tilde{u}'_s -amplitude distributions show low-frequency type-III modes in the range $6 \leq \omega \leq 48$, and high-frequency modes ($\omega > 60$) reveal typical type-I or z -mode distributions. Figure 5.2 shows the distribution of mode $\omega = 90$ with respect to the clockwise-turning CFV visualized by \tilde{u}'_s - and λ_2 -isocontours. The pinpoint-suction setup is visualized by arrows indicating the prescribed suction velocity at the wall as applied in case 1-H.

The suction position shown is (near-) optimal with respect to secondary-growth attenuation and has been found iteratively. It is not exactly beneath

the maximum of the z -mode. Note that as explained in section 4.3 the stream-line direction varies with the distance from the wall.

5.2 Downstream development of disturbances for cases with suction

First, the homogeneous-suction case HOM is considered. A suction coefficient using the free-stream velocity in chordwise direction is defined by

$$c_q = \frac{\bar{v}_{avg} \cdot P}{\bar{U}_\infty}, \quad (5.1)$$

where $\bar{v}_{avg} = 1/A \int v \, dA$, A - orifice area, is the average suction velocity over the suction orifice and P the porosity of the suction panel. A value of $c_{q,0} = 1.63 \cdot 10^{-3}$ on a chordwise extension of the suction domain of $l_x = 0.9$ is chosen for case HOM according to table 5.1. The homogeneous suction operates at $v = v_{max} = 0.0016$ ($P = 1$) and covers the complete spanwise domain. The increase of the spanwise mean $(0,0)$ between $3.15 \leq x \leq 4.05$ in figure 5.3a is a consequence of the homogeneous suction. Little influence on the main vortex is observed, visualized by $\omega = 0 - (0,0)$. A slight reduction of secondary amplification is found for all considered high-frequency modes compared to the selected reference mode $\omega = 120$ from case REF that gained the highest amplification rate. However, transition to turbulence is only marginally delayed.

The first pinpoint-suction case 1-H is set up by selecting the location of the suction-hole center ($x_H = 3.356$, $z_H = 0.060$) according to figure 5.2 and choosing a hole diameter of $d = 0.0173 = 2.30 \delta_{1,s}(x_H)$. The maximum suction velocity is $v_{max} = \bar{v}_{max}/\bar{U}_\infty = 0.5$, corresponding to $v_{max}/u_{b,s,e} = 0.413$. Slight variations of the spanwise location of the hole center have only a minor influence on the attenuating effect of the suction.

If the reference area from case HOM is considered ($A_{hom} = \lambda_{z,0} \cdot l_x$), the porosity for case 1-H yields $P = \pi d^2/4/A_{hom} = 0.0022$ and the suction coefficient results in $c_q = 5.45 \cdot 10^{-4}$ which is $c_{q,0}/3$.

The localized suction influences the vortex strength, see figure 5.3b. The y - z -maximum of the steady, three-dimensional \tilde{u}'_s -deformation of the flow $\omega =$

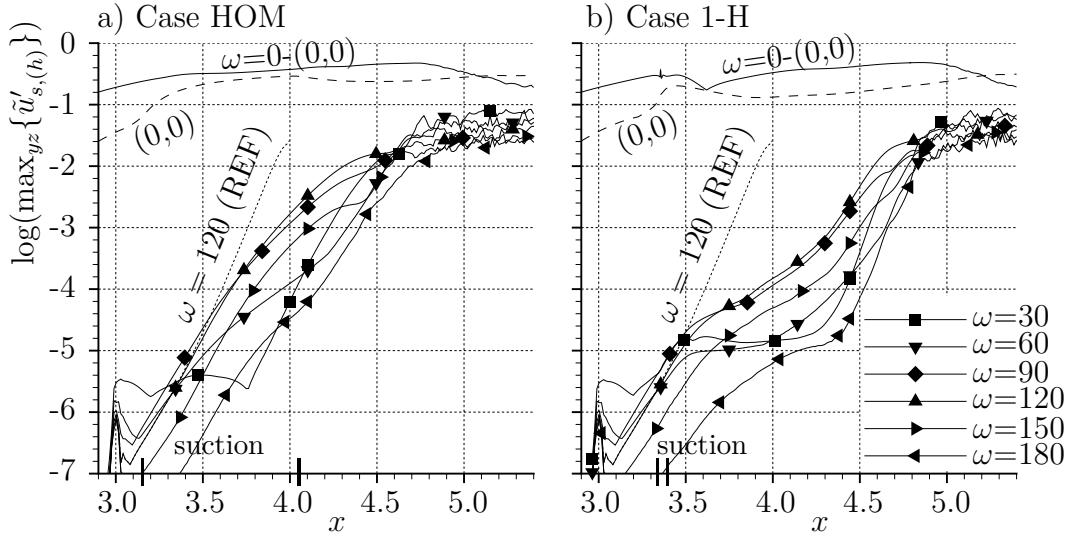


Figure 5.3: Downstream development of modal $\tilde{u}'_{s,(h)}$ -amplitudes from Fourier analysis in time (maximum over y and z , $0 \leq \omega \leq 180$, $\Delta\omega = 30$). Mode $\omega = 120$ from case REF has been added as reference (dotted line).

$0 - (0,0)$ shows a significant reduction behind the suction hole, its amplitude dropping from 0.30 to 0.17. Secondary growth of all modes is affected immediately and significantly reduced. Only after $x = 4.3$, the former amplification rates are regained due to the re-grown CFV. The transition delay is about the same as in case HOM, but with 67% less suction mass flow.

The influence of the diameter and the mass and momentum input are summarized in appendix E. The main finding is that the mass flux sucked is the most important parameter with respect to secondary-growth attenuation rather than the maximum suction velocity and thus the wall-normal momentum output at the considered rates.

To check for oversuction, the parameter Re_{kk} , defined in section 4.3, is evaluated in a case without oncoming vortex. For a single hole and suction parameters identical to case 1-H, Re_{kk} reaches 335 and is well below the observed critical values $700 < Re_{kk} < 800$ [58].

To increase the sucked mass flow, more holes are added to prevent oversuction caused by one hole with an unduly large suction velocity \bar{v}_{avg} . Three succeeding suction holes, each with the same suction parameters as the single hole in case 1-H, are set up, resulting in $c_q = c_{q,0}$. The hole centers are

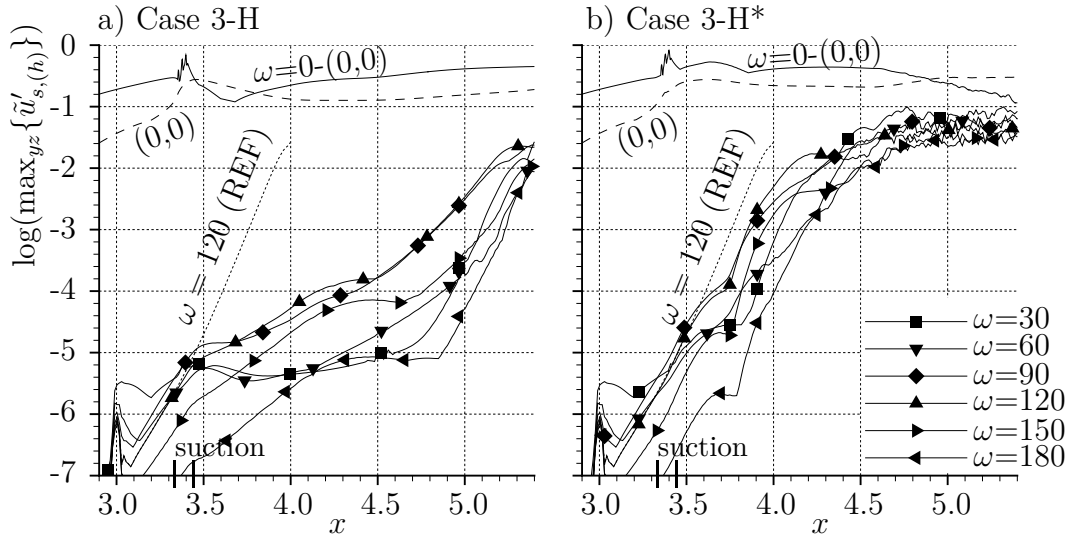


Figure 5.4: Like figure 5.3 but for cases 3-H and 3-H*.

aligned on a straight line, parallel to the vortex-core orientation at $x = 3.36$. Results for this case, called 3-H, are provided in figure 5.4a. In spite of a local increase the vortex amplitude level is reduced to 0.12 at $x = 3.7$, and stronger secondary-growth attenuation can be observed for all unsteady modes. Transition is shifted to the end of the considered domain. Note that one length unit ($\bar{L} = 0.1$ m) corresponds to $133 \cdot \delta_{1,s}$ at $x = 3.36$.

In order to check the influence of the spanwise suction-hole position, case 3-H* is set up with all three suction holes shifted by $\lambda_{z,0}/2$. This is pessimal considering the spanwise spacing and sense of rotation of the CFV. Figure 5.4b shows indeed an enhancement of the CFV strength to a maximum value of more than 53% at $x = 3.65$. However, the overall effect of the suction seems to overcome the misalignment drawback, and transition is at least not enhanced. Therefore it is concluded that a varying spanwise location of the suction holes can either enhance or weaken the CFV amplitude, but secondary instability is always weakened due to deformation of the CFV and the mean suction effect, pulling the flow to the wall.

To further investigate the role of the spanwise position of suction, case 3-S with three consecutive spanwise slits is set-up at the same chordwise locations as for case 3-H. No spanwise variation of suction is present, but in contrast to case HOM it is localized in the chordwise direction. With our spectral code this is simply achieved by neglecting $v'_k(y = 0)$ for $k > 0$, since the spanwise slit

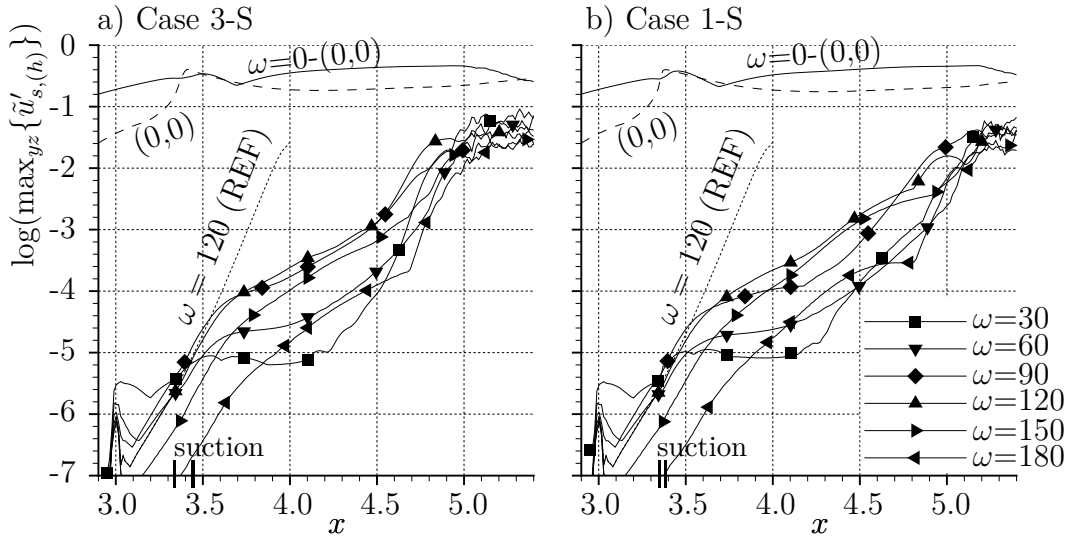


Figure 5.5: Like figure 5.3 but for cases 3-S and 1-S.

represents the spanwise mean component $v'_{k=0}(y=0)$ of a case with a suction hole. The suction coefficient $c_q = c_{q,0}$ corresponds to cases HOM and 3-H but the maximum suction velocity reduces from 50.0% to 4.63%. (Note that by this procedure the three consecutive slits overlap marginally in chordwise direction and the resulting slit length given in table 5.1 does therefore not exactly match the value of the employed hole diameters of case 3-H.) Figure 5.5a shows that the resulting transition delay lies in between cases 1-H and 3-H. The chordwise concentration of suction improves transition delay compared to homogeneous suction, however, the slit suction does not perform as well as case 3-H at identical c_q -values.

To further increase the chordwise concentration of suction case 1-S is set-up with a single suction slit operating at $v_{max} = 0.50$. A similar suction coefficient as in cases HOM, 3-H, and 3-S can be achieved by choosing a slit length of $l_{1-S} \approx 1/3 l_{3-S} = 0.005$ represented by $6\Delta x$, yielding $c_q = 1.852 \cdot 10^{-3} \approx c_{q,0}$. The resulting transition delay is provided in figure 5.5b and shows no significant improvement with respect to case 3-S. Also, the influence on the main vortex is virtually identical. It is concluded that the optimal chordwise concentration for slit suction has already been reached with case 3-S.

To further increase the mass flux the maximum suction velocity for the next case 3-S* is multiplied by a factor of 3 compared to case 3-S, yielding a maximum suction velocity of 13.8% and $c_q = 3 \cdot c_{q,0}$. Figure 5.6b shows a

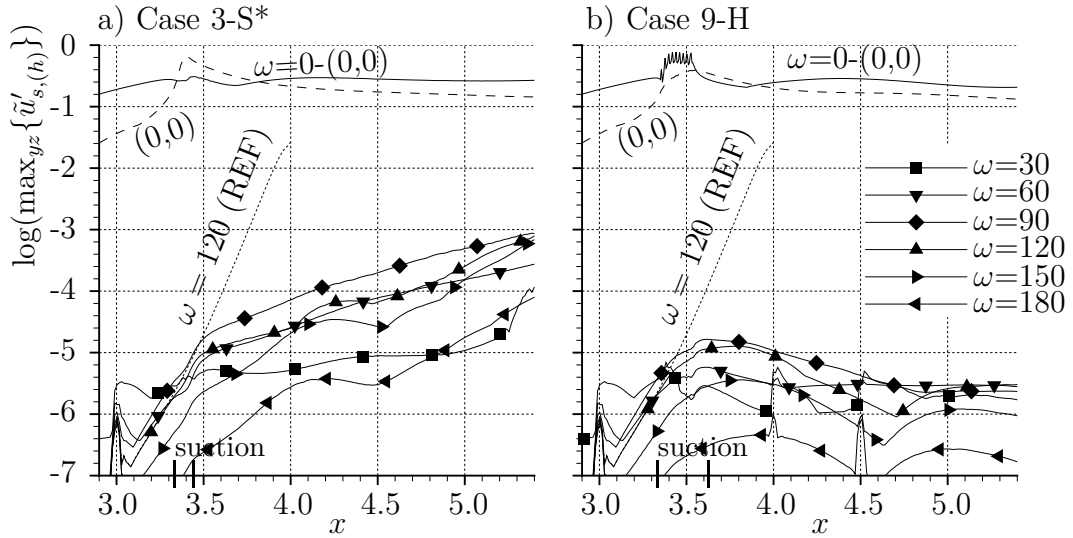


Figure 5.6: Like figure 5.3 but for cases 3-S* and 9-H.

massive attenuation of secondary growth and transition is shifted outside the domain considered. Also, $\omega = 0 - (0,0)$ does not exceed 30% amplitude. Only weak secondary growth can be found with the highest amplitudes reached by mode $\omega = 90$.

Finally, the corresponding pinpoint-suction case is set-up: Nine consecutive holes are arranged on a straight line parallel to the vortex-core orientation at $x = 3.36$, employing $c_q = 3 \cdot c_{q,0}$. Secondary growth and thus transition to turbulence is eliminated completely, see figure 5.6b. The downstream regrowth of the CFV pulled to the wall is apparently too small to provoke secondary instability inside the considered domain. In order to enable the formation of possibly new instability modes, the disturbance pulse from $x = 3.0$ is repeated at $x = 4.0$ and $x = 4.5$ and can be found in the local increase of e.g. mode $\omega = 180$. No palpable secondary growth is however observed throughout all modes.

Figure 5.7 provides a comparison of the transition delay for all cases. The amplitude level of $\tilde{u}'_s = 10^{-2}$ of the largest unsteady mode is used to measure the (relative) transition shift. Case 1-H is almost as efficient as case 3-S although c_q is three times smaller. The chordwise concentration from 3 slits to 1 slit results in a 17% improvement comparing cases 3-S and 1-S. Case 3-H shows a 50% larger transition delay compared to case 3-S at identical suction rates. For cases 3-S* and 9-H onset of transition cannot be detected in the

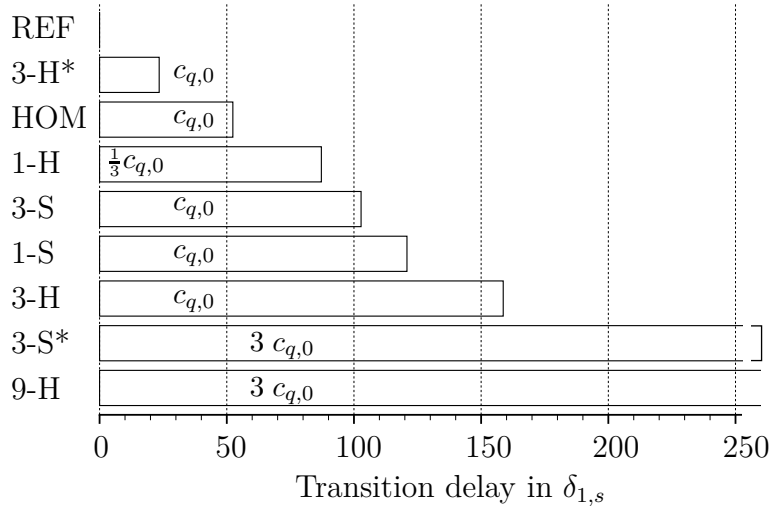


Figure 5.7: Transition delay of all cases including respective suction coefficient. Downstream locations are detected by where the first unsteady mode reaches a \tilde{u}_s -amplitude of 10^{-2} . Reference displacement thickness of the undisturbed base flow: $\delta_{1,s}(x = 4.00) = 7.73 \cdot 10^{-3}$.

considered domain. However, considering the growth rates at the end of the integration domain for case 3-S* it is expected that in this case transition will still occur.

5.3 Skin friction development

Figure 5.8 shows the parameter $C(x) = \int \max_t \{ \partial u_{42.5^\circ} / \partial y |_{y=0} \} dx$. The wall-normal gradient of the spanwise mean flow in flight direction $\partial u_{42.5^\circ} / \partial y |_{y=0}$ is proportional to the directional local skin friction coefficient. In order to account for fully turbulent flow the maximum value within one fundamental period in time ($t \in [0; T_0]$) is taken from our simulation with pulsed disturbances. The integral $C(x)$ allows for direct comparison of the curves at chordwise locations as a measure for the friction drag share up to this position. The reference case reveals laminar flow up to $x = 4.0$. The change in slope indicates transition to turbulent flow. Case 1-H shows the skin-friction increase caused by suction, pulling high-momentum fluid to the wall, at $x = 3.36$. However, at $x = 4.2$ the increase is compensated by sustaining laminar flow and less skin friction can be found throughout the integration domain in spite of turbulent flow starting at $x = 5.0$.

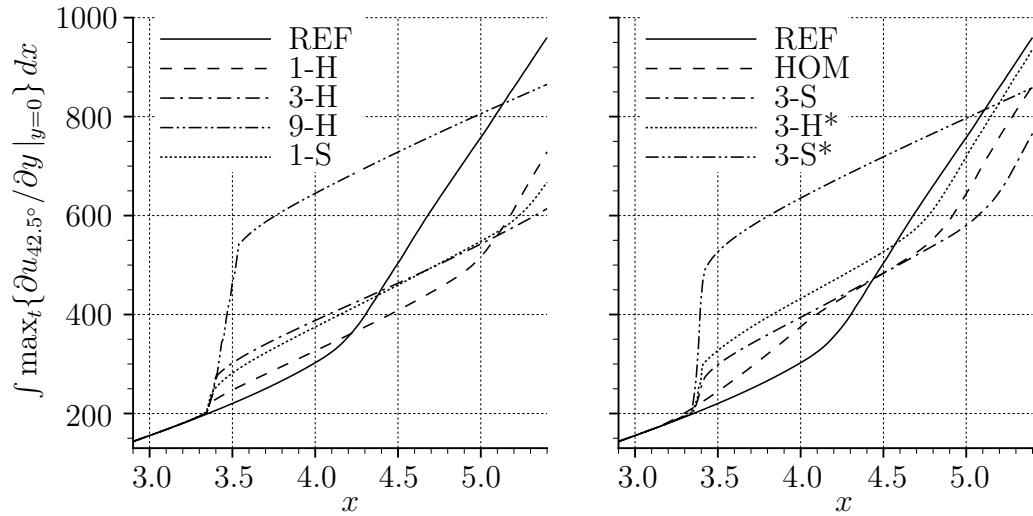


Figure 5.8: Downstream development of the (in streamwise direction) integrated wall-normal velocity gradient of the spanwise mean velocity component in direction of the oncoming flow ($\phi_\infty = 42.5^\circ$) at the wall serving as a measure of the skin friction coefficient c_f . For the integration the maximum over one fundamental period in time T_0 has been used in order to account for a fully turbulent flow (and not pulsed transition).

For case 3-H the approximately three times higher increase occurring at $x = 3.5$ arises from the three consecutive holes and thus three times larger mass flow sucked. However, for $x > 5.1$ this case causes less friction drag than case 1-H. Case 1-S* lies in between cases 1-H and 3-H. Case 9-H shows an enormous increase around $x = 3.5$ but the flow stays laminar so long that it will eventually outperform all other cases which is in turn true for case 3-S*. Cases HOM, 3-S, and 3-H* provide similar results as case 1-H with different locations of transition to turbulence. Note that further effects like the influence of the suction on the pressure distribution (sink effect) or the power possibly required for the suction system have not been taken into account in this evaluation. (Suction without additional pumps is currently investigated in practice. In this case the suction areas are connected to regions of low pressure at an aircraft.)

5.4 Vortical structures

Figures 5.9 and 5.10 show visualizations of vortical structures for all cases in a rotated reference system (cf. appendix D); for close-ups, marked by black rectangles, see figures 5.11 and 5.12. The angle $\phi_r = 45.0^\circ$ has been chosen to approximately straighten the CFVs in the visualization. The snapshot for case REF shows nearly undisturbed flow up to $x_r = 1.3$. The small structures at $x_r = 0.8$ show the disturbance pulse in an early stage. The turbulent region between $x_r = 1.5$ and $x_r = 2.0$ is caused by the previous pulse.

For case 3-H the suction holes are marked by black circles. A counter-rotating vortex pair developing behind the suction orifices is expected such that each vortex “transports” fluid into the hole. Looking downstream, the vortex emerging to the right turns counter-clockwise, i.e. close to the wall against the crossflow direction, and thus dies out soon in this case and cannot be discerned [56]. The one emerging to the left (structure I) turns in clockwise direction like the oncoming CFV, is shifted to the left and suppressed by the next CFV to the left shortly before merging with it. The oncoming CFV persists and is marginally shifted in positive spanwise direction. The secondary structures from the pulsing are on much lower amplitude levels compared to case REF.

Case 3-S shows local dislocation to the left and deformation of the oncoming CFV above the suction slits, marked by black lines, but the spanwise location downstream is not altered at all. (The local, opposite dislocation at the beginning and end of suction might be caused by the oblique slit orientation with respect to the CFV axis.) Secondary structures are more pronounced than in case 3-H.

Case 3-H* with pessimal suction-hole locations shows strong deformation of the primary vortices and only marginal transition delay.

Case 9-H shows strong downstream effects of the nine consecutive suction holes and a strong positive spanwise shift of the oncoming CFVs. Similar to case 3-H the left co-rotating vortex emerging from the suction holes can be clearly seen (structure II), this time almost merging with the CFV. The counter-rotating, right suction vortex (structure III) does not die out soon but is strong enough to push the oncoming CFV to the right before it is swallowed

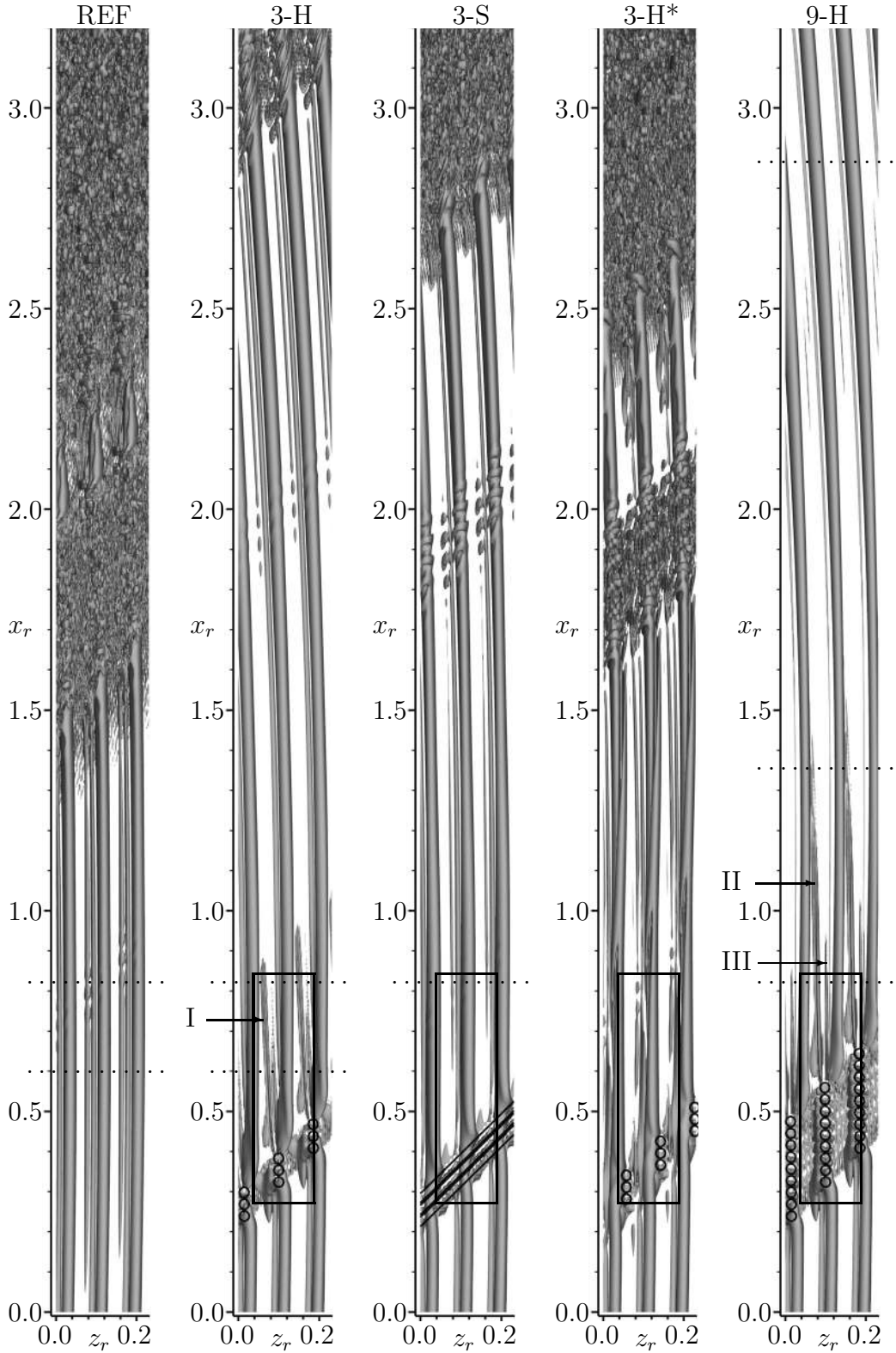


Figure 5.9: Vortex visualization ($\lambda_2 = -1$), top view, snapshot in time ($t/T_0 = 0.0$), to scale. A rotated reference system is used with $x_{r0} = 3.2$, $z_{r0} = 0.0$, $\Phi_r = 45.0^\circ$. Dotted lines refer to crosscuts of figures 5.13, 5.14, 5.15, and 5.18. Approximately 3 fundamental spanwise wavelengths are shown.

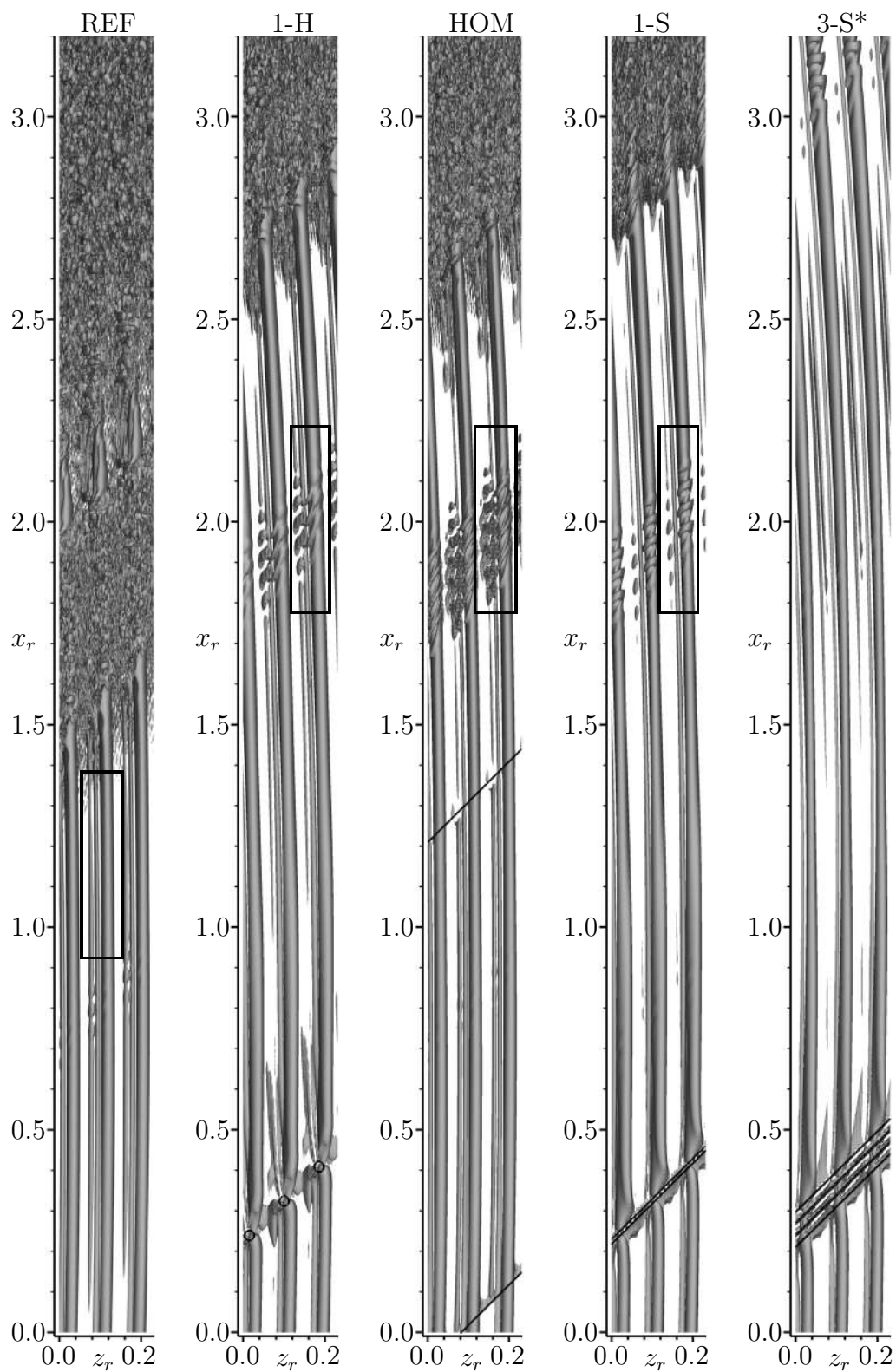


Figure 5.10: As figure 5.9.

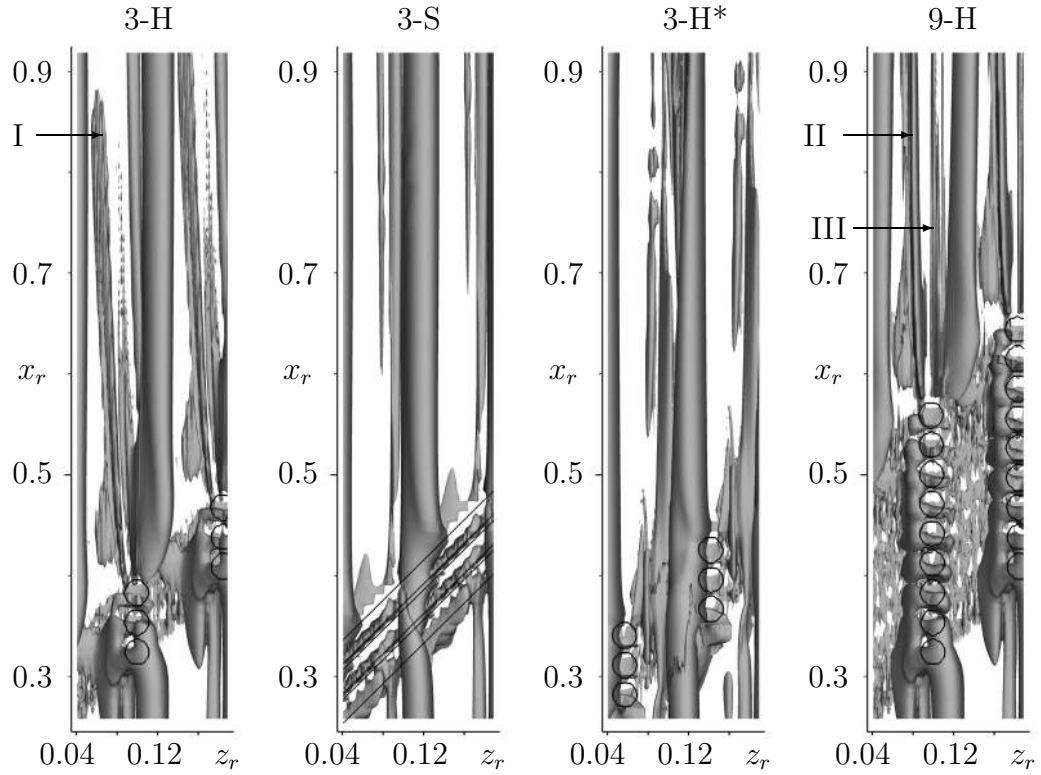


Figure 5.11: Close-ups from figure 5.9.

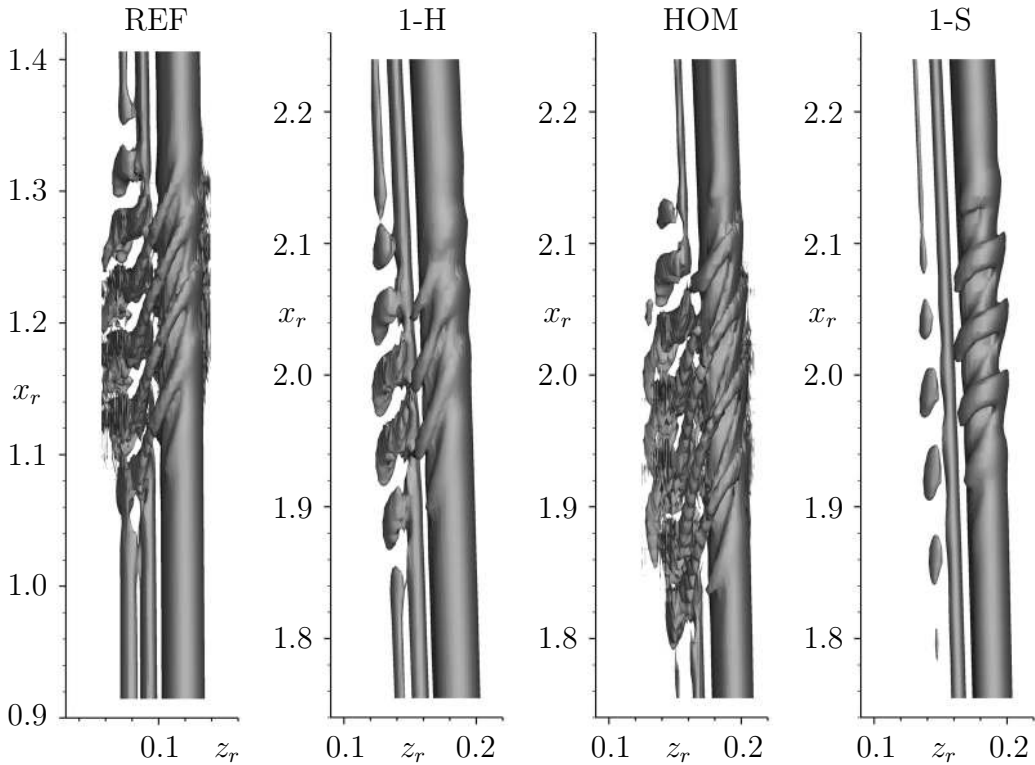


Figure 5.12: Close-ups from figure 5.10. Note the deviating streamwise section shown for case *REF* since $t/T_0 = 0.4$ is selected here.

by the crossflow. No structures from the pulse are visible in the considered domain.

Note that in case 9-H turbulence does not occur near $x \approx 5.5$ ($x_r \approx 3.3$) as discussed for case REF before, in the latter caused by amplification of numerical background noise. In case 9-H secondary instability is absent, and unsteady disturbances do not grow, or grow very weakly only.

Cases 1-H, HOM, and 1-S show less pronounced secondary structures compared to case REF and transition delay can be found. Secondary structures starting at $x = 2.9$ for case 3-S* indicate early stages of turbulence which was not observed in case 9-H.

Figure 5.12 gives a comparison of the secondary structures for cases REF, HOM, 1-H, and 1-S by means of close-ups of the respective downstream locations. Note that for case REF the close-up is not directly extracted from figure 5.10 but a snapshot at $t/T_0 = 0.4$ has been chosen to show the typically shaped finger-like vortices and thus the downstream domain shown is also different. The effect of homogeneous suction on the shape of the instability modes is negligible since the secondary structures look very much alike. For case 1-H the structures are less pronounced but the angle of the finger vortices is similar to the reference case. The structures of the case with slit suction differ from the other three cases: They seem to sit on top of the vortex and are more symmetrical than the ones before that are located exclusively at the updraft side of the vortex.

5.5 Secondary instability

5.5.1 Eigenfunctions in crosscuts

The influence of suction on the u_r -amplitude distribution of secondarily unstable eigenmodes becomes evident in figure 5.13. For case REF, the low-frequency mode $\omega = 30$ of type III can be found below the main vortex connected to the local maximum spanwise gradient, whereas the high-frequency mode $\omega = 120$ is connected to the local minimum and hence a type-I or z -

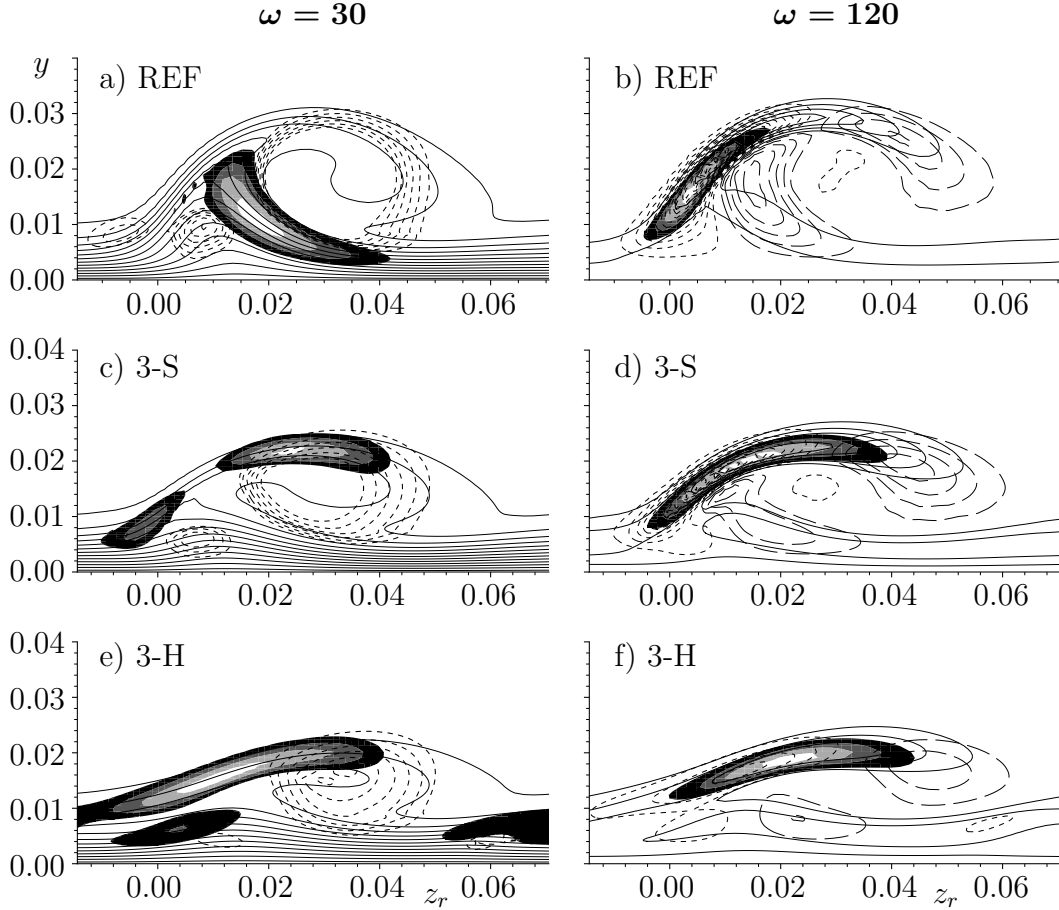


Figure 5.13: Crosscuts at $x_r = 0.82$ ($x \approx 3.78$). Left column ($\omega = 30$) shows \tilde{u}_r -isocontours (lines, 0.05 to 0.95, $\Delta = 0.075$), λ_2 -isocontours (dashed lines, -2 to -12, $\Delta = 2$) and the normalized u_r -amplitude distribution for mode $\omega = 30$ (shaded, levels 0.3 to 0.9, $\Delta = 0.2$). Right column ($\omega = 120$) shows $y \cdot (\frac{\partial u_r}{\partial z_r})/u_{b,s,e}$ -isocontours (solid lines, $\Delta = 0.2$, $\Delta = 0.4$ for case REF) and $y \cdot (\frac{\partial \tilde{u}_r}{\partial y})$ -isocontours (dotted: positive, dashed: negative values, zero-level not shown, $\Delta = 0.05$, $\Delta = 0.10$ for case REF) and normalized u_r -amplitudes for mode $\omega = 120$. The rotated reference system from figure 5.9 is used.

mode. The focus is on the z -mode since it has the largest amplification rates. Usually, its maximum is also connected to the maximum wall-normal gradient.

Figure 5.13b displays distributions of the spanwise and wall-normal gradients of the downstream velocity component \tilde{u}_r multiplied by the wall-normal coordinate y to downgrade near-wall maxima that are not relevant. At the maximum of the eigenfunction $u_{z,max} = y \cdot (\frac{\partial \tilde{u}_r}{\partial z_r}) / u_{b,s,e} = |-1.21|$ and $u_{y,max} = y \cdot (\frac{\partial \tilde{u}_r}{\partial y}) = 1.00$ is found. Case 3-S reveals a changeover to a y -mode, with $u_{z,max} = |-0.38|$ and $u_{y,max} = 1.12$ which confirms the more symmetrical shape of secondary structures found in figure 5.12. The spanwise mean suction reduces the overall spanwise shear by pulling the vortex towards the wall. For case 3-H $u_{z,max} = |-0.16|$ and $u_{y,max} = 0.77$ is found. The hole suction deforms the vortex such that the flow gradients are additionally reduced. The impact on the main vortex can be found when comparing the

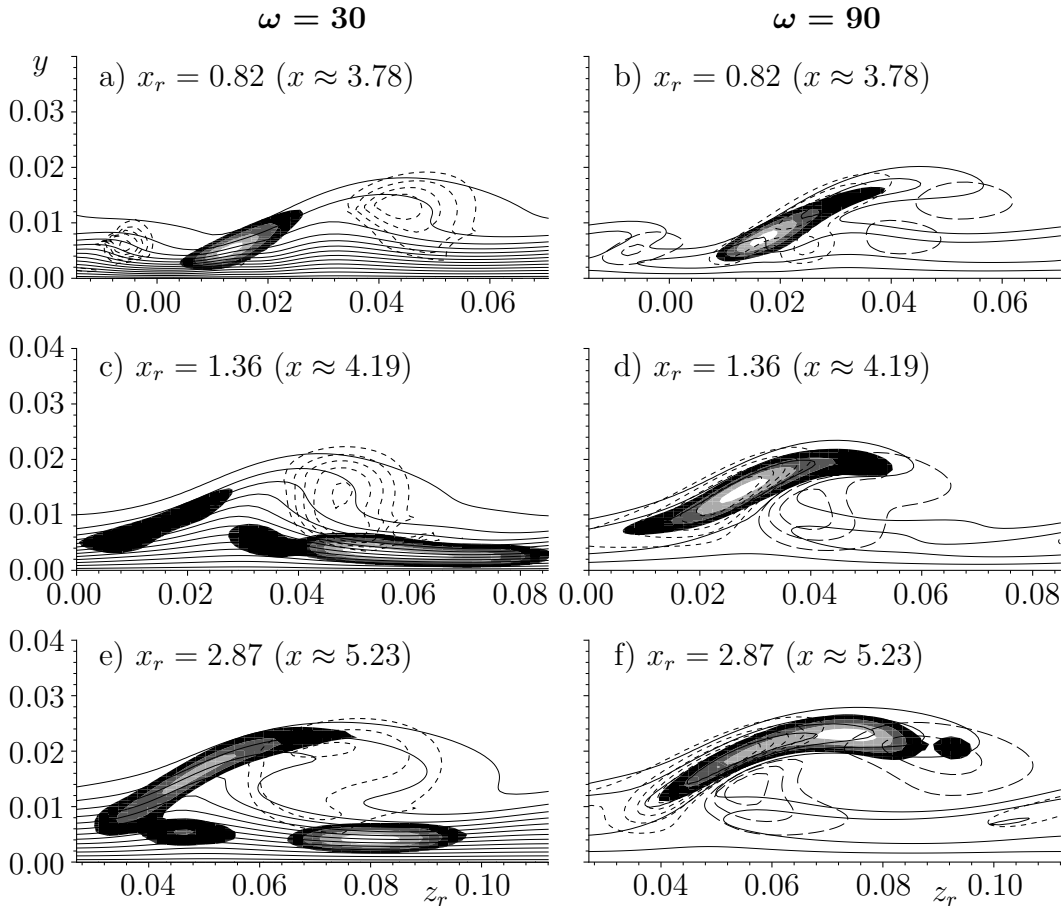


Figure 5.14: Crosscuts for case 9-H. Left column shows mode $\omega = 30$, right column mode $\omega = 90$. See figure 5.13 for details.

three λ_2 -distributions where case 3-H shows the weakest main vortex. If the value $\sqrt{u_z^2 + u_y^2}|_{max}$ is compared for cases REF, 3-S, and 3-H the values 1.57, 1.18, 0.79, are found, indicating an overall shear reduction, suggesting a direct measure for secondary-growth attenuation. When comparing the amplification rates of mode $\omega = 120$ at $x = 3.78$ from figures 5.4a, 5.5a, it turns out that the growth rates for cases 3-S and 3-H are almost identical, with the amplitudes lower for case 3-H. In other similar cases not shown the secondary growth rates decrease with decreasing gradient, too.

An evaluation of case 9-H (figure 5.14) shows a similar trend. The frequency $\omega = 90$ is chosen instead of $\omega = 120$ as for figure 5.13 since it has the highest amplitude level. $\sqrt{u_z^2 + u_y^2}|_{max}$ yields the values 0.41, 0.82, and 0.71 at the three downstream positions shown. Using nine holes reduces the main-flow gradients further, but predicting secondary stability is difficult employing solely this criterion. The development of the low-frequency mode shows a non-amplified T-S like amplitude distribution since no distinguished spanwise gradients exist. The development of mode $\omega = 90$ tends to switch from a z -mode to a y -mode. All modes shown are damped or neutral.

5.5.2 Kelvin-Helmholtz shear

To find a measure for secondary amplification a procedure described by Bonfigli & Kloker [12] is followed. A shear-layer plane, oriented perpendicular to the axes of the secondary vortex structures, direction t , is obtained by artificially enlarging the respective u -, v -, and w -eigenmodes and visual inspection of the corresponding secondary λ_2 -structures. t is roughly, but essentially not exactly, the direction of the CFV axis. Figure 5.15 shows the vorticity component $\omega_{x,t}$ perpendicular to the Kelvin-Helmholtz (K-H) shear-layer plane for four cases. The values found provide the expected information. Evaluating $\omega_{x,t}$ at the respective eigenfunction maxima delivers the following values for cases REF, 3-S, 3-H, and 9-H, respectively: 61.5, 40.0, 37.5, and 7.6. Evidently, lower K-H shear-layer strength yields smaller secondary amplification. For all cases, $\omega_{x,t}$ at the respective eigenfunction maximum is composed primarily of a combination of ω_y and $\omega_{z,r}$. For cases 3-S and 3-H, ω_y basically determined by $\partial u_r / \partial z_r$ is significantly reduced. Additionally, for case 3-H, the K-H plane

is tilted more relative to the plane perpendicular to the CFV axis ($\psi_t = 10^\circ$), and thus the contribution of ω_y is additionally decreased. Although the contribution of $\omega_{z,r}$ and thus $\partial u_r / \partial y$ to the $\omega_{x,t}$ -value is enhanced with increasing angle ϕ_t for cases 3-S and 3-H, this effect is overcompensated by the decreased wall-normal vorticity component. This causes a changeover from a z -mode (figure 5.15a) to a y -mode (figure 5.15c) comparing the respective location of the eigenfunction maximum in figure 5.15. The evaluation for case 9-H is added to show the virtually vanishing $\omega_{x,t}$ -component. The strongly altered orientation of the t -plane of a damped mode is of minor relevance. Also, a velocity component normal to the shear-layer in its plane further reduces the instability [12]. However, to gain reliable a-priori information on secondary instability properties, a two-dimensional eigenfunction solver, a comprehensive method using the PSE (parabolized stability equations), or DNS is required.

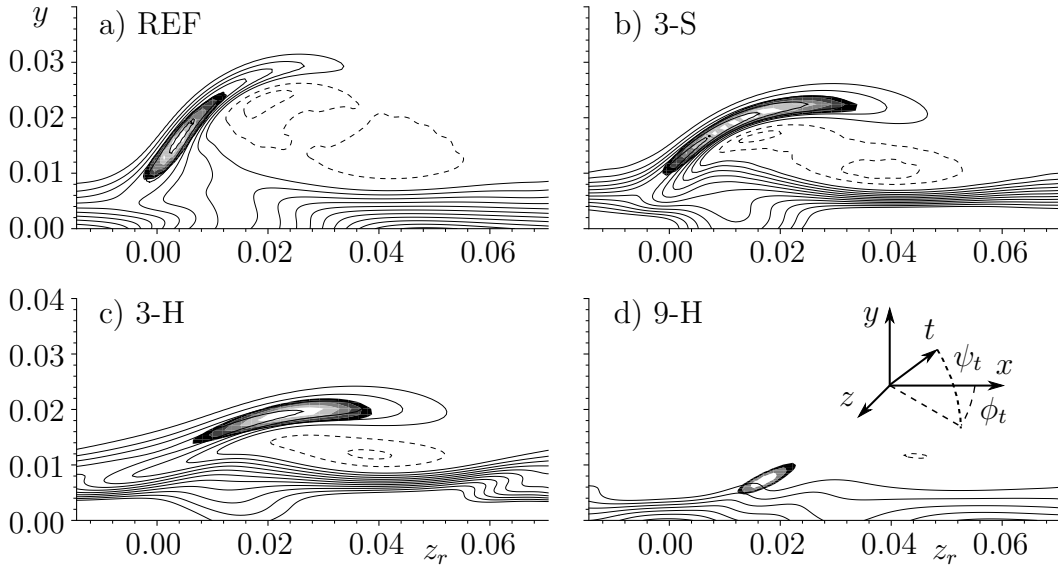
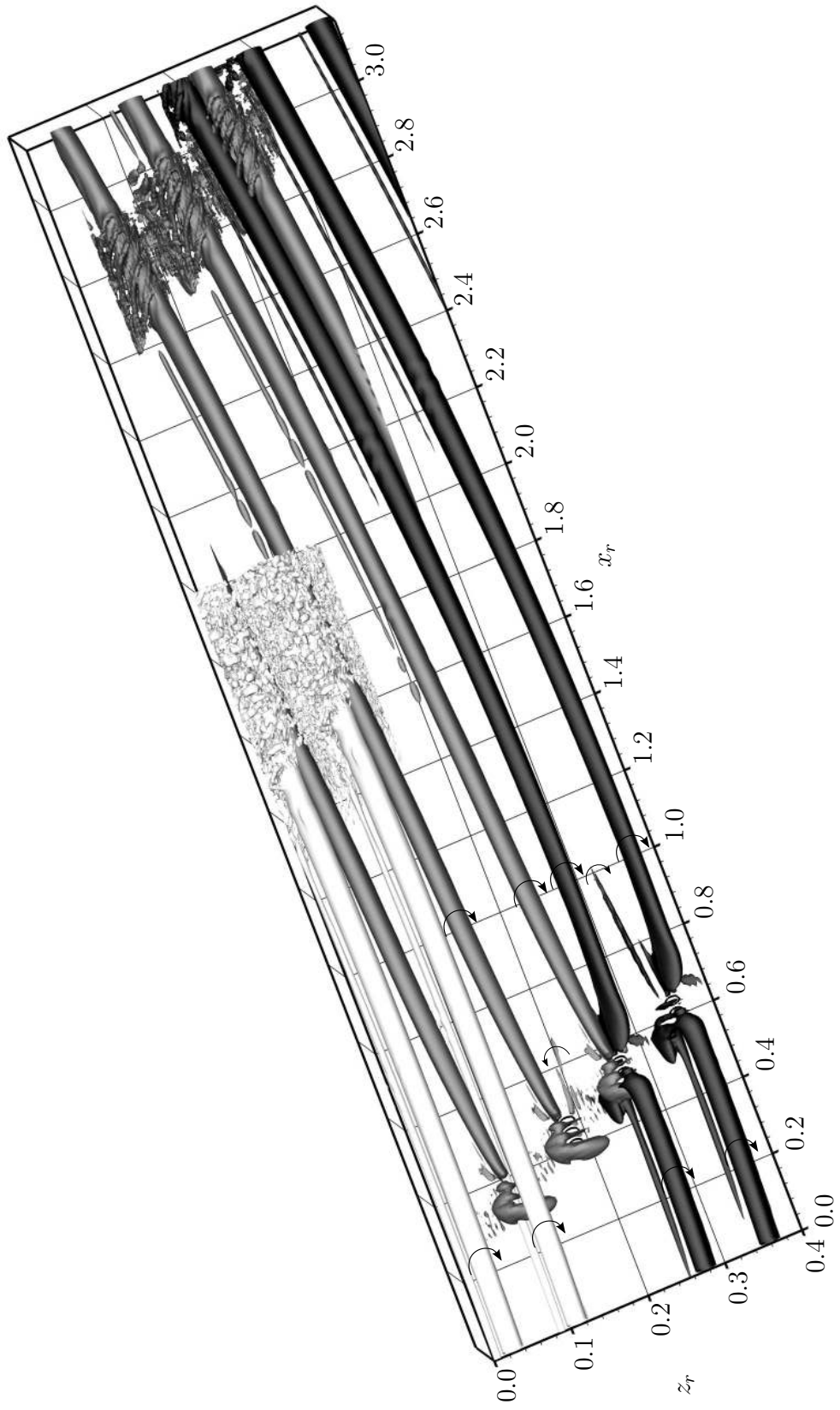


Figure 5.15: Crosscuts at $x_r = 0.82$ ($x \approx 3.78$). Vorticity component $\omega_{x,t}$ (lines, $\Delta = 10$, dashed negative values, zero-level not shown) and normalized u_r -amplitude distribution (shaded, levels 0.5 to 0.9, $\Delta = 0.1$) for mode $\omega = 120$ ($\omega = 90$ for case 9-H) a) REF, $\phi_t = 66^\circ$, $\psi_t = 15^\circ$, b) 3-S, $\phi_t = 91^\circ$, $\psi_t = 16^\circ$, c) 3-H, $\phi_t = 105^\circ$, $\psi_t = 10^\circ$, and d) 9-H, $\phi_t = 54^\circ$, $\psi_t = 7^\circ$. See the inset in d) for the definition of the direction t . Note that ϕ_t is measured in the chordwise system and $\phi_r \approx 45.0^\circ$ has to be subtracted in order to get the relative angle to the CFV axis direction. The rotated reference system from figure 5.9 is used.

Figure 5.16: Vortical structures ($\lambda_2 = -5$) for cases REF, 3-H, and 3-H-noCFV. The rotated reference system from figure 5.9 is used. Not to scale.

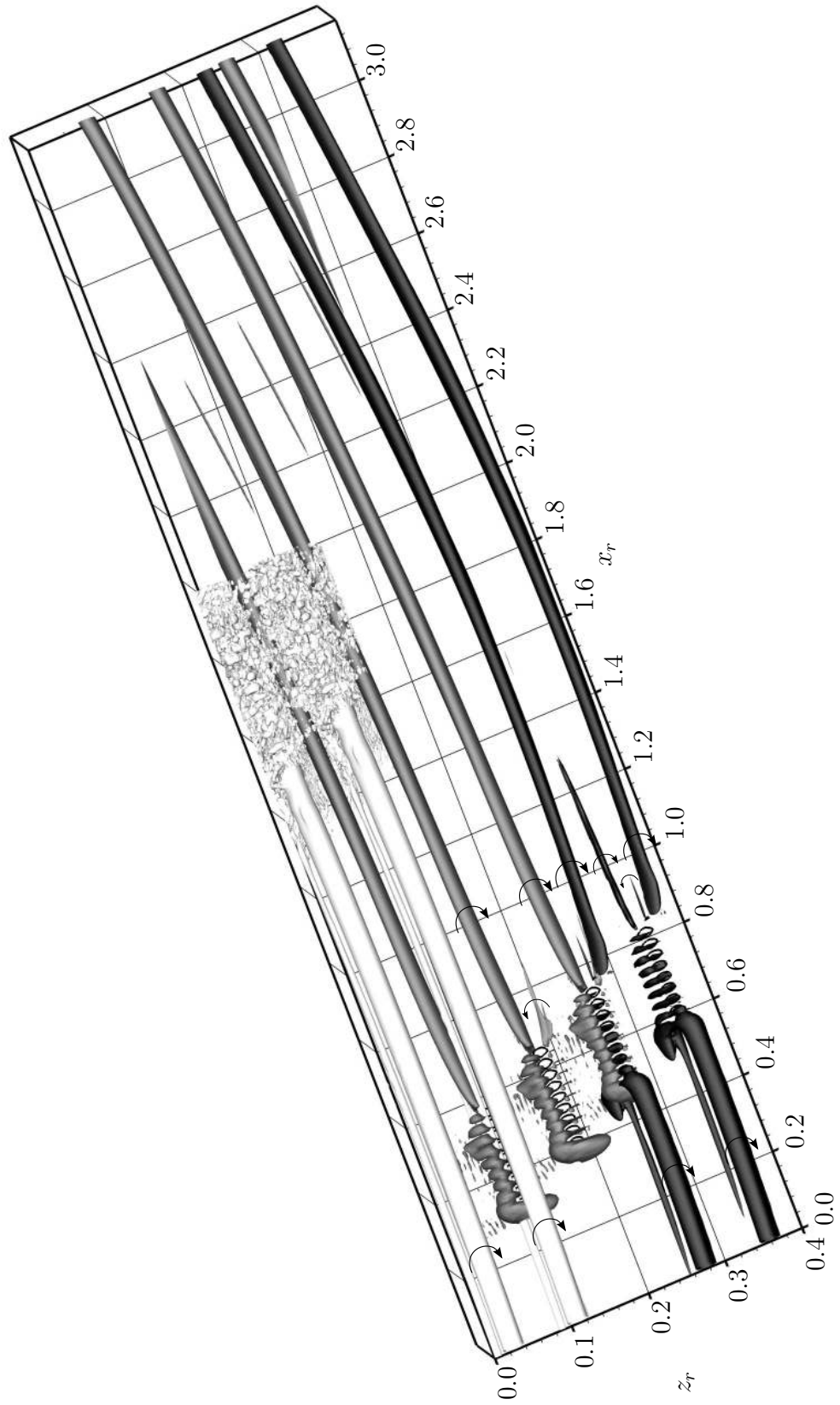


5.6 Analysis of crossflow-vortex interactions

To clarify the mechanisms occurring in the vicinity and downstream of the suction holes, the case, like case 3-H but without oncoming CFV, is considered 3-H-noCFV, *no oncoming CFV*, to identify the flow field induced by suction in the undisturbed base flow. To check for secondary instability the disturbance strip triggering the pulses is shifted from $x = 3.0$ to $x = 4.0$ and the initial disturbance amplitudes are increased by two orders of magnitude. Figure 5.16 shows vortical structures in three different shades of gray for cases REF, 3-H-noCFV, and 3-H to clarify the “nonlinear superposition”. For visualization, some regions are blanked. Furthermore, the sense of rotation is marked by arrows. The reference case REF (bright gray, two oncoming CFVs) shows early transition starting at $x_r = 1.40$. Case 3-H-noCFV (medium gray, no oncoming CFVs, three evolving main vortices) shows that only one vortex of the suction-induced counter-rotating vortex pair survives, eventually causing turbulence as well, starting at $x_r = 2.60$. The other one, turning against the crossflow is strongly damped and disappears instantly ($x_r = 0.60, z_r = 0.20$). The combination of oncoming and suction-hole induced vortex results in delayed transition (case 3-H, dark gray, two oncoming CFVs subject to hole suction). The CFV is sucked to the wall and reduced in size by the three suction holes located at the updraft side of the main vortex. Interestingly, the suction-hole induced vortex supported by the crossflow dies out soon in this case, probably hindered by the next main vortex ($x_r = 1.00, z_r = 0.32$).

A similar procedure is carried out for the case with nine suction holes. The initial amplitudes of the pulse are set back to the same level considered in case 9-H. The resulting flow field of the corresponding cases 9-H-noCFV and 9-H is visualized in figure 5.17. Slightly more pronounced structures directly behind the suction holes are found for case 9-H-noCFV due to the increased mass flux ($x_r = 0.70, z_r = 0.20$). The emerging and prevailing main vortex however is weaker than for case 3-H-noCFV, most likely due to the larger (stabilizing) mean flow deformation. Moreover, no finger vortices can be observed! The small vortex in case 9-H emanating from the last suction hole and turning against the crossflow (referred to as structure III during discussion of figure 5.9) can also be observed at this λ_2 -level ($x_r = 0.90, z_r = 0.36$). The one

Figure 5.17: Vortical structures ($\lambda_2 = -5$) for cases REF, 9-H, and 9-H-noCFV. The rotated reference system from figure 5.9 is used. Not to scale.



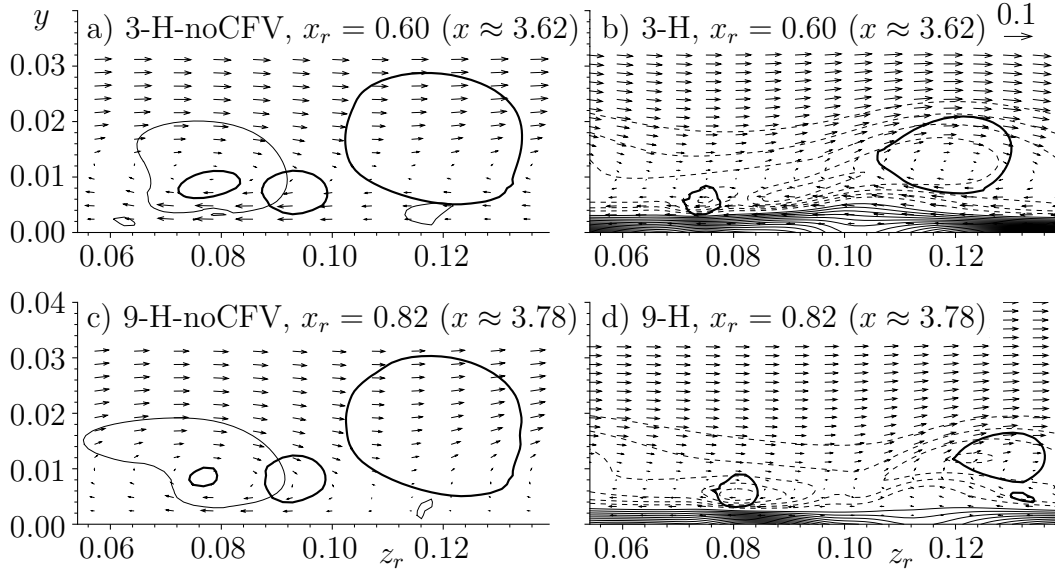


Figure 5.18: Crosscuts: a) and c) show isocontours with $\lambda_2 = -2$ (thin lines, case REF added with thick lines) and $[\tilde{w}_r, \tilde{v}]$ -vectors, b) and d) show $\tilde{\omega}_{x,r}$ -isocontours (lines, $\Delta = 2$, dotted negative values, zero-level not shown). The rotated reference system from figure 5.9 is used.

turning with the crossflow is more pronounced ($x_r = 0.8 - 1.3, z_r = 0.34$, structure II in figure 5.9) and is the result of the oncoming CFV and the suction-hole induced one. Partly, the angular momentum input of the suction holes is obviously consumed to weaken the oncoming vortex.

The crosscuts considered in figure 5.18a show λ_2 -isocontours in the plane $x_r = 0.600$ of figure 5.16 for case REF (thick lines) and case 3-H-noCFV (thin lines). The CFV center can be found at $z_r = 0.117$, the center of the co-rotating left suction-induced vortex at $z_r = 0.078$. Figure 5.18b shows the same crosscut for case 3-H. (Note that the corresponding dark gray structure in figure 5.16 is blanked there. Due to spanwise periodicity an identical structure can be found at $x_r = 0.80, z_r = 0.28$). The persisting main vortex sits at $z_r = 0.120$, is much weaker, and the co-rotating suction-hole induced structure can be found at $z_r = 0.074$. The negative values of $\tilde{\omega}_{x,r}$ confirm the sense of rotation.

Crosscuts for case 9-H are taken from figure 5.17 at $x_r = 0.824$. Figure 5.18c provides results for case REF and case 9-H-noCFV showing the respective spanwise vortex locations. Figure 5.18d reveals the already observed positive

spanwise shift of the CFV. (Again, the corresponding structure is blanked in figure 5.17 but can be found at $x_r = 1.23, z_r = 0.29$.)

The downstream development of steady and unsteady disturbances for cases 3-H-noCFV and 9-H-noCFV is compared with case REF in figures 5.19 and 5.20. Also, steady modes for cases 3-H and 9-H are added for comparison. As for case 3-H-noCFV the steady three-dimensional deformation of the flow field $\omega = 0 - (0, 0)$ shows the localized increase caused by the suction holes between $x = 3.3$ and $x = 3.4$ followed by amplified vortex growth beginning at $x = 4.1$. The amplitude level is at 20% and secondary instability, triggered at $x = 4.0$, sets in immediately, cf. figure 5.20 (dashed lines). Note that the mean-flow deformation $(0,0)$ drops below 13% at $x = 4.1$.

When the development of steady disturbances for case 9-H-noCFV is considered, the perturbation input by the nine suction holes is on a much higher level, but relevant vortex growth cannot be observed. The mean-flow deformations $(0,0)$ for cases 9-H and 9-H-noCFV are found to be well above 20% and do not drop below 16% for a long downstream distance (up to $x = 5.0$). Especially in the region of neutral CFV development (case 9-H-noCFV, $x \approx 4.1$) and readopted CFV growth (case 9-H, up to $x = 4.4$) the stabilizing influence persists. Secondary instability does not set in abruptly for case 9-H-noCFV although the pulse is triggered at several succeeding disturbance strips, cf. figure 5.20 (dash-dotted lines). Weak, but decreasing growth of secondary instability is observed (e.g. mode $\omega = 90$) when proceeding downstream. The growth of modes with higher frequency, e.g. $\omega = 180$, is completely non-linear. Note that self-induced unsteadiness (cf. the discussion regarding oversuction in sections 4.3 and 5.2), possibly triggered by the 9 holes, is not observed.

The effect of pinpoint suction becomes obvious by the following considerations: The reference case leads to transition to turbulence caused by a large-amplitude CFV and active secondary instability. The CFV develops from the controlled excitation of one of the most unstable spanwise modes. The same holds for case 3-H-noCFV ($c_q = 1.6 \cdot 10^{-3}$ considering a chordwise reference length of $l_x = 40 \delta_{99,s}$), where no oncoming CFV is present but the spanwise distance of the suction holes triggers the most unstable spanwise mode as well and the stabilizing effect of the mean-flow deformation is too weak to hinder its development and growth. Note that the secondary growth rates however

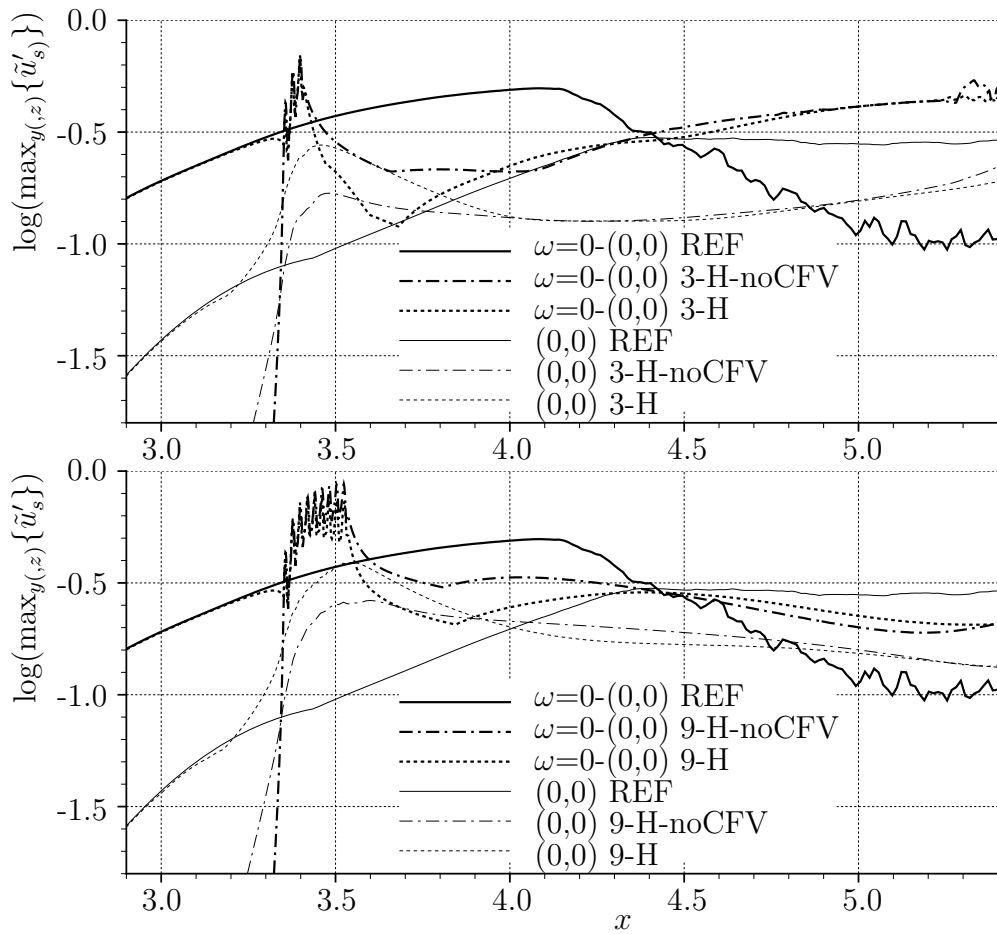


Figure 5.19: Downstream development of selected steady modal \tilde{u}'_s -amplitudes for cases REF, 3-H-noCFV, and 9-H-noCFV.

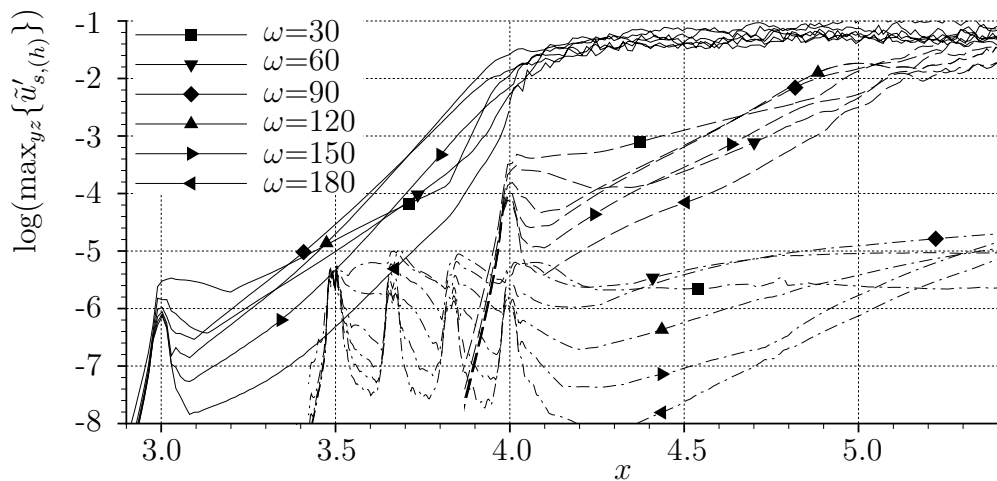


Figure 5.20: As figure 5.19 but unsteady modes are shown for cases REF (solid lines), 3-H-noCFV (dashed lines), and 9-H-noCFV (dash-dotted lines).

are smaller compared to case REF. The superposition of both cases (case 3-H, figure 5.4a) resulted in a more stable flow scenario, with less secondary amplification, revealing and proving the three-dimensional nature of pinpoint suction.

If nine suction holes are used ($c_q = 4.8 \cdot 10^{-3}$), the mean-flow deformation is almost strong enough to suppress the onset of secondary instability (case 9-H-noCFV). Since case 9-H results in completely eliminated secondary growth (figure 5.6b), it is clear that the designed non-linear interaction of CFV is beneficial. The purely two-dimensional effect of suction was provided with case 3-S* where the same sucked mass flux was applied through spanwise slits (without the pinpoint effect) but weak, continuously constant secondary amplification was found (figure 5.6a).

6 Conclusions

The effects of localized, concentrated suction at the wall on the secondary instability of a laminar, crossflow-dominated boundary-layer flow deformed by grown steady crossflow vortices (CFVs) have been investigated by direct numerical simulations. The underlying laminar base flow represents the 3-d boundary layer of the DLR Göttingen “Prinzipexperiment” where a flat plate with a displacement body above was employed to reproduce the flow in the leading-edge region over an infinite swept wing. The spatial evolution of forced disturbances including various kinds of suction setups has been simulated by numerically solving the compressible and incompressible three-dimensional unsteady Navier-Stokes equations. The aim was to delay laminar-turbulent transition in order to reduce viscous drag.

In the first part of the work, the usefulness of hole-suction modeling has been checked by comparing results from simulations with modeled and simulated hole suction in two- and three-dimensional boundary layers. The second part of the work provides results from various suction cases. Subject of investigation was the control of grown CFVs with active, strong secondary instability. The successful application of concentrated “pinpoint” suction could be shown resulting in significant transition delay.

Modeled suction versus simulated suction

Modeled and simulated suction has been compared for a $Ma=0.5$ Blasius base flow as well as a 3-d boundary-layer flow at $Ma=0.7$, the latter with large-amplitude CFVs, using one spanwise row of suction holes. The cases with simulated suction comprise a cylindrical channel domain below the plate and thus the interaction of the channel with the oncoming flow. As for the modeled cases, a wall-normal mass flux is prescribed at the wall such that the integrally sucked mass flux is the same as in the cases with suction channel.

Largely matching results, including quantitative flow-field visualization and comparison of vortical structures and velocity distributions as well as Fourier analyses in time, justify well the application of the chosen hole-suction modeling. In the $Ma=0.5$ flow, the generation and development of a suction-induced vortex pair turned out to be identical if the same sucked mass flux was considered for the simulated and the modeled case. As for the 3-d boundary layer, the weakening of the oncoming CFV is identical when the simulated or modeled suction orifice is placed beneath the updraft side of the CFV. The resulting attenuation of secondary-instability modes shows very good agreement.

Investigations considering critical Reynolds numbers with respect to over-suction revealed that at the chosen pressure levels at the channel outlet the flow in the channel adjusted well below critical values, yielding $Re_d = 970$ and $Re_{kk} = 350$ (where $Re_{d,crit} = 2300$ and $Re_{kk,crit} > 700$ [58] are the respective critical Reynolds numbers).

Laminar flow control by means of pinpoint suction

Motivated by the agreement found the main results for laminar flow control have been obtained from the numerically much more efficient incompressible method where the results in the “Prinzipexperiment” base flow are obtained by means of various kinds of modeled slit- and hole-suction setups. To date boundary-layer suction has been applied to reduce the primary crossflow instability. Here, however, it is shown that fully three-dimensional boundary layers with grown CFVs can be controlled by suction as well. This method tackles then secondary instability.

Applying identical suction coefficients c_q it could be shown that homogeneous and slit suction setups with spanwise invariant suction orifices provide little and medium transition delay, respectively, whereas the case employing (three succeeding) pinpoint suction holes below the updraft side of a grown, steady CFV postpones transition significantly. A case with nine suction holes, placed one after the other along the CFV, shows complete suppression of secondary instability. The corresponding two-dimensional scenario with suction slits performs well but not as good.

For the specific action of pinpoint suction three major effects could be elaborated:

First, the 2-d mean-flow deformation by suction weakens the development of a growing CFV mode or attenuates an already persisting one, at least to some extent, depending on its strength by pulling it towards the wall. Thereby, the vortices are flattened and spanwise shear is reduced. Furthermore, wall-normal shear is reduced as well since the distance of the shear-layer to the wall is diminished. This overall shear reduction leads to an attenuation of secondary instability. Considering flow scenarios without oncoming CFVs, it is shown that hole suction can trigger laminar-turbulent transition through the excitation of an unstable CFV mode in the presence of suction. If the sucked mass flux is increased, the mean-suction effect can however be strong enough to almost suppress the development of a critical CFV.

The second effect appears if concentrated, localized suction through holes is placed beneath the updraft side of the oncoming CFV. In the clean flow scenario without oncoming CFV, a pair of counter-rotating vortices emanating from each suction hole is induced. The one turning against the crossflow is suppressed shortly downstream of the hole. The other one develops and rotates like a growing, amplified CFV. In the combined scenario, i.e. oncoming CFVs plus hole suction, the suppressed suction-induced one can still push the oncoming main vortex to the side where it is hampered by the large co-rotating suction-induced one from the other side due to its closeness. Soon after, both suction-induced vortices disappear. The result is CFVs with less vortical momentum and attenuated secondary amplification. (It has to be pointed out that this effect differs largely from mechanisms found in two-dimensional symmetrical base flows where excited vortices can be canceled, e.g. on a suction panel, by designing a staggered panel and thus exciting anti-phase, i.e. counter-rotating, vortices.)

Third, high-frequency instability modes are directly influenced by the localized suction if placed beneath the location of their maximal amplitude. Considering a case with homogeneous suction, little influence of the suction on the main vortex can be observed whereas the secondary growth rates are noticeably attenuated. Also, a simulation with weak blowing at the very same location (not shown) shows frequency-dependent attenuation although the underlying

basic state becomes seemingly “more unstable” since the vortex is driven in this case. Thus, the secondary instability is sensitive to very small changes in the underlying velocity field. This effect has been detected by Bonfigli & Kloker [12] who found that a wall-normal velocity component superposed on the Kelvin-Helmholtz shear layer, in which secondary instability originates, reduces the disturbance growth.

The secondary, traveling modes present in cases with suction and developing on the updraft side of each CFV are oriented more parallel to the crossflow direction compared to a reference case without suction. If amplitude distributions are considered a changeover from the typical type-I (z -) mode to type-II (y -) modes is found, revealing a strong change of stability properties. The shear in the respective Kelvin-Helmholtz plane is found to be reduced as well, resulting in an overall significant reduction of secondary instability.

As for the suction holes, a diameter of about two times the displacement thickness and a suction velocity of about 20% of the local external velocity, averaged over the hole, has been chosen. Compared to standard suction this is a 2-3 times higher suction velocity than usual. Thus, pinpoint suction is still distinctly below very strong suction that might cause local flow tripping. (Own tentative DNS investigations on so-called oversuction caused by single holes indicate that, at the chosen parameters $Re_{\delta_{1,s}}$ and $d/\delta_{1,s}$, the critical suction velocity $\bar{v}_{avg}/\bar{u}_{b,s,e}$ lies beyond 45% [58].)

As for the wall shear caused by the concentrated suction, the observed increase is non-negligible but is far outweighed by the substantial transition delay. For practical applications of pinpoint suction either the position of the CFVs with respect to the suction holes has to be fixed - for example by using controllable actuators upstream -, or a panel with many holes, controllable in groups or even individually, can be used in conjunction with shear stress sensors. More simply, the slit version may be applied that however is less effective. Note that only few spanwise slits would be necessary for effective control.

A Numerical setup and computational performance

Table A.1 provides numerical simulation parameters for all incompressible cases discussed in chapter 5 and for the verification simulations mentioned in section 2.3. N_x , N_y , and N_z represent the number of grid points in stream-wise, wall-normal and spanwise direction, and $K + 1$ is the number of Fourier harmonics in z -direction. The wall-normal step sizes (Δy_{wall} and Δy_δ) are given at the wall and at $\delta_{99,s}$ at the location of the (first) suction orifice. The value $\Delta y_{wall}/\Delta y_e$ gives the relation between the wall-normal step size at the outer edge and the wall. The spanwise resolution is $\Delta z = \lambda_{z,0}/N_z$. The code is parallelized in spanwise direction, see e.g. [57].

Table A.2 summarizes parameters for all cases at $Ma=0.5$ and $Ma=0.7$ investigated in chapter 4. Domain decomposition in the $x - y$ -plane is applied for effective parallelization, see e.g. [5]. For the channel domains the grid points in radial direction r , in wall-normal direction h , and circumferential direction ϕ are referred to as N_r , N_h , and N_ϕ . Note that the channel domains comprise an equidistant wall-normal grid starting at $y = 0.0$ up to $y = -350\Delta y$ with subsequent grid stretching.

The most important parameters for the two simulations mentioned in the introduction (figure 1.3) are given in the following. The Blasius case is simulated with the incompressible numerical method at $Re = 100,000$, $Re_{\delta_{1,hole}} = 1924$, $d/\delta_1 = 2.0$, and $\lambda_{z,0}/d = 7.4$. An area-averaged mean suction velocity of 26% is chosen. The 3-d case is simulated with the compressible numerical method at $Re = 92,000$, $Ma_\infty = 0.2$, $Re_{\delta_{1,s,hole}} = 719$, $d/\delta_{1,s} = 3.6$, and $\lambda_{z,0}/d = 4.3$. The area-averaged mean suction velocity yields 24%. For further details on the setup of the DNS see [58], cases “1-1” and “3-1”.

All simulations were carried out on the vector computers provided by the

Case	REF/HOM		All discrete-suction cases		Verification		Verification	
	incompressible		incompressible		compressible	w/o suction	incompressible with suction	
Re	92000	92000	92000	92000	92000	92000	92000	92000
\bar{u}_∞ [m/s]	14.0	14.0	14.0	14.0	72.72	14.0	14.0	14.0
\bar{L} [m]	0.1	0.1	0.1	0.1	0.01923	0.1	0.1	0.1
Ma $_\infty$	0	0	0	0	0.21	0	0	0
$x \in$	[1.65, 5.85]	[1.65, 5.85]	[1.65, 5.85]	[1.65, 5.85]	[1.90, 4.28]	[1.65, 4.48]	[1.65, 4.48]	[1.65, 4.48]
$y \in$	[0.0, 0.135]	[0.0, 0.077]	[0.0, 0.077]	[0.0, 0.077]	[0.0, 0.077]	[0.0, 0.135]	[0.0, 0.077]	[0.0, 0.077]
$\lambda_{z,0}$	0.12	0.12	0.12	0.12	0.12	0.12	0.12	0.12
N_x	3202	3202	3202	3202	1816	2162	2162	2162
N_y	209	225	225	225	95	209	225	225
K / N_z	15 / (64)	15 / (64)	15 / (64)	15 / (64)	(10) / 32	10 / (32)	10 / (32)	10 / (32)
γ_0	52.4	52.4	52.4	52.4	52.4	52.4	52.4	52.4
$\Delta x \times 10^3$	1.31	1.31	1.31	1.31	1.31	1.31	1.31	1.31
$\Delta y_{wall} \times 10^5 / \frac{\Delta y_{wall}}{\Delta y_e}$	7.91 / 29.78	0.66 / 307.4	0.66 / 307.4	0.66 / 307.4	23.03 / 8.63	7.91 / 29.78	0.66 / 307.4	0.66 / 307.4
$\Delta y_\delta \times 10^5$	48.24	62.64	62.64	62.64	84.7	48.24	62.64	62.64
$\Delta z \times 10^3$	2.00	2.00	2.00	2.00	3.75	3.75	3.75	3.75
$\Delta t \times 10^4$	1.75	0.66	0.66	0.66	0.11	1.75	0.66	0.66

Table A.1: Simulation parameters for incompressible and verification cases (3-d base flow and modeled suction).

Case	Ma=0.5		Ma=0.7		reference case ^a modeled suction
	main domain	channel domain	main domain	channel domain	
Re	100,000	100,000	92,000	92,000	92,000
\bar{u}_∞ [m/s]	173.63	173.63	254.51	254.51	254.51
\bar{L} [m] $\times 10^3$	9.158	9.158	5.494	5.494	5.494
Ma _∞	0.5	0.5	0.7	0.7	0.7
$x \in (r \in)$	[11.66, 12.98]	[0.0, 0.0193]	[1.90, 4.28]	[0.0, 0.0084]	[1.90, 4.28]
$y \in (h \in)$	[0.0, 0.163]	[-0.62, 0.0]	[0.0, 0.079]	[-0.25, 0.0]	[0.0, 0.200]
$\lambda_{z,0}$	0.286	-	0.12	-	0.12
N_x (N_r)	1051	25	1818	20	1816
N_y (N_h)	105	1300	112	1000	112
K / N_z (K / N_ϕ)	(42) / 128	(42) / 128	(42) / 128	(42) / 128	(10) / 32
γ_0	22.0	-	52.4	-	52.4
$\Delta x \times 10^3$ ($\Delta r \times 10^3$)	1.26	0.786	1.31	0.433	1.31
$\Delta y_{wall} \times 10^5 / \frac{\Delta y_{wall}}{\Delta y_c}$	3.00 / 16.58	3.00 / 3.4	1.00 / 24.16	1.00 / 7.91	2.30 / 21.54
$\Delta y_\delta \times 10^4$	18.70	-	8.19	-	10.89
$\Delta z \times 10^4$	22.34	-	9.38	-	37.5
$\Delta t \times 10^4$	0.143	0.143	0.209	0.209	0.524

Table A.2: Simulation parameters for simulations at $Ma=0.5$ (**2-d base flow**) and $Ma=0.7$ (**3-d base flow**).

^aTwo additional simulations have been carried out on CRAY XE-6 with $x \in [1.9, 5.43]$ and $N_x = 2700$

HLRS (High Performance Computing Center) Stuttgart, namely on the NEC SX-8 and SX-9 computers. The incompressible code was run with the standard RK4-O4 time integrator for cases REF/HOM. 10 GB of memory were needed on one node SX-9 (16 vector CPUs @ 3.2 GHz) and each processor was operating at 11200 MFLOPs. The CPU time per grid point and time step was $0.09 \mu s$. For the semi-implicit time integrator, applied in all remaining incompressible cases with suction, the following values were found: 11 GB memory requirement, 9000 MFLOPs/CPU, and $0.18 \mu s$ CPU time per time step and grid point. Considering the actual physical problem, another important parameter is the relation of the “CPU time per spatial grid point and fundamental period” values since it compares the necessary integration time to reach a certain physical flow state. For the two considered setups the code with semi-implicit time integrator was slower by a factor of 5.1. This value includes the factor of 2 considering the required CPU time per time step and grid point and a factor of 2.5 resulting from a necessarily smaller time step due to the explicitly treated convective terms using a three-step Heun method.

The compressible verification simulation at $Ma=0.2$ was computed on 4 nodes SX-8 (each having 8 vector CPUs @ 2.0 GHz) where the internodal MPI parallelization extended over 4 domains in streamwise direction and intranodal OpenMP parallelization was applied for the spanwise direction. Operating at 5650 MFLOPs a CPU time per grid point of $2.4 \mu s$ was required. This correlates roughly to a value of $0.80 \mu s$ for a SX-9 CPU considering a reasonable average speedup SX-8-CPU to SX-9-CPU of 3. Comparing the required CPU time for a fundamental period in time to the corresponding incompressible verification simulation with suction and semi-implicit time integrator it turned out that the incompressible code was still more than 14 times faster (comparison on the NEC SX-9 system).

The compressible simulation at $Ma=0.7$ yields $0.60 \mu s$ SX-9 CPU time per grid point for the modeled-suction case and $1.90 \mu s$ for the case with suction channel included. For the suction channel, a much finer resolution in wall-normal and spanwise direction is furthermore required. Thus, comparing the corresponding integration times for a fundamental period in time, the channel simulation is slower by a factor of 9 per spatial grid point than the corresponding modeled case.

Last, a comparison of totally consumed CPU hours for some cases is given. Thereby, the required time for a certain problem is compared regardless of factors like numerical method or resolution. The final state for the $Ma=0.7$ channel simulation was obtained after 15 fundamental periods in time using a total of 11520 SX-9 CPU hours whereas the case with modeled suction consumed 322 CPU hours only. The incompressible suction cases provide almost twice the streamwise integration-domain length and required 768 hours for 15 fundamental periods in time. The consumption of the incompressible reference case was 99 CPU hours.

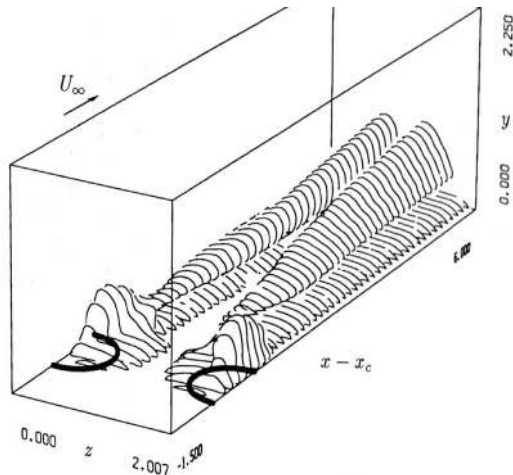
For comparison, some parameters for a simulation on the new CRAY XE-6, a massively-parallel supercomputer installed at the HLRS in 2012, are given: The $Ma=0.7$ case with modeled suction and identical simulation parameters as case MOD but $N_x = 2700$ required 39467 CPU hours on 1696 AMD Opteron(tm) 6276 (Interlagos) processors @ 2.3 GHz. Thereby, 27×3 domains were set up in streamwise and wall-normal direction, respectively (internodal parallelization using MPI), whereas the spanwise direction is parallelized using OpenMP (intranodal, one node has 32 CPUs). Note that in this case 15 periods in time turned out to be not sufficient for obtaining a quasi-periodic flow field and 35 periods were simulated which however might not be required. Thus, using the factor $35/15$ and considering N_x to be linearly dependent on the required CPU time giving another factor of $3/2$, the total CPU-hours have to be scaled down by a factor of 3.5 for a direct CPU-time comparison to the modeled-suction case on the SX-9. Still, a factor of about 35 remains that the CRAY XE-6 processors are slower than the SX-9 processors. Note that the domain decomposition and other parameters were not optimal. Typically a factor of 10-20 is expected.

B Grid studies for incompressible numerical method

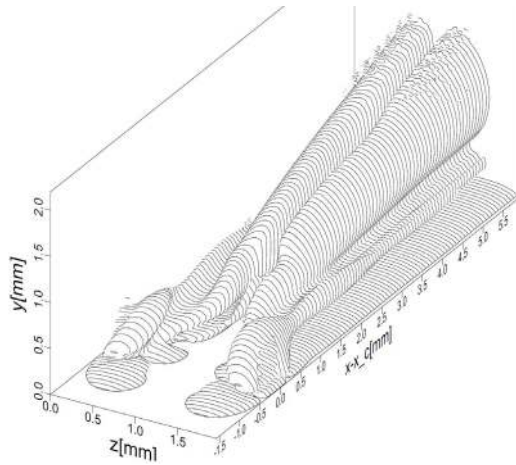
During the current work it turned out that the wall-normal resolution especially close to the wall is an extremely crucial parameter for a vorticity-based DNS code when non-weak wall suction is applied. Meitz [53] and Messing [55] provide DNS results for an experimental flow by Goldsmith [25], where streamwise vortices emanating from a spanwise row of suction holes with $\bar{v}_{max}/\bar{u}_\infty = 0.60$ were investigated. The case was considered “just subcritical”, and growing streamwise, contra-rotating vortices were observed (see figures B.1 a,b).

The case has been revisited to validate the current code version. The most important parameters for the simulation are: Reynolds number $Re = 100,000$, freestream velocity $U_\infty = 15.0m/s$, reference length $L = 0.1m$, location of the suction hole center $x_{hole} = 0.508m$, displacement thickness of the undisturbed base flow at the suction hole center $\delta_{1,hole} = 1.224 mm$, corresponding Reynolds number $Re_{\delta_{1,hole}} = 1224$, $d_{mod}/\lambda_{z,0} = 0.5$, where $d_{mod} = 1.03mm$ is the suction hole diameter. The \cos^3 -function (see equation 2.11) suggested by Meitz was used by Messing and has been used for the current cases as well to model the hole suction.

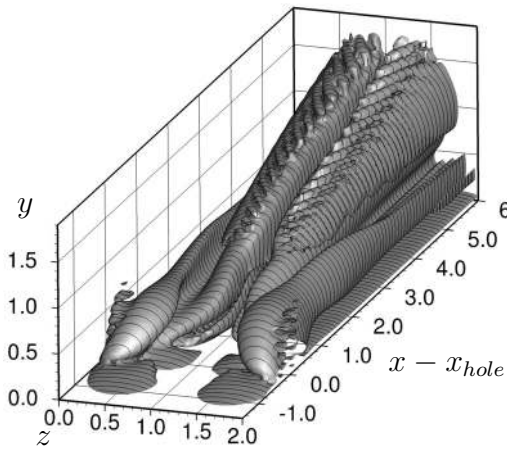
Successive refinement of Δy_{wall} results in decreasing strength and spanwise extension of vortical structures (see figures B.1 c-e). The result with the high-resolved grid “fine” shows two small, instantly damped co-rotating vortices. For case “coarse” it turned out that long-time integration is not possible for the selected parameters. The degree of unsteadiness is therefore dependent on the integration time level. (Note also that Messing labels his plot $|\omega_x| = 60$, but Meitz and own results show $|\omega_x| = 30$ – this might thus as well be a labeling error by Messing.)



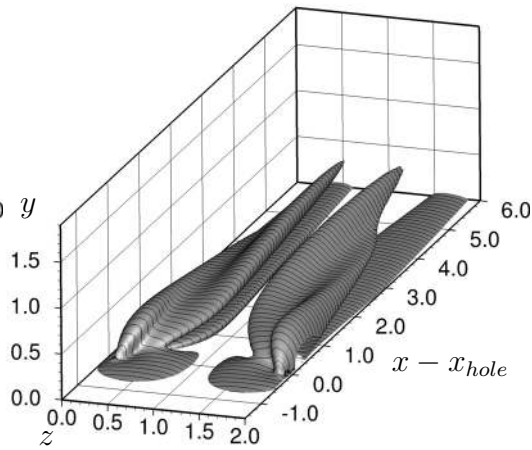
a) Result from Meitz [53]



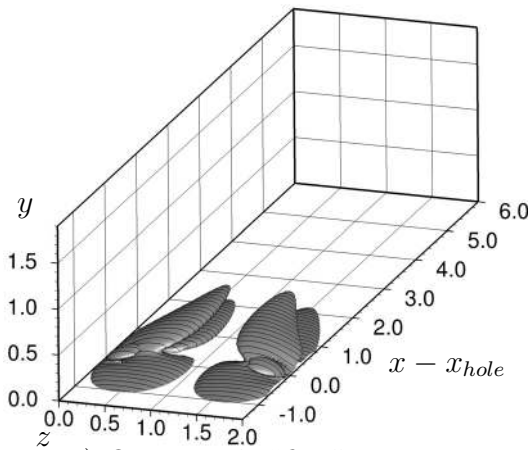
b) Result from Messing [55]



c) Own result "coarse"



d) Own result "medium"



e) Own result "fine"

a) $\Delta y = 7.5 \cdot 10^{-2} \text{ mm}$, $K=10$ b) $\Delta y = 5.0 \cdot 10^{-2} \text{ mm}$, $K=17$ c) $\Delta y = 5.0 \cdot 10^{-2} \text{ mm}$, $K=17$ d) $\Delta y = 6.3 \cdot 10^{-3} \text{ mm}$, $K=15$ e) $\Delta y = 4.7 \cdot 10^{-4} \text{ mm}$, $K=15$

a), c)-e): Stretched wall-normal grid

b): 3 wall-zones, successively halved Δy a)-e): $\Delta x = 7.5 \cdot 10^{-2} \text{ mm}$

Figure B.1: Results for Goldsmith suction case by Meitz, Messing, and own results. Shown are vortical structures marked by $|\omega_x| = 30$ - isosurfaces.

With respect to the boundary-layer thickness, Meitz employed $\Delta y_{wall}/\delta_{1,hole} = 1/16$, Messing used $1/24$ whereas the values for the current cases “medium” and “fine” are $1/200$ and $1/2600$. Only minor differences can be observed comparing the result from case “fine” to a case with $\Delta y_{wall}/\delta_{1,hole} = 1/1300$ but convergence has not been fully proofed.

Moreover, the semi-implicit time integration scheme introduced in section 2.1.2.4 has been verified during this grid study revealing identical results compared to a simulation with the standard RK4-O4 time integrator at the same wall-normal resolution.

B.1 Two-dimensional base flow

A thorough grid study is provided for two cases with $\bar{v}_{max}/\bar{u}_{\infty} = 0.30$ and 0.45 , respectively, employing the \cos^3 -suction distribution in a Blasius boundary layer, similar to the above-mentioned Goldsmith case.

Results for the 45%-suction case are shown in figure B.2 where the downstream development of selected disturbance amplitudes is traced for three wall-normal resolutions. Whereas a strong deviation is visible when $\Delta y_{wall}/\delta_1$ is decreased from $1/800$ to $1/1300$, no difference can be recognized when the finest resolution with $1/2600$ is considered. This result suggests that the above-mentioned case “fine” operating at 60% suction might not be fully converged assuming that the required wall-normal step size at the wall depends directly on the maximum suction amplitude. Note that at insufficient wall-normal resolution the generated vortex is overpredicted in amplitude which is in accordance with the various results provided in figure B.1. Refinement of the streamwise and spanwise resolution has absolutely no effect on the solution.

The same procedure is carried out for a case with 30% hole suction and results for $\Delta y_{wall}/\delta_1$ covering $1/400$, $1/800$, and $1/1300$ are provided in figure B.3 where a similar picture as above can be observed but this time converged results are found for the $1/1300$ -case.

The last study constitutes a quantitative comparison with results of the compressible code. It acts as a precursor for the final code verification presented in section 2.3 where results of a fully three-dimensional flow field in-

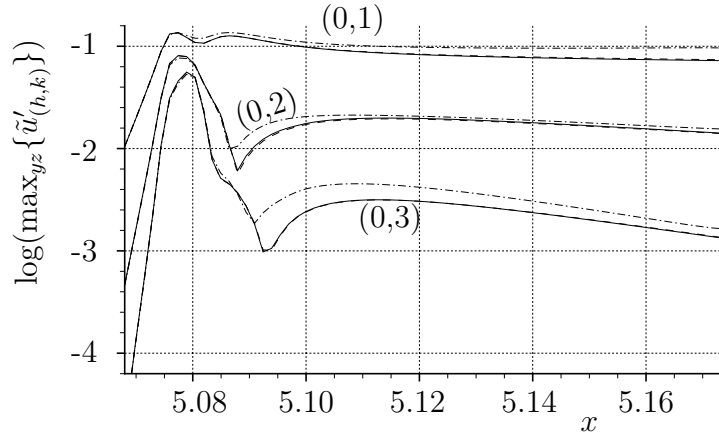


Figure B.2: Grid study of the wall-normal stretched grid for an incompressible case with 45% hole suction in a Blasius boundary layer. $\Delta y_{wall} = 1/2600 \delta_1$ (solid lines), $\Delta y_{wall} = 1/1300 \delta_1$ (dashed lines), and $\Delta y_{wall} = 1/800 \delta_1$ (dash-dotted lines). The downstream development for the steady modal $\tilde{u}'_{(h,k)}$ -amplitudes $(0,1)$, $(0,2)$, and $(0,3)$ is evaluated.

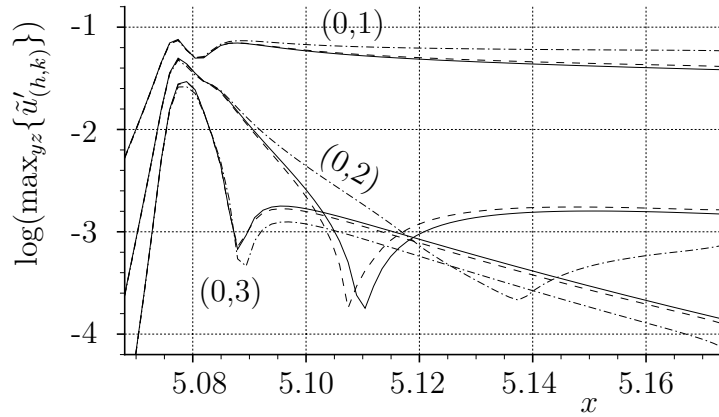


Figure B.3: As figure B.2 but with 30% hole suction. $\Delta y_{wall} = 1/1300 \delta_1$ (solid lines), $\Delta y_{wall} = 1/800 \delta_1$ (dashed lines), and $\Delta y_{wall} = 1/400 \delta_1$ (dash-dotted lines).

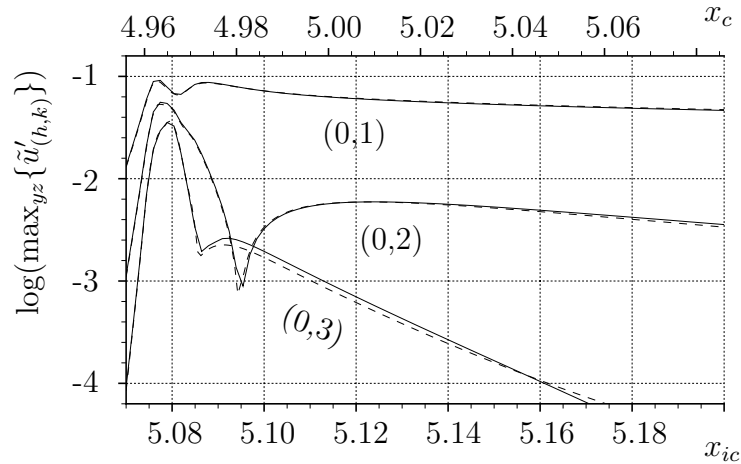


Figure B.4: Comparison of results from incompressible code (solid, x_{ic}) and compressible code (dashed, x_c) for a case with 30% hole suction in a Blasius boundary layer (polynomial suction distribution, see [23]).

cluding oncoming vortices and suction are compared. A self-similar Blasius boundary-layer solution at $Ma_\infty = 0.2$ is computed here and used as compressible reference flow. Differing from the results presented so far, a polynomial has been used for the prescribed suction distribution in both cases. Results are provided in figure B.4. The x -axes are shifted slightly to compensate for weak compressible effects that result in a slightly thicker boundary layer. Thus, the suction-hole locations are matched to investigate the effects at identical $Re_{\delta,1}$ -values. Almost identical results confirm converged results at the prescribed boundary conditions for both codes. For more details on the last study including comparisons of the resulting vortical structures and flow fields see [23].

B.2 Three-dimensional base flow

Grid studies for the three-dimensional base flow are provided for case 3-H (see chapter 5), where an oncoming crossflow vortex is subject to three succeeding suction holes operating at 50% u_∞ . Results can be found in figure B.5. The selected modes show unsatisfactory results for the coarse grid whereas the two fine grids show almost identical vortex attenuation and weakening of secondary amplification of the unsteady mode $\omega = 120$. Similar to the two-dimensional

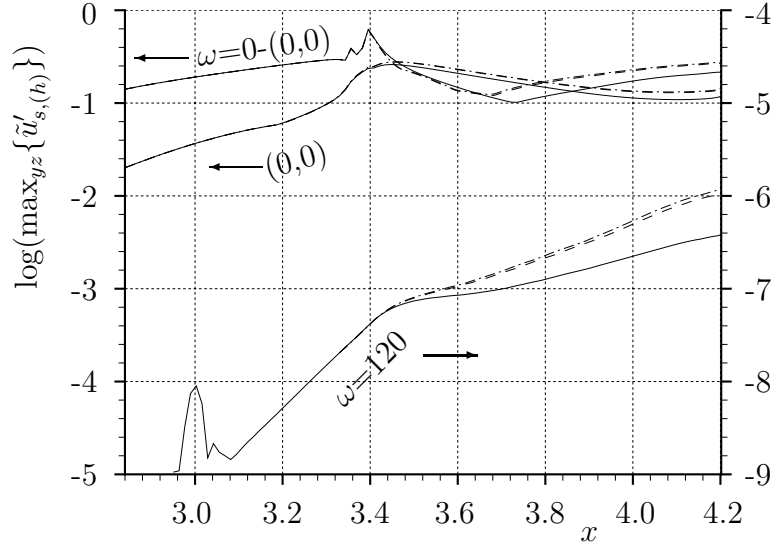


Figure B.5: Grid study employing three wall-normal stretched grids: $\Delta y_{wall} = 9.89 \cdot 10^{-4}$ (solid lines), $\Delta y_{wall} = 6.59 \cdot 10^{-4}$ (dashed lines), and $\Delta y_{wall} = 4.95 \cdot 10^{-4}$ (dash-dotted lines). For Case 3-H (see chapter 5) the downstream development of selected modal $\tilde{u}'_{s,(h)}$ -amplitudes is evaluated: Mean flow deformation $(0,0)$; steady, three-dimensional deformation $\omega = 0 - (0,0)$; and unsteady high-frequency mode $\omega = 120$.

case, the amplitude level of vortices on an under-resolved grid are too large, thus the reduction of the crossflow-vortex amplitude turns out to be too strong. The grid employing $\Delta y_{wall} = 6.59 \cdot 10^{-4}$ is considered for all cases provided in section 5. Again, refining the streamwise or spanwise coordinate shows absolutely no difference.

C Compressible Navier-Stokes equations

The set of equations that is solved by the compressible numerical method described in section 2.2 consist of the energy equation

$$E = \rho \int c_v dT + \frac{\rho}{2} (u^2 + v^2 + w^2), \quad (\text{C.1})$$

the equation of state

$$p = \frac{\rho T}{\kappa M a_\infty^2}, \quad (\text{C.2})$$

and the compressible three-dimensional Navier-Stokes equations including the continuity equation

$$\frac{\partial Q}{\partial t} + \frac{\partial F}{\partial x} + \frac{\partial G}{\partial y} + \frac{\partial H}{\partial z} = 0, \quad (\text{C.3})$$

where the flux vectors F , G and H are defined as

$$F = \begin{pmatrix} \rho u \\ \rho u^2 + p - \tau_{xx} \\ \rho u v - \tau_{xy} \\ \rho u w - \tau_{xz} \\ u(E + p) + q_x - u \tau_{xx} - v \tau_{xy} - w \tau_{xz} \end{pmatrix}, \quad (\text{C.4a})$$

$$G = \begin{pmatrix} \rho v \\ \rho u v - \tau_{xy} \\ \rho v^2 + p - \tau_{yy} \\ \rho v w - \tau_{yz} \\ v(E + p) + q_y - u \tau_{xy} - v \tau_{yy} - w \tau_{yz} \end{pmatrix}, \quad (\text{C.4b})$$

$$H = \begin{pmatrix} \rho w \\ \rho u w - \tau_{xz} \\ \rho v w - \tau_{yz} \\ \rho w^2 + p - \tau_{zz} \\ w(E + p) + q_z - u \tau_{xz} - v \tau_{yz} - w \tau_{zz} \end{pmatrix}. \quad (\text{C.4c})$$

The normal and shear stress components are

$$\tau_{xx} = \frac{\mu}{Re} \left(\frac{4}{3} \frac{\partial u}{\partial x} - \frac{2}{3} \frac{\partial v}{\partial y} - \frac{2}{3} \frac{\partial w}{\partial z} \right), \quad (\text{C.5a})$$

$$\tau_{yy} = \frac{\mu}{Re} \left(\frac{4}{3} \frac{\partial v}{\partial y} - \frac{2}{3} \frac{\partial u}{\partial x} - \frac{2}{3} \frac{\partial w}{\partial z} \right), \quad (\text{C.5b})$$

$$\tau_{zz} = \frac{\mu}{Re} \left(\frac{4}{3} \frac{\partial w}{\partial z} - \frac{2}{3} \frac{\partial u}{\partial x} - \frac{2}{3} \frac{\partial v}{\partial y} \right), \quad (\text{C.5c})$$

$$\tau_{xy} = \frac{\mu}{Re} \left(\frac{\partial u}{\partial y} + \frac{\partial v}{\partial x} \right), \quad (\text{C.6a})$$

$$\tau_{xz} = \frac{\mu}{Re} \left(\frac{\partial u}{\partial z} + \frac{\partial w}{\partial x} \right), \quad (\text{C.6b})$$

$$\tau_{yz} = \frac{\mu}{Re} \left(\frac{\partial v}{\partial z} + \frac{\partial w}{\partial y} \right), \quad (\text{C.6c})$$

and the heat fluxes are

$$q_x = - \frac{\vartheta}{(\kappa - 1) Re Pr Ma_\infty^2} \frac{\partial T}{\partial x}, \quad (\text{C.7a})$$

$$q_y = - \frac{\vartheta}{(\kappa - 1) Re Pr Ma_\infty^2} \frac{\partial T}{\partial y}, \quad (\text{C.7b})$$

$$q_z = - \frac{\vartheta}{(\kappa - 1) Re Pr Ma_\infty^2} \frac{\partial T}{\partial z}, \quad (\text{C.7c})$$

where ϑ and μ are the thermal conductivity and the dynamic viscosity.

D Coordinate systems

The coordinate system (x, y, z) used for all DNS is a body-fixed Cartesian coordinate system where the x -axis is perpendicular to the leading edge, z runs parallel to the leading edge and y denotes the wall-normal coordinate. Other coordinate systems used for postprocessing and visualization of DNS data are sketched in figure D.1.

The streamline-oriented coordinate system (x_s, y, z_s) is turned around the y -axis (in clockwise direction when viewed from top) and defined such that the x_s -axis is parallel to the local edge velocity outside the boundary layer at every downstream position (ϕ_e is the corresponding local angle of the potential streamline with the x -axis, cf. figure 3.3 where the boundary-layer parameters are introduced). The velocity components u_s and w_s point in x_s - and z_s -direction. The crossflow component w_s has then the typical crossflow shape, being by definition zero outside the boundary layer (cf. e.g. figure 1.1). Note that the orientation x_s is not constant with varying x -coordinate.

The rotated coordinate system (x_r, y, z_r) is an arbitrarily-rotated reference system, mainly used for vortex visualization. The origin is marked by x_{r0} and z_{r0} and the axes x and x_r include the angle ϕ_r . The respective velocity components are accordingly named u_r and w_r .

One special rotated coordinate system (ξ, y, ζ) is defined such that the origin coincides with the center of the suction hole. Thus, the flow field in the vicinity of the wall orifice can be visualized optimally. The corresponding velocity components are also named u_r and w_r for simplicity.

The transformation equations for the streamline oriented coordinate system are:

$$x_s = (x - x_{r0}) \cos(\phi_e) + (z - z_{r0}) \sin(\phi_r) \quad (\text{D.1})$$

$$z_s = -(x - x_{r0}) \sin(\phi_e) + (z - z_{r0}) \cos(\phi_r), \quad (\text{D.2})$$

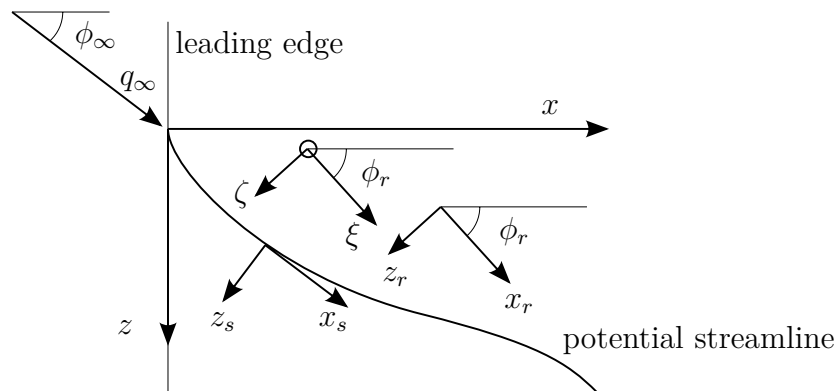


Figure D.1: Sketch of coordinate systems used.

but are identical for the other two cases when (x_s, z_s, ϕ_e) are substituted by (x_r, z_r, ϕ_r) or (ξ, ζ, ϕ_r) , respectively. The definition of the rotated velocity and vorticity components is straightforward. If $\phi_r = \text{const.}$, the resulting coordinate system has straight axes.

E Influence of the hole diameter

Suction distributions according to equation (2.11) are considered and mass as well as momentum fluxes are calculated for cases with one suction hole per vortex and varying hole diameters, see table E.1. The flow setup is according to case 1-H of chapter 5. Case A employs the suction hole with diameter $d = \hat{d}$ and maximum suction velocity $v_{max} = \hat{v}_{max} = 0.2 u_\infty$. The suction holes in cases B and C provide the same mass fluxes with the hole diameters decreased by 25% and 40%, respectively. For case B* the suction hole is 25% smaller, set up such that the same momentum flux is obtained as in case A, resulting in less mass flux. Figure E.1 shows the downstream modal development of selected \tilde{u}'_s -amplitudes. We observe an almost identical attenuation of secondary growth for cases A,B, and C whereas case B* results in less attenuation. This is due to less weakening of the CFV in case B, see figure E.2. Thus, the effect of localized suction for the investigated hole set-ups depends rather on the mass flux sucked than the momentum flux associated with it.

Case	d/\hat{d}	v_{max}/\hat{v}_{max}	$(v_{max}/\hat{v}_{max})^2$	$\dot{m} \sim d^2 v_{max}$	$i \sim d^2 v_{max}^2$
A	1	1	1	1	1
B	0.75	1.78 (= $(\hat{d}/d)^2$)	3.16 (= $(\hat{d}/d)^4$)	1	1.78 (= $(\hat{d}/d)^2$)
C	0.6	2.78 (= $(\hat{d}/d)^2$)	7.72 (= $(\hat{d}/d)^4$)	1	2.78 (= $(\hat{d}/d)^2$)
B*	0.75	1.33 (= \hat{d}/d)	1.78 (= $(\hat{d}/d)^2$)	0.75 (= \hat{d}/d)	1

$\hat{d} = 20 \Delta x, \hat{v}_{max} = 0.200 \cdot u_\infty = 0.165 \cdot u_{s,e}$

Table E.1: Mass and momentum fluxes for cases considered in appendix E.

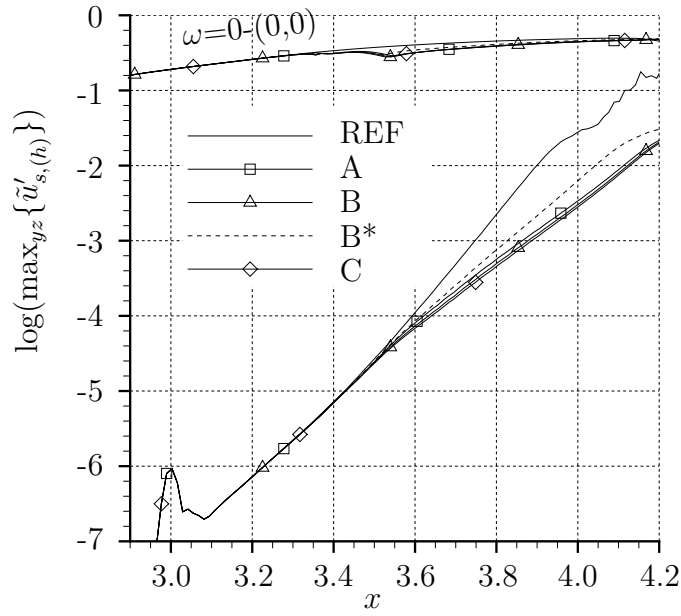


Figure E.1: Downstream development of modal $\tilde{u}'_{s,(h)}$ -amplitudes from Fourier analysis in time (maximum over y and z). Shown are maximum steady 3-d deformation ($\omega = 0 - (0,0)$) and one selected mode $\omega = 108$ for the reference case and three suction cases (see table E.1).

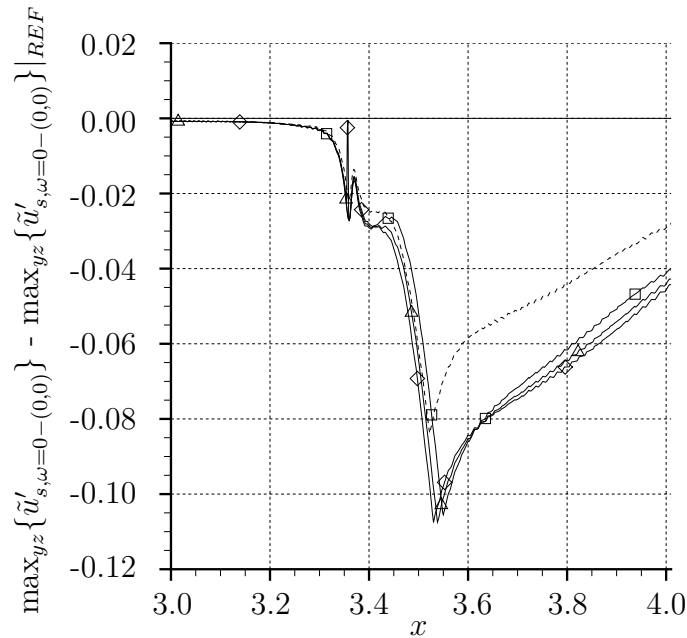


Figure E.2: Difference of modal $\omega = 0 - (0,0)$ - values with respect to case REF. Shown are the cases as labeled in figure E.1.

Bibliography

- [1] Airbus 350-1000 aircraft. <http://www.airbus.com/aircraftfamilies/passengeraircraft/a350xwbfamily/a350-1000/>. Date of download: 04/03/2012.
- [2] Boeing's new airplane 787, laminar flow nacelle. http://boeing.com/newairplane/787/design_highlights/#/VisionaryDesign/Aerodynamics/LaminarFlowNacelle. Date of download: 04/03/2012.
- [3] C. Abegg, H. Bippes, and E. Janke. Stabilization of boundary-layer flows subject to crossflow instability with the aid of suction. In H. F. Fasel and W. Saric, editors, *Laminar-Turbulent Transition*, Proc. IUTAM Symposium, Sedona, AZ, USA (1999). Springer, 2000.
- [4] D. Arnal, A. Seraudie, and J. P. Archambaud. Influence of surface roughness and suction on the receptivity of a swept wing boundary layer. In H. F. Fasel and W. Saric, editors, *Laminar-Turbulent Transition*, Proc. IUTAM Symposium, Sedona, AZ, USA (1999). Springer, 2000.
- [5] A. Babucke. *Direct Numerical Simulation of Noise-Generation Mechanisms in the Mixing Layer of a Jet*. Dissertation, Universität Stuttgart, 2009.
- [6] A. Babucke, J. Linn, M. J. Kloker, and U. Rist. Direct numerical simulation of shear flow phenomena on parallel vector computers. In M. Resch, editor, *High Performance Computing on Vector Systems, Proceedings of the High Performance Computing Center Stuttgart, March 2005*, pages 229–247. Springer, 2006.
- [7] S. Balachandar, C. Streeet, and M. R. Malik. Secondary instability in rotating-disk flow. *J. Fluid Mech.*, 242:323–347, 1992.

- [8] H. Bippes. Basic experiments on transition in three-dimensional boundary layers dominated by crossflow instability. *Prog. Aerosp. Sci.*, 35:363–412, 1999.
- [9] G. Bonfigli. *Numerical Simulation of transition and early turbulence in a 3-d boundary layer perturbed by superposed stationary and travelling crossflow vortices*. PhD thesis, Universität Stuttgart, 2006.
- [10] G. Bonfigli and M. Kloker. Three-dimensional boundary-layer transition phenomena investigated by spatial direct numerical simulation. In H. F. Fasel and W. Saric, editors, *Laminar-Turbulent Transition*, Proc. IUTAM Symposium, Sedona, AZ, USA (1999). Springer, 2000.
- [11] G. Bonfigli and M. J. Kloker. Spatial Navier-Stokes simulation of crossflow-induced transition in a three-dimensional boundary layer. In W. Nitsche, H.-J. Heinemann, and R. Hilbig, editors, *New Results in Numerical and Experimental Fluid Dynamics II*, volume 72 of *NNFM*, pages 61–68. Vieweg, 1999.
- [12] G. Bonfigli and M. J. Kloker. Secondary instability of crossflow vortices: validation of the stability theory by direct numerical simulation. *J. Fluid Mech.*, 583:229–272, 2007.
- [13] A. L. Braslow. *A history of suction-type laminar-flow control with emphasis on flight research*. Monographs in aerospace history. NASA History Office, Office of Policy and Plans, NASA Headquarters, 1999.
- [14] C. Bulgubure and D. Arnal. Dassault Falcon 50 laminar flow flight demonstrator. In *DGLR-Bericht 92-06, Proceedings of the First European Forum on Laminar Flow Technology*, Hamburg, Germany. DGLR, 1992.
- [15] V. G. Chernoray, A. V. Dovgal, V. V. Kozlov, and L. Löfdahl. Experiments on secondary instability of streamwise vortices in a swept-wing boundary layer. *J. Fluid Mech.*, 534:295–325, 2005.
- [16] W. Eissler. *Numerische Untersuchung zum laminar-turbulenten Strömungsumschlag in Überschallgrenzschichten*. Dissertation, Universität Stuttgart, 1995.

- [17] H. Fasel. *Untersuchungen zum Problem des Grenzschichtumschlags durch numerische Integration der Navier-Stokes-Gleichungen*. Dissertation, Universität Stuttgart, 1974.
- [18] H. Fasel, A. Thumm, and H. Bestek. Direct numerical simulation of transition in supersonic boundary layer: oblique breakdown. In L. D. Kral and T. A. Zang, editors, *Transitional and Turbulent Compressible Flows*, volume 151 of *FED*, pages 77–92. ASME, 1993.
- [19] A. Fezer and M. J. Kloker. DNS of transition mechanisms at Mach 6.8: flat plate vs. sharp cone. In *West-East High-Speed Flow Fields 2002*, pages 434–441, conf. proc., Barcelona, Spain (2002). CIMNE, 2003.
- [20] T. Friederich and M. J. Kloker. Control of the secondary cross-flow instability using localized suction. *J. Fluid Mech.*, 706:470–495, 2012.
- [21] T. A. Friederich and M. J. Kloker. Localized blowing and suction for direct control of the crossflow secondary instability. *AIAA*, 2008-4394, 2008. 38th Fluid Dynamics Conference and Exhibit, Seattle, Washington.
- [22] T. A. Friederich and M. J. Kloker. Control of crossflow-vortex induced transition: DNS of pinpoint suction. *AIAA*, 2011-3884, 2011. 41th Fluid Dynamics Conference and Exhibit, Honolulu, Hawaii.
- [23] T. A. Friederich and M. J. Kloker. Direct numerical simulation of swept-wing laminar flow control using pinpoint suction. In W. Nagel, D. Kröner, and M. Resch, editors, *High Performance Computing in Science and Engineering '10, Transactions of the High Performance Computing Center, Stuttgart (HLRS) 2010*, pages 231–250. Springer, 2011.
- [24] T. A. Friederich and M. J. Kloker. Numerical simulation of crossflow-transition control using pinpoint suction. In *Contributions to the 17th STAB/DGLR Symposium Berlin, Germany 2010, accepted, to be published*, NNFM. Springer, 2012.
- [25] J. Goldsmith. Critical laminar suction parameters for suction into an isolated hole or a single row of holes. Technical Report No. BLC-95, Northrop Aircraft Inc., 1957.

- [26] W. E. Gray. The effect of wing sweep on laminar flow. *RAE TM Aero*, 255, 1952.
- [27] N. Gregory. Research on suction surfaces for laminar flow. In G. V. Lachmann, editor, *Boundary Layer and Flow Control*, volume 2, pages 924–960. Pergamon, 1961.
- [28] N. Gregory, J. T. Stuart, and W. S. Walker. On the stability of three-dimensional boundary layers with applications to the flow due to a rotating disk. *Philos. Trans. R. Soc. London*, Ser. A248:155-199, 1955.
- [29] T. Herbert. Secondary instability of boundary layers. *Annu. Rev. Fluid Mech.*, 20:487–526, 1988.
- [30] M. Högberg and D. Henningson. Secondary instability of cross-flow vortices in Falkner-Skan-Cooke boundary layers. *J. Fluid Mech.*, 368:339–357, 1998.
- [31] J. Jeong and F. Hussain. On the identification of a vortex. *J. Fluid Mech.*, 285:69–94, 1995.
- [32] R. D. Joslin. Aircraft laminar control. *Annu. Rev. Fluid Mech.*, 30:1–29, 1998.
- [33] R. D. Joslin. Overview of laminar control. *NASA Langley Research Center, Hampton, VA*, NASA/TP-1998-208705, 1998.
- [34] Y. S. Kachanov and V. Y. Levchenko. The resonant interaction of disturbances at laminar-turbulent transition. *J. Fluid Mech.*, 138:209–247, 1984.
- [35] M. Kawakami, Y. Kohama, and M. Okutsu. Stability characteristics of stationary crossflow vortices in three-dimensional boundary layer. *AIAA*, 99-0811, 1999.
- [36] P. S. Klebanoff, K. D. Tidstrom, and L. M. Sargent. The three-dimensional nature of boundary-layer instability. *J. Fluid Mech.*, 12:1–34, 1962.

- [37] M. Kloker. *Direkte Numerische Simulation des laminar-turbulenten Strömungsumschlages in einer stark verzögerten Grenzschicht*. Dissertation, Universität Stuttgart, 1993.
- [38] M. Kloker. A robust high-order split-type compact FD scheme for spatial direct numerical simulation of boundary-layer transition. *Applied Scientific Research*, 59(4):353–377, 1998.
- [39] M. J. Kloker. Advanced laminar flow control on a swept wing: useful crossflow vortices and suction. *AIAA*, 2008-3835, 2008. 38th Fluid Dynamics Conference and Exhibit, Seattle, Washington.
- [40] W. Koch. On the spatio-temporal stability of primary and secondary crossflow vortices in a three-dimensional boundary layer. *J. Fluid Mech.*, 456:85–111, 2002.
- [41] W. Koch, F. P. Bertolotti, A. Stolte, and S. Hein. Nonlinear equilibrium solutions in a three-dimensional boundary layer and their secondary instability. *J. Fluid Mech.*, 406:131–174, 2000.
- [42] Y. P. Kohama, W. S. Saric, and W. Hoos. A high-frequency, secondary instability of crossflow vortices that leads to transition. In *Proceedings of the R.A.S. conference on boundary-layers and control*, pages 4.1–4.13, Cambridge, U.K., 1991.
- [43] U. Konzelmann. *Numerische Untersuchung zur räumlichen Entwicklung dreidimensionaler Wellenpakete in einer Plattengrenzschichtströmung*. Dissertation, Universität Stuttgart, 1990.
- [44] P. Kunze. Numerische Untersuchungen des Einflusses des Ausblasekanals von Löchern auf die Filmkühlung im Überschall. Studienarbeit (Advisors: A. Babucke, M. Kloker & J. Linn), Institut für Aerodynamik und Gasdynamik, Universität Stuttgart, 2008.
- [45] J. Linn. *Numerische Untersuchungen zur Filmkühlung in laminaren Über- und Hyperschallgrenzschichtströmungen*. Dissertation, Universität Stuttgart, 2011.

- [46] L. M. Mack. Boundary-layer linear stability theory. In *Special Course on Stability and Transition of Laminar Flow*, AGARD report 709, 1984.
- [47] D. G. MacManus and J. A. Eaton. Micro-scale three-dimensional Navier–Stokes investigation of laminar flow control suction hole configurations. *AIAA*, 96-0544, 1996.
- [48] D. G. MacManus and J. A. Eaton. Flow physics of discrete boundary layer suction - measurements and predictions. *J. Fluid Mech.*, 417:47–75, 2000.
- [49] D. V. Maddalon. Hybrid laminar-flow control flight research. Technical Report TM-4331, page 47, NASA Research and Technology, 1991.
- [50] D. V. Maddalon, F. S. Collier, L. C. Montaya, and C. K. Land. Transition flight experiments on a swept wing with suction. *AIAA*, 89-1893, 1989.
- [51] M. R. Malik and C.-L. Chang. Crossflow disturbances in three-dimensional boundary layers: nonlinear development, wave interaction and secondary instability. *J. Fluid Mech.*, 268:1–36, 1994.
- [52] M. R. Malik, F. Li, M. M. Choudhari, and C. L. Chang. Secondary instability of crossflow vortices and swept-wing boundary-layer transition. *J. Fluid Mech.*, 399:85–115, 1999.
- [53] H. L. Meitz. *Numerical investigation of suction in a transitional flat-plate boundary layer*. PhD thesis, University of Arizona, 1996.
- [54] H. L. Meitz and H. F. Fasel. Numerical simulation of boundary-layer flow over suction holes. In R. Kobayashi, editor, *Laminar-Turbulent Transition*, Proc. IUTAM Symposium, Sendai, Japan (1994). Springer, 1995.
- [55] R. Messing. *Direkte numerische Simulationen zur diskreten Absaugung in einer dreidimensionalen Grenzschichtströmung*. Dissertation, Universität Stuttgart, 2004.
- [56] R. Messing and M. J. Kloker. Investigation of suction for laminar flow control of three-dimensional boundary layers. *J. Fluid Mech.*, 658:117–147, 2010.

- [57] D. Meyer. *Direkte numerische Simulation nichtlinearer Transitionsmechanismen in der Strömungsgrenzschicht einer ebenen Platte*. Dissertation, Universität Stuttgart, 2003.
- [58] H. Müller. Assessment of roughness analogies for strong discrete suction by means of direct numerical simulation. Diplomarbeit (Advisors: T. Friederich & M. Kloker), Institut für Aerodynamik und Gasdynamik, Universität Stuttgart, 2012.
- [59] W. Müller, H. Bestek, and H. F. Fasel. Spatial direct numerical simulation of transition in a three-dimensional boundary layer. In R. Kobayashi, editor, *Laminar-Turbulent Transition*, Proc. IUTAM Symposium, Sendai, Japan (1994). Springer, 1995.
- [60] A. Pagella, A. Babucke, and U. Rist. Two-dimensional numerical investigations of small-amplitude disturbances in a boundary layer at $Ma=4.8$. *Phys. Fluids*, 16:2272–2281, 2004.
- [61] W. Pfenninger. Some results from the X-21 A program. Part 1. Flow phenomena at the leading edge of swept wings. In *Recent developments in boundary layer research*, volume IV of *AGARDograph 97*, 1965.
- [62] H. L. Reed, T. S. Haynes, and W. S. Saric. Computational fluid dynamics validation issues in transition modeling. *AIAA J.*, 36(5):742–751, 1998.
- [63] H. L. Reed and W. S. Saric. Stability of three-dimensional boundary layers. *Annu. Rev. Fluid Mech.*, 21:235–284, 1989.
- [64] J. Reneaux and A. Blanchard. The design and testing of an airfoil with hybrid laminar flow control. In *DGLR-Bericht 92-06, Proceedings of the First European Forum on Laminar Flow Technology*, Hamburg, Germany. DGLR, 1992.
- [65] G. A. Reynolds and W. S. Saric. Experiments on the stability of the flat-plate boundary layer with suction. *AIAA J.*, 24(2):202–207, 1986.
- [66] U. Rist. *Numerische Untersuchung der räumlichen, dreidimensionalen Strömungsentwicklung beim Grenzschichtumschlag*. Dissertation, Universität Stuttgart, 1990.

- [67] W. S. Saric, A. L. Carpenter, and H. L. Reed. Laminar flow control flight test for swept wings: Strategies for lfc. *AIAA*, 2008-3834, 2008.
- [68] W. S. Saric, R. B. Carrillo, and M. S. Reibert. Leading-edge roughness as a transition control mechanism. *AIAA*, 98-0781, 1998.
- [69] W. S. Saric, R. B. Carrillo, and M. S. Reibert. Nonlinear stability and transition in 3-d boundary layers. *Meccanica*, 33(5):469–487, 1998.
- [70] W. S. Saric, H. L. Reed, and E. J. Kerschen. Boundary-layer receptivity to freestream disturbances. *Annu. Rev. Fluid Mech.*, 34(1):291–319, 2002.
- [71] W. S. Saric, H. L. Reed, and E. B. White. Stability and transition of three-dimensional boundary layers. *Annu. Rev. Fluid Mech.*, 35:413–440, 2003.
- [72] H. Schlichting and K. Gersten. *Boundary-Layer Theory*. Springer, Berlin, 8th corrected edition, 2003.
- [73] O. T. Schmidt and U. Rist. Linear stability of compressible flow in a streamwise corner. *J. Fluid Mech.*, 688:569–590, 2011.
- [74] G. Schrauf. Status and perspectives of laminar flow. *The aeronautical journal*, 1102:639–644, 2005.
- [75] G. B. Schubauer and H. K. Skramstad. Laminar boundary-layer oscillations and transition on a flat plate. *J. Aeronaut. Sci.*, 14:69–78, 1947.
- [76] P. R. Spalart. Numerical study of transition induced by suction devices. In R. M. C. So, C. G. Speziale, and B. E. Launder, editors, *Proceedings of the International Conference: Near-Wall Turbulent Flows*, pages 849–858, Tempe, AZ. Elsevier, 1993.
- [77] J. Thibert, A. Quast, and J. P. Robert. The A320 laminar fin programme. In *DGLR-Bericht 92-06, Proceedings of the First European Forum on Laminar Flow Technology*, Hamburg, Germany. DGLR, 1992.
- [78] A. Thumm. *Numerische Untersuchung zum laminar-turbulenten Strömungsumschlag in transsonischen Grenzschichtströmungen*. Dissertation, Universität Stuttgart, 1991.

- [79] P. Wassermann. *Direkte Numerische Simulationen zum querströmungsinduzierten laminar-turbulenten Umschlagprozess in einer dreidimensionalen Grenzschichtströmung*. Dissertation, Universität Stuttgart, 2002.
- [80] P. Wassermann and M. J. Kloker. Mechanisms and passive control of crossflow-vortex-induced transition in a 3-d boundary layer. *J. Fluid Mech.*, 456:49–84, 2002.
- [81] P. Wassermann and M. J. Kloker. Transition mechanisms induced by travelling crossflow vortices in a three-dimensional boundary layer. *J. Fluid Mech.*, 483:67–89, 2003.
- [82] P. Wassermann and M. J. Kloker. Transition mechanisms in a three-dimensional boundary-layer flow with pressure-gradient changeover. *J. Fluid Mech.*, 530:265–293, 2005.
- [83] E. B. White and W. S. Saric. Secondary instability of crossflow vortices. *J. Fluid Mech.*, 525:275–308, 2005.
- [84] E. B. White, W. S. Saric, R. D. Gladden, and P. M. Gabet. Stages of swept-wing transition. *AIAA*, 2001-0271, 2001.
- [85] F. M. White. *Viscous Fluid Flow*. McGraw-Hill, New York, 2nd edition, 1991.
- [86] T. Wintergerste. *Numerische Untersuchung der Spätstadien der Transition in einer dreidimensionalen Grenzschicht*. Dissertation, Eidgenössische Technische Hochschule Zürich, 2002.
- [87] T. Wintergerste and L. Kleiser. Direct numerical simulation of transition in a three-dimensional boundary layer. In R. A. W. M. Henkes and J. L. van Ingen, editors, *Transitional boundary layers in aeronautics*, Proc. Colloquium of the Royal Netherlands Academy of Arts and Science, Amsterdam, NL (1995). RNAAS, 1996.
- [88] T. Wintergerste and L. Kleiser. Break down of a cross flow vortex in a three dimensional boundary layer. In J. Chollet, editor, *Direct and large-eddy simulation II*, Ercoftac series. Kluwer Academic Press, 1997.

Curriculum Vitae

Name Tillmann Achim Friederich
Date of birth February 09, 1981
Place of birth Stuttgart, Germany
Nationality German

1991-2000 Gymnasium Plochingen
Plochingen, Germany

2000-2001 Civilian service at Rohräckerschule Esslingen
Esslingen, Germany

2001-2007 Study of Aerospace Engineering, University of Stuttgart
Stuttgart, Germany

2003-2004 Internship at Airbus Hamburg (6 months)
Hamburg, Germany

2005-2006 Integrated studies at the University of Arizona,
DAAD scholarship (10 months)
Tucson, Arizona, USA

2007 Diploma in Aerospace Engineering, University of Stuttgart
Stuttgart, Germany

2007-2012 Research assistant at the Institute for Aerodynamics and
Gas Dynamics, University of Stuttgart
Stuttgart, Germany

